COLLISION ENERGY DEPENDENCE OF THE REACTIONS OF METASTABLE NEON WITH SMALL MOLECULES

by

Joseph H. Noroski

B.S., University of Pittsburgh, 1993

M.S., University of Pittsburgh, 2001

M.S., University of Pittsburgh, 2007

Submitted to the Graduate Faculty of

Arts and Sciences in partial fulfillment

of the requirements for the degree of

Doctor of Philosophy

University of Pittsburgh

2009

UNIVERSITY OF PITTSBURGH

COLLEGE OF ARTS AND SCIENCES

This thesis was presented

by

Joseph H. Noroski

It was defended on

April 3, 2009

and approved by

Geoffrey Hutchison, Professor, Chemistry

David Pratt, Professor, Chemistry

James Mueller, Professor, Physics

Dissertation Director: Kenneth Jordan, Professor, Chemistry

Dissertation director: Kenneth D. Jordan

COLLISION ENERGY DEPENDENCE OF THE REACTIONS OF METASTABLE NEON WITH SMALL MOLECULES

Joseph H. Noroski, Ph.D.

University of Pittsburgh, 2009

The reaction dynamics of Ne* ($2p^5 3s$ $^3P_2$, $^3P_0$) + X → [NeX]$^+$ + e$^-$ (X = H_2, CO, N_2, NO, O_2, CO_2, and C_2H_2) were studied with supersonic beams at various collision energies (E) via electron spectroscopy. Increasing E decreases the interparticle distance at which ionization occurs, allowing for exploration of the reaction potential energy surfaces via the kinetic energy ε of the ejected electron. Data were fit to give vibrational populations and line shifts ($\Delta\varepsilon_s$), the difference between the excitation energy of Ne* and the vibronic energy of the target molecules, where vibronic excitation is due to Ne*. The resulting populations were compared to calculated or experimental Franck-Condon factors (FCfs), and vibrational progressions were identified. Deviation from Franck-Condon (FC) behavior was observed in all cases except for C_2H_2, and all spectra at all E showed a blue shift except CO_2. With increasing E, $\Delta\varepsilon_s$ for H_2^+, CO^+, and N_2^+ increased with increasing E, while $\Delta\varepsilon_s$ decreased for NO^+ and $C_2H_2^+$. The CO_2^+ spectra revealed a nearly constant red shift for the lowest three E and a blue shift for the highest E. O_2^+ showed a very small blue shift, but the O_2^+ populations were not determined due to an underlying continuum.

Penning, excitation transfer, and ion-pair mechanisms are the most widely accepted for the reactions of metastable atoms. The closed-shell structure of H_2, CO, and N_2 and the large, increasing $\Delta\varepsilon_s$ suggest that their Ne* reactions proceed via the Penning mechanism. The open-shell structure of NO and its decreasing $\Delta\varepsilon_s$ indicates changing dynamics and possibly also competition between all three mechanisms for Ne* + NO. The very small $\Delta\varepsilon_s$ for O_2^+ implies the excitation transfer mechanism for Ne* + O_2. Ne* reactions with CO_2 and C_2H_2 both exhibited constant $\Delta\varepsilon_s$ values for more than one E. This suggests that an excitation transfer mechanism is at work in these systems, but changes in $\Delta\varepsilon_s$ at other E indicate that competing mechanisms may also be relevant.

Lastly, a retrospective on authoring a solutions manual for a freshman chemistry textbook is offered.

TABLE OF CONTENTS

LIST OF TABLES

LIST OF FIGURES

xii

1.0 PENNING IONIZATION

1.1 PREVIOUS RESEARCH

Penning ionization (PI) can be defined as an electron rearrangement reaction in which an

electron is transferred from a high-lying shell of atom or molecule B to the inner-shell vacancy

left by promoting an electron from a ground state of atom or molecule A to an excited state

denoted A*. See Figure 1.1. The Penning mechanism, frequently referred to as the exchange

mechanism in the literature, depends on orbital overlap, and it often results in peak intensities

that exhibit Franck-Condon behavior. For atomic A and a diatomic target molecule BC, we can

write the reaction as follows:

$$A^* \ + \ BC \ \rightleftharpoons \ [ABC]^* \ \rightarrow \ [ABC]^+ \ + \ e^- \ \rightarrow \ \text{ionic products.}$$

$[ABC]^*$ and $[ABC]^+$ are two collision intermediates. The second intermediate can undergo any

of the following:

$$
\begin{aligned}
[ABC]^+ \ &\rightarrow \ A \ + \ BC^+ &&\text{(Penning ionization)} \\
&\rightarrow \ ABC^+ &&\text{(associative ionization)} \\
&\rightarrow \ A \ + \ B^+ \ + C &&\text{(dissociative ionization)} \\
&\rightarrow \ AB^+ \ + \ C &&\text{(rearrangement ionization)}
\end{aligned}
$$
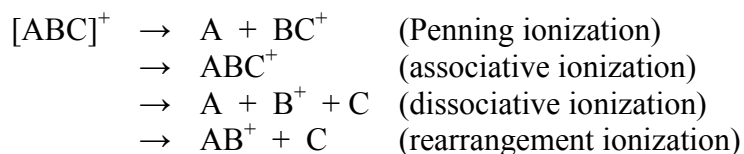
While the first reaction is typically called "Penning ionization", our definition indicates

that all are PI *if they proceed by the mechanism described above*. A* is usually a metastable

1
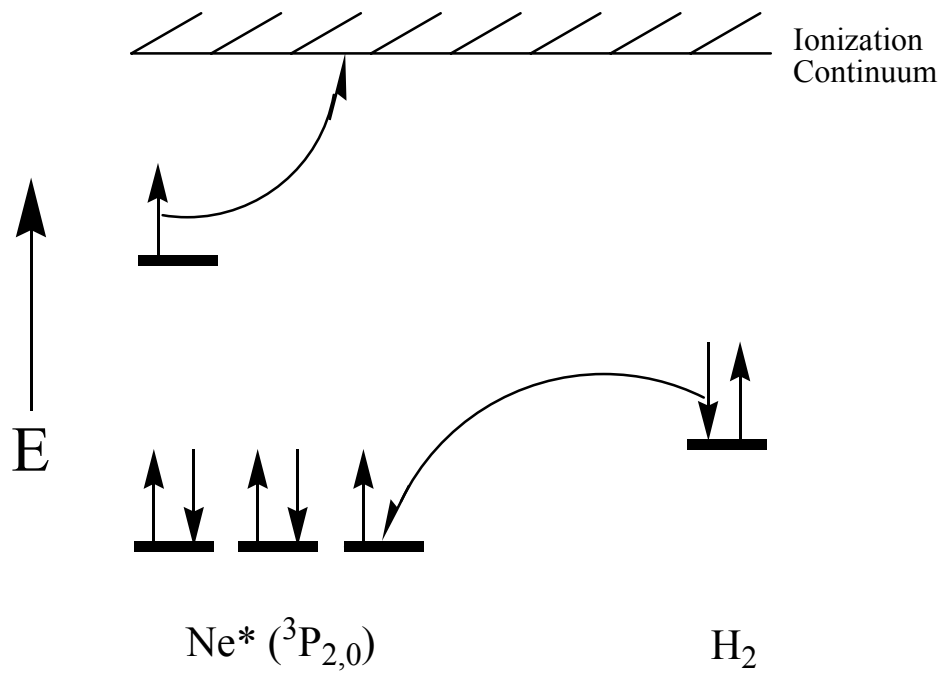
Figure 1.1: Penning ionization. The schematic diagram above conveys the key aspects of the Penning (i.e., exchange) mechanism that defines Penning ionization.

atom, but, sometimes, it is a molecule. A* is produced by bombarding A with an electron beam. The Siska group is primarily interested in the reactions for which the metastable atom is a noble gas. Cermak and Herman[1] (1965) were among the first to suggest determining the kinetic energy of the electrons that are ejected via PI as a means of monitoring gas phase reactions. This type of experiment is dubbed Penning ionization electron spectroscopy (PIES).

PIES is, however, only a subset of the vast number of reactions that can be performed with crossed beams of reactants, and Y. T. Lee notes that there are many reasons to employ this type of experiment, being that one can: (1) control the energies of the reagents, (2) understand the dependence of chemical reactivity on molecular orientation, (3) explore the nature of reaction intermediates and their subsequent decay dynamics, and (4) identify complex reaction mechanisms involving polyatomic radical products.[2] We are particularly successful with (1) because of our use of supersonic jets. (See below.) While (4) is not the subject of this thesis, it *is* work that has been done and is ongoing[3] in the Siska lab in our scattering apparatus, which can be used to obtain data that is complementary to PIES data. To elucidate reaction mechanisms from PI, one can determine product angular and velocity distributions, a task accomplished by observing the *ions* produced in a chemical reaction. Additionally, the total ionization cross-section Q_I, the collision energy dependence of Q_I, branching ratios, and energy redistribution can be derived from the analysis of ions from the reaction.[4] The other principal product of PI is *electrons*. Ejected electrons, "viewed" through PIES, can be used to derive information about nascent vibronic distributions of the Penning ions. [4] This means that we gain dynamical information about *the actual electron transfer event*. Further dynamical discussion is below, but,

now that we have provided a motivation for the use of PI, we move on to more specifics about work with Ne*.

PIES experiments involving Ne* were first done, of course, with simple target atoms and molecules[5]: He*, Li, Na, Ar, K, Kr, Xe, Cs, and H_2. Many of these experiments were performed in the 1980's, and, as the list shows, PIES theory was initially explored for atom-atom collisions. Progress in this field, particularly with Ne*, has been slow for two main reasons. First, the assignment of peaks becomes much more difficult as the number of atoms in the target molecule increases since there are more molecular orbitals (MO's) from which electrons can be ejected and there are more normal modes of vibration that can be excited. Any mixing of these normal modes complicates the electron spectrum even more. Second, the lower excitation energy of Ne* , compared to He*, prevents probing as deeply into lower energy MOs and from ejecting high kinetic energy electrons, which are easier to detect since they are far from the noise prevalent at low kinetic energy. See Table 1.1. Further, this lower excitation energy leads to more complicated spectra and mechanisms, as described throughout this dissertation.

Table 1.1: Metastable gas atom characteristics[6]

Atom	Electron configuration	State	Excitation energy (eV)
He	$1s2s$	$2\,^1S_0$	20.6158^a
		$2\,^3S_1$	19.8196^a
Ne	$2p^53s$	$3\,^3P_0$	16.7154^b
		$3\,^3P_2$	16.6191^b

[a] and [b] are listed under Reference 6.

Still, intrepid physical chemists continue to research the reactions of Ne*. Lescop *et al.*[7] examined the PI of CO_2 by Ne*, made peak assignments, and proposed a non-van der Waals interaction between the colliding species. Maruyama *et al.*[8] examined the PI of CO_2 clusters by Ne*. Additionally, the Lescop and Tuffin group has explored[9,10,11,12,13] via PIES the reactions of Ne* with NH_3, C_2H_2, H_2O, N_2, and CO *at thermal energies*. By comparison to NeI photoionization the NH_3 results showed that Ne*/NH_3 interaction influences the ionization dynamics and, in typical fashion, they explored the agreement of vibrational populations with Franck-Condon factors. Vecchiocattivi *et al.*[14] have also conducted crossed beam studies of excited neon on many small molecules to determine total ionization cross sections. Only recently has the Vecchiocattivi group configured its apparatus to perform kinetic energy studies in the manner that P. E. Siska used years earlier. (See below.) In a study[15] of the Ne* + N_2O reaction, the Vecchiocattivi group explored the products of autoionization via mass spectrometry as well as the correlation between the collision energy and the molecular orbitals of N_2O that are involved in the process. A follow up paper[16] contains a theoretical investigation of this same reaction with the finding that "orientation effects tend to become less pronounced with increasing collision energy."

Over the past decade, the Siska group has explored He* reactions[17,18] with H_2, HD, D_2, N_2, and CO [4] and those of Ne* with Ar[19], H_2[20], NO[21], CO, NO, CO_2, and C_2H_2. Shown in Figure 1.1, the accepted mechanism for PI is the *exchange mechanism*, which gained acceptance due to the work of Hotop *et al.*[22], who used a reaction cross section argument, and Keliher *et al.*[23], who showed that that He*($2\,^3S_1$) PI yields spin polarized electrons and argued for the mechanism on the grounds of conservation of spin angular momentum. (By "exchange" Hotop

simply meant to describe the exchange of the two participating electrons [22], as in Figure 1.1. In this context exchange was not a reference to the quantum mechanical concept of exchange or exchange integrals.) Their work eliminated the once-proposed *radiative mechanism* which proposed that the metastable relaxes and emits a photon, which ionizes the target molecule. The relatively long lifetime of the metastable at supersonic beam conditions also argues against the radiative mechanism.[24][22] The study of He* ($2\,^1S_0$, $2\,^3S_1$) was the logical place for all research in this area to begin since the collisions involve spherically symmetric *s* orbitals. The reactions with Ne*, however, are significantly more complicated. The metastable states possess angular momentum ($^3P_{2,0}$), and the hole in Ne* is in a *p* orbital, leading to geometrically dependent collisions. How these differences affect PI reactions are still unsettled questions. Further, the smaller energies involved are more likely to produce states that are resonant with a densely packed set of states known as Rydberg states, which exist in the continuum of states for the A + B^+ + e^- system and result from weakly held electrons (see below). While laying the groundwork for research into these Rydberg states, our recent efforts mainly have been focused on determining the kinetic energy dependence of the Ne* PI spectra that have been obtained over the recent years. Confirmation of Lescop's assignment of the vibrational progressions that are excited by the reaction of CO_2 with Ne* is also a goal. For the sake of reference and discussion in this dissertation, Table 1.2 includes the ground state valence electron configurations, term symbols, and point groups of the molecules of recent interest to our group. Table 1.3 gives adiabatic ionization potentials of the small molecules examined in this dissertation.

Table 1.2: Small molecule configurations, term symbols, and point groups

Molecule	Valence electron configuration	Term symbol	Point group
H_2	$(1\sigma_g)^2$	$^1\Sigma_g^+$	$D_{\infty h}$
N_2	$(2\sigma_g)^2(2\sigma_u)^2(1\pi)^4(3\sigma_g)^2$	$^1\Sigma_g^+$	$D_{\infty h}$
O_2	$(2\sigma_g)^2(2\sigma_u)^2(3\sigma_g)^2(1\pi_u)^4(1\pi_g)^2$	$^3\Sigma_g^-$	$D_{\infty h}$
CO	$(3\sigma)^2(4\sigma)^2(1\pi)^4(5\sigma)^2$	$^1\Sigma^+$	$C_{\infty v}$
NO	$(3\sigma)^2(4\sigma)^2(1\pi)^4(5\sigma)^2(2\pi)^1$	$^2\Pi$	$C_{\infty v}$
CO_2	$(2\sigma_g)^2(2\sigma_u)^2(3\sigma_g)^2(3\sigma_u)^2(1\pi_u)^4(1\pi_g)^4$	$^1\Sigma_g^+$	$D_{\infty h}$
N_2O	$(4\sigma)^2(5\sigma)^2(6\sigma)^2(1\pi)^4(7\sigma)^2(2\pi)^4$	$^1\Sigma^+$	$C_{\infty v}$
C_2H_2	$(2\sigma_g)^2(2\sigma_u)^2(3\sigma_g)^2(1\pi_u)^4$	$^1\Sigma_g^+$	$D_{\infty h}$

Table 1.3: Adiabatic ionization potentials of some small molecules

Molecule	State	Adiabatic ionization potential (eV)
H_2	X	15.42593[25]
N_2	X	15.5808[26]
	A	16.6986(Ref. 26)
	B	18.7507(Ref. 26)
O_2	X	12.071[27]
	a	16.101(Ref. 27)
	A	17.045(Ref. 27)
	b	18.171(Ref. 27)
CO	X	14.0139(Ref. 26)
	A	16.5440(Ref. 26)
	B	19.6712(Ref. 26)
NO	X	9.264[28]
	a	15.663(Ref. 28)
	b	16.560(Ref. 28)
	w	16.875(Ref. 28)
CO_2	X	13.7772[29]
	A	17.3132 (Ref. 29)
	B	18.0761 (Ref. 29)
	C	19.394[30]
N_2O	X	12.8898[31]
	A	16.3896[32]
	B	17.65[33]
	C	20.11 (Ref. 33)
C_2H_2	X	11.403[34]
	A	16.297 (Ref. 34)
	B	18.391 (Ref. 34)

1.2 THE TWO POTENTIAL MODEL

The "kinetic energy" of our PIES reactions is the initial, relative kinetic energy, based on the *relative* velocity v_{rel} of the two soon-to-be-colliding reactants, which approach each other in a crossed beams manner. See Figure 1.2.
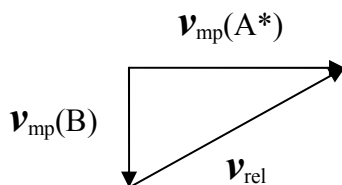
Figure 1.2: The relative velocity vector diagram for a crossed beams experiment. v_{rel} is given by $v_{rel} = v_{mp}(A^*) - v_{mp}(B)$ in order to abide by the convention that v_{rel} should point in the direction of the atomic beam in an atom-molecule system. v_{mp} is the most probable velocity of gas particle A or B. The calculation of v_{mp} is shown in detail in the Appendix.

Others refer to the relative velocity as the *asymptotic* velocity, referring to the flat part of the A* + B potential curve ($R \rightarrow \infty$) shown in Figure 1.3, which illustrates the classical interpretation of PI, the "two potential model" potential energy diagram. With μ as the reduced mass, we define this relative kinetic energy as the *initial energy of the system*, E:

$$E = \frac{1}{2} \mu v_{rel}^2 \qquad (1)$$

E is the total energy, *excluding excitation of* A*, of the A* + B system, and it remains

constant throughout the reaction. E is often called the collision energy. (Figure 1.3 clearly

shows that the excitation energy of A is not included in E.) To conduct kinetic energy

dependence studies, we heat the less massive reactant. This produces a larger change in E than

heating the more massive reactant because less massive objects move faster, via KMT, and E is

proportional to the square of the relative velocity. [Ohno attempts to perform kinetic energy

studies, using time of flight methods[35,36]. We feel that this method, which uses pulses of

metastable beams with a Maxwellian distribution, does not provide a definite kinetic energy.

This is due to fast metastables at the back end of the pulse colliding with slower metastables at

the front of the pulse, which transfers energy to the slower metastables and clouds the energy

distribution that one calculates from the velocities of the metastables. The Ohno group describes

this as two-dimensional PIES. The two dimensions are the ejected electron kinetic energy and

the kinetic energy dependence.] The information that we learn from kinetic energy studies is

dynamical information, where dynamics refers to the *forces* at work during the collision event.

The forces, of course, can be repulsive or attractive. Whether the electron ejection occurs while

the interaction between the colliding species is attractive or repulsive is determined by the

deviation of the energy $\varepsilon(R_i)$ from ε_0. See Figure 1.3. $\varepsilon(R_i)$ is the kinetic energy of the electrons

that are ejected during a PIES experiment and, therefore, equals the difference in energy between

the A* + B and the A + B$^+$ + e$^-$ potential energy curves (V_0 and V_+, respectively) at the distance

where electron ejection occurs, R_i. ε_0 is the difference between the excitation energy E* of A*

and the ionization potential IE of B: $\varepsilon_0 = E*(A*) - IE(B)$. In other words, ε_0 is the kinetic energy

of ejected electrons if ejection occurred at infinite separation, that is, a value based purely on

orbital energies. Of course, electron transfer occurs at much smaller R than infinity, the result of
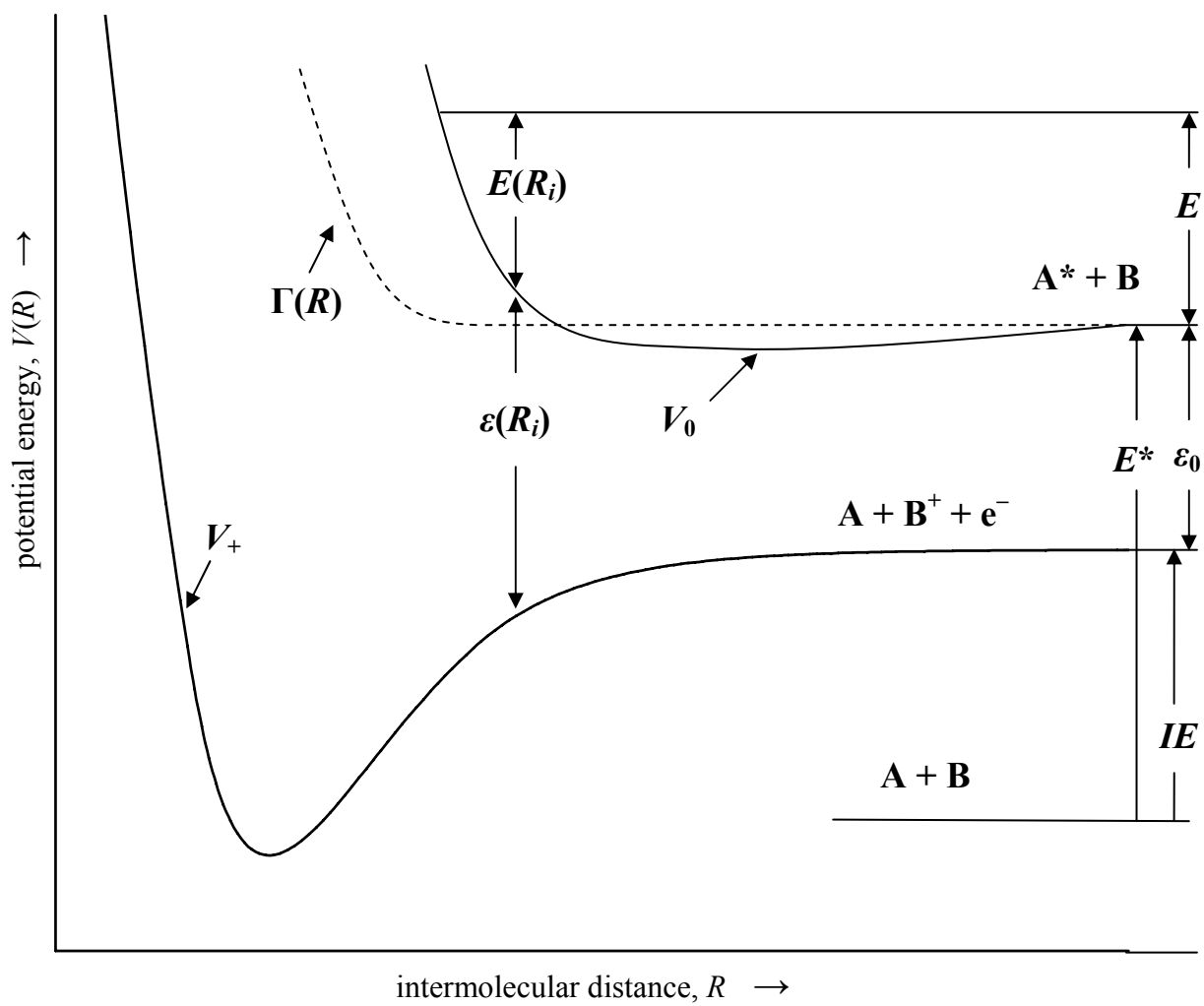
Figure 1.3: The two potential model for PI.

forces at work when the donor and acceptor orbitals of the reactants are in close proximity. If reaction occurs, then, $\varepsilon(R_i)$ will differ from ε_0 because the potential energy curves of the reactants and products are not horizontal straight lines; *the colliding reactants interact*.

One can view the upper curve (V_0) as being "correct" or "in operation" from large R up until the point of electron ejection, that is, on the incoming trajectory. At $R = R_i$ the bottom curve "turns on" and becomes the "correct" indicator of the potential energy situation for whatever species are formed from the collision. For our model the V_+ curve describes the products $A + B^+ + e^-$ on their journey away from the collision, the outward trajectory. Other products are possible and result from associative, dissociative, and rearrangement ionization. If, for example, the product $[AB]^+$ forms during the reaction, it can be trapped in the potential well of V_+. This would not, however, affect the kinetic energy of the ejected electron that is measured in the PIES experiment. (More on this below.) Note that the irreversible, vertical $\varepsilon(R_i)$ transition of Figure 1.3 can occur from two different regions of the upper curve – the attractive well, where $V_0 < 0$, or the repulsive region, where $V_0 > 0$. The point where a potential curve (e.g., V_0 or V_+) changes sign is called the zero-crossing point. Ionization over the attractive well yields $\varepsilon(R_i) < \varepsilon_0$. (Note that since there is a well, it is theoretically possible that several values of R can yield ejected electrons of the same kinetic energy.) When the actual kinetic energy of the electron, $\varepsilon(R_i)$, is less than the prediction based solely on orbital energies, ε_0, scientists say that the transition is "shifted to the red". Ionization over the repulsive region gives $\varepsilon(R_i) > \varepsilon_0$, and the transition is "shifted to the blue". It is crucial to note that this qualitative shift idea, the comparison of ε_0 to $\varepsilon(R_i)$, which is necessary if we are to explain PIES in any simple manner, depends on the approximation that V_+ is nearly flat up until the point of electron ejection. This

approximation is bolstered by the fact that A* has a very large radius, which induces a repulsive interaction between A* and B at much larger R than the R at which A and B^+ experience repulsion. Thus, the crossing point of V_0 occurs earlier in the collision than does the crossing point for V_+. The red shift/blue shift concept requires that the total collision energy E, as described above, be conserved for the entire process. An attractive interaction between A* and B accelerates the reactants toward each other, increasing their kinetic energy. If electron ejection occurs at this point, the ejected electron must carry away less energy than ε_0. A repulsive interaction between A* and B causes the reactants to slow down as they approach. If electron ejection occurs at this point, the ejected electron must carry away more energy than ε_0. We can express this relationship mathematically as follows:

$$E = V_0(R_i) + E(R_i) = V_+(R_i) + E'(R_i) + \varepsilon(R_i) \tag{2}$$

$E(R_i)$ is the reactants' kinetic energy at R_i, $E'(R_i)$ is the products' kinetic energy, and $\varepsilon(R_i)$ = $V_0(R_i) - V_+(R_i)$. In general $E(R)$ is the classical, local, heavy-particle kinetic energy, including centrifugal energy, and $E(R)$ is proportional to the square of the local, relative velocity of the particles. In attractive interactions, the relative velocity of the reactants increases as the collision occurs, increasing $E(R)$. In repulsive interactions, the relative velocity of the reactants decreases as the collision occurs, decreasing $E(R)$. $E(R)$ is not directly measurable. The interplay between $E(R)$, E, and V_0 is reflected in the upper curve of Figure 1.3. An experiment at only one temperature provides red shift or blue shift information for that E alone. By performing the experiment at different temperatures, we can monitor how an increase in E affects the kinetic energy of the ejected electron, that is, monitor the change in the magnitude of the red or blue

shift, and gain information about the shape of the upper curve (A* + B) up to the point of electron transfer. Repulsive interactions are the most common type, and the A* + B potential energy curves often have shallow wells. Attraction can be found in cases where the target molecules have unpaired electrons and spin states which allow for electron transfer.

In addition to the classical properties in Figure 1.3, we find the quantum property, the resonance width $\Gamma(R)$, which has the unit of energy and is closely related to Fermi's Golden Rule. Namely, $\Gamma(R) = 2\pi\rho_\varepsilon \left| V_{0\varepsilon}(R) \right|^2$. (Since PIES involves ionization, some call $\Gamma(R)$ the ionization width.) Stated in this form, $\Gamma(R)$ can be understood in terms of the mechanism described by Miller[37]. As Miller posits, V_+ in Figure 1.3 represents *a single state* of the $(A\text{-}B)^+ +$ e^- system, which dissociates to ground state A and ground state B^+. In fact, this curve is the lower bound of a *continuum* of states of this system. What leads to the continuum? The ejected electron is not bound, and, therefore, its energy is not quantized, so the energy between V_0 and V_+ is continuously variable, leading to a continuum of states. For this reason Miller describes PI as the "leakage" (i.e., transition) from the discrete state found on the V_0 curve to a state in the continuum that is degenerate with it. These suppositions are represented in our Γ equation where ρ_ε is the density of states in the continuum and $V_{0\varepsilon}(R)$ is the coupling (i.e., an integral that must be evaluated) between the discrete and continuum states. The stronger the coupling, the more likely it is that a transition will occur. (More precisely, $V_{0\varepsilon}(R)$ is the transition matrix element between the two states involved in the transition, and, when appropriate wave functions are used, the resonance width is expressed as $\Gamma(R) = 2\pi \left| V_{0\varepsilon}(R) \right|^2$.) A more thorough description for $\Gamma(R)$ and $V_{0\varepsilon}(R)$ is found elsewhere[38], but a further qualitative description of $\Gamma(R)$ can be found in Section 2.2. It is important, however, to note that PIES theory and scattering theory in general

often combine V_0 and $\Gamma(R)$ to form an optical potential, $V_{opt}(R) = V_0 - (i/2)\Gamma(R)$, where $\Gamma(R)$ maintains its description from above. V_{opt}, however, accounts for flux loss from an inelastic process such as reaction or ionization in the case of PIES. [4] Further, V_{opt} enables collision dynamics and cross sections (typically reported in cm^2 or $Å^2$) for PI to be evaluated independently of the fate of the $[ABC]^+$ complex shown at the start of Section 1.1.

In addition to dynamical information, PIES yields information about the population of the electronic and vibrational levels of the dawning Penning ions (not the neutral target molecule). Since the electrons produced in PIES are ejected essentially instantaneously, the electrons provide us "real time" or "snap shot"-like information about which electronic and vibrational levels are occupied. This is, of course, the general situation that we find in photoelectron spectroscopy. For emission from non-bonding or weakly bonding or weakly anti-bonding MO's, we expect that the nuclear arrangement of the ion will be very similar to that of the neutral molecule. This leads to strong overlap of the $v = 0$ and $v' = 0$ vibrational levels in a Franck-Condon (FC) sense, indicating that vibrational excitations are weak and long vibrational progressions will not be seen. Conversely, emission of an electron from a strongly bonding or strongly anti-bonding MO should result in significant nuclear rearrangement. Therefore, the upper potential well will be shifted to a longer or shorter r_e, respectively. This leads to *vertical transitions* that are stronger for $v = 0$ to $v' \neq 0$, implying that a significant vibrational progression will be evident. The $v = 0$ to $v' = 0$ transition above is called the *adiabatic transition*, and Table 1.3 contains a brief list of adiabatic ionization potentials, the energy required to produce such a transition, for molecules that we are currently investigating in the Siska group: H_2, N_2, O_2, CO, NO, CO_2, N_2O, and C_2H_2. Note that such a simple description as a $v = 0$ to $v' = 0$ transition only

applies to a molecule, such as hydrogen, with one normal mode of vibration. The H_2 ionization spectrum is simplified even further because it has only one occupied MO. CO_2, however, has four normal modes of vibration, two of which are degenerate, and eight occupied valence MO's. Thus, an "adiabatic transition" can occur from each occupied MO of CO_2. Ionization of the HOMO ($1\pi_g$) gives the so-called X state. Ionization of the next highest-lying MO ($1\pi_u$) gives the A state. Next is the B state, then the C state, and so on. Now, for example, within the X state any of the three energetically-distinct normal modes can be excited, and it makes no sense to discuss a $v = 0$ to $v' = 0$ transition. The only correct way to indicate the adiabatic transition for the X state of CO_2 is $(000)\,^2\Pi_{g,3/2} \leftarrow (000)\,^1\Sigma_g^+$. The set of zeros ($v_1v_2v_3$) indicates the vibrational modes, the symmetric stretch (v_1), the doubly degenerate bend (v_2), and the antisymmetric stretch (v_3). In C_2H_2 there are seven normal modes and, for example, the adiabatic transition for the X state is written as $[00000]\,^2A_g \leftarrow [00000]\,^1\Sigma_g^+$. v_1 is C−H symmetric stretching, v_2 is C−C symmetric stretching, v_3 is C−H asymmetric stretching, v_4 and v_5 are doubly degenerate bending modes. Thus, an adiabatic transition occurs when a molecule that is in its vibrational ground state, that is, *all normal modes are in the ground state*, is ionized into an ionic state (be it X, A, …) in which *all normal modes are in the ground state*. This is the lowest energy transition (that produces an ion) that can occur within an electronic state, and this energy is traditionally called the "ionization energy" of an orbital. Further, then, this means that all progressions that involve excitation of a single vibrational mode (e.g., $[v_10000] \leftarrow [00000]$, $[0v_2000] \leftarrow [00000]$, etc.) must originate from the same energy. In the analysis section of this dissertation, peak assignments will be made on the spectra that are based, in part, on excitation of normal modes of vibration. Such a discussion, however, depends on the validity of the Born-Oppenheimer approximation[39] to the particular transition. When this approximation is (nearly) correct, the

potential surface of the ion is very similar to that of the neutral molecule, and intense transitions are expected. As there is with C_2H_2's A state, however, there is a change in symmetry, and the [00000] ← [00000] transition is very difficult to determine precisely.[40] The Born-Oppenheimer approximation and the closely related Franck-Condon principle are discussed in relation to spectra and how to explain their origins in Section 3.2.

2.0 EXPERIMENTAL

2.1 VACUUM SYSTEM

To examine the reaction of Ne* with our target molecules, we must get rid of other gases, so the

PIES experiments are performed under high vacuum conditions in a non-magnetic, stainless steel

"box". The main chamber has inside dimensions of 32.5" × 31" × 24" and is accessed via a

removable 39.5" × 31" × 1.25" aluminum cover, which acts as one of the chamber walls. The

main chamber houses the reaction center and the buffer chambers for A* and B. The metastable

(A*) beam source is dubbed the primary source, and the target (B) beam source is called the

secondary beam source. The primary and secondary beam sources are mounted on separate

stands with casters, allowing us to "plug" each beam source into the appropriate buffer chamber.

The castered stands allow for relatively easy removal of the source chambers for maintenance.

An overhead view of the instrument is shown in Figure 2.1. A high vacuum is obtained by first

pumping each chamber with *mechanical pumps*. The main and secondary (source and buffer)

chambers are pumped with Alcatel direct drive (no belts) mechanical pumps (Model 2033 and

2033C, respectively). The secondary pump's parts are Teflon coated to resist chemicals,

allowing us to examine radicals such as NO or other nasty molecules. The primary chamber

(source and buffer) is first pumped with a Welch Duo-Seal Vacuum Pump (Model 1397). Two

smaller Alcatel pumps (M2004A) are used to pump out the HeI lamp, the primary and secondary
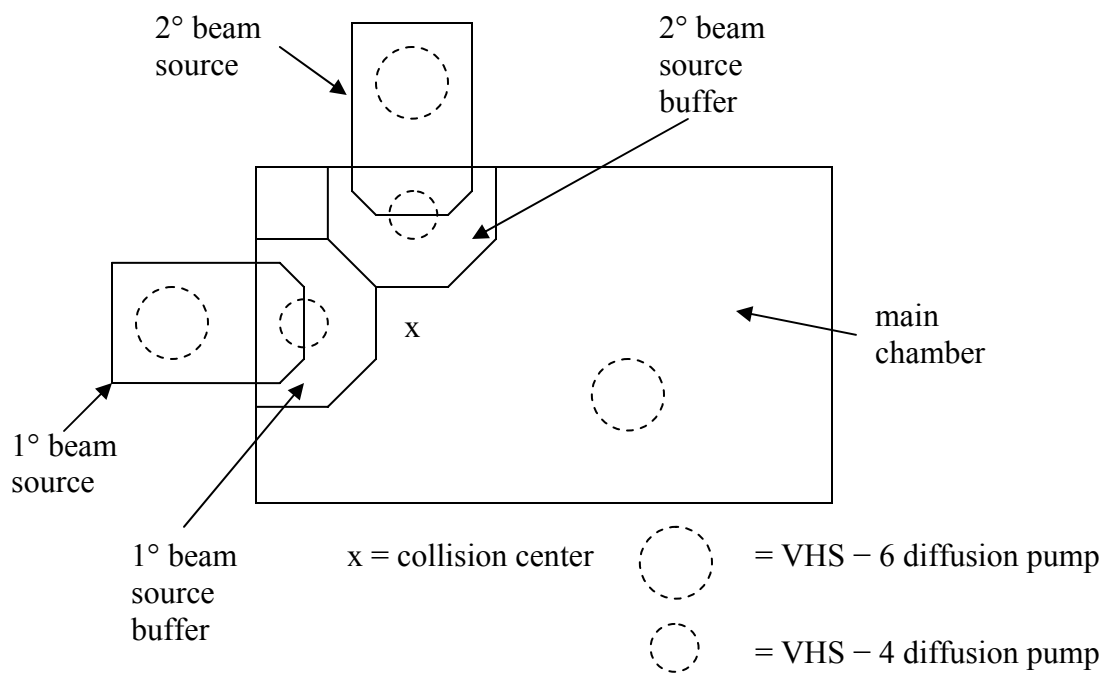
Figure 2.1: The five regions of our crossed beams PIES instrument.

gas manifolds, and the quench lamp, which is part of the electron gun. Once the mechanical pumps have reduced the pressure to 0.1 torr, bellows are used to close them off from the respective region, allowing us to open all five regions to *diffusion pumps* (dp's) (Varian VHS − 6 and VHS − 4 models) via gate valves. The mechanical pumps remain open to the dp's as the dp's operate. These dp's operate by vaporizing silicon oil and cooling the vapor as it rises. As the cooled oil sinks back into the dp, it draws gaseous particles down with it, creating a better vacuum. Ultimately, we achieve a pressure of roughly 3×10^{-7} torr in the main chamber and pressures of roughly 5×10^{-8} torr in the primary and secondary chambers.

2.2 GAS INTRODUCTION

Figure 2.1 shows that the reactants are shot at each other at a right angle – the so-called "crossed beams" experiment. The beams are supersonic and have high centerline intensity, narrow velocity distribution, and high number density. This type of beam is produced, as opposed to a simple effusive beam, through the use of a gas nozzle with a 76 μm diameter orifice. This "bottleneck" produces pressures on the order of several thousand torr and, therefore, many collisions that virtually eliminate any velocity component that is perpendicular to the beam of gas. Stated simply, the high number density allows for many collisions and a large number of ejected electrons, *which is our signal*. This is a common sense idea. A narrow velocity distribution, however, helps us in a more sublime way. Referring to Figure 1.3, you will note that E is drawn as a sharp line. Is this possible? Let us begin by imagining that we could create collisions of identical E by having identical velocities for each reactant. Even at this

20

hypothetical, infinitely sharp E, transitions can still, theoretically, occur at *any R* between the turning point and large R, because the transition process is governed by the quantum mechanical quantity $\Gamma(R)$, which we mentioned in Chapter 1. $\Gamma(R)$ becomes significant, however, only at smaller R due to the increased overlap of orbitals at shorter distances; $\Gamma(R)$ is proportional to orbital overlap. Hickman and Morgner qualitatively describe $\Gamma(R)$ as "the ionization rate as a function of internuclear separation."[41] (Strictly speaking, $\Gamma(R)/\hbar$ is a rate constant because this gives the unit s^{-1}.) Concomitantly, the probability that a reaction will occur becomes significant only at smaller R. Thus, the quantum nature of $\Gamma(R)$ dictates that ***identical** transitions occur over a small **range** of R values around R_i*. Now, let us allow E to cover a small range of values, as it does in the actual case with a real velocity distribution, meaning that there is now a spread in the turning points for the various E's. For example, the largest E in the distribution has the turning point of smallest R. This spread in E, coupled with the increase of $\Gamma(R)$, enlarges further the range of R values for which ***identical** transitions* can occur. From Figure 1.3 transitions at different R_i's give different $\varepsilon(R_i)$'s which we record as peak broadening. Thus, more definite E's produce sharper peaks, justifying the use of supersonic nozzles. In addition to producing the supersonic beams, these nozzles can be heated (with wire-wound ceramic rods that surround it) or cooled (by sending liquid nitrogen through the water cooling lines) to generate beams at different temperatures, allowing us to conduct experiments at different kinetic energies E. Further, we eliminate (we hope) any Doppler broadening by having the axis of the lens entrance positioned 90° from the collision plane.

The primary beam source's electron gun, noted above as the means to excite A to A*, is designed to excite, in our case, noble gases via a head on collision. This produces in the case of

helium two metastable states: He*($1s2s$ $^1S_0$) and He*($1s2s$ $^3S_0$). For all of the other noble gases, we get $^3P_{0,2}$ states from electron configurations np^5 (n + 1)s. In particular, and more explicitly, we get the following for neon: Ne*($2p^53s$ $^3P_2$) and Ne*($2p^53s$ $^3P_0$), with a 3.35 ± 0.20 : 1 J = 2 : J = 0 intensity ratio.[42] When resolving peaks, therefore, we must account for peaks due to both states of Ne*. Now, the electron gun produces many excited states, not just the ones shown above. For example, the configuration Ne*($2p^53s$) also produces the states $^3P_1$ and $^1P_1$. Why then do we say that only $^3P_2$ and $^3P_0$ are important? $^3P_2$ and $^3P_0$ are *metastable states*, states that are long-lived on a molecular timescale. General selection rules, the rules that must be obeyed for a transition to occur, require that ΔJ = 0 or ± 1 (but J = 0 to J = 0 is forbidden), ΔL = 0 or ± 1 (but L = 0 to L = 0 is forbidden), and that ΔS = 0. Thus, a transition from any ^3P state to the ground state of neon $^1S_0$ is spin-forbidden because ΔS = −1. Since the $^3P_1$ state is, however, not present in the reaction center it (and certainly other states) must find a way to radiate its energy quickly via an alternate pathway that *is* allowed. The $^1P_1 \rightarrow$ $^1S_0$ transition has ΔJ = −1, ΔL = −1, and ΔS = 0, indicating that it is fully allowed.   The gun also contains an optical absorption lamp that allows us to select the metastable state ("state select") we wish to examine. (The phrase often used for this process is "quenching".) The state selection lamp operates by exciting one metastable atom, the one we wish to remove, further to an electronic state that is not forbidden from relaxing to the ground state, $1s^2$ $^1S_0$. For example, a He resonance (quench) lamp (20582 Å light) induces the appropriate transitions that remove the $1s^12s^1$ $^1S_0$ state, leaving only the $1s^12s^1$ $^3S_0$ state.

Additionally, our PIES device has a windowless He I discharge lamp which is positioned antiparallel to the metastable beam. This high voltage (2.4 kV) lamp is run at a pressure of ~2

torr, and most of the He is pumped away before it reaches the main chamber. The main chamber pressure does, however, rise to about 3×10^{-6} torr when the lamp is in operation. The 584 Å (21.21804 eV) photons that are produced by this lamp are used to calibrate (peak position and transmission of electrons) the instrument through well known photoelectron spectroscopy (PES) data. Examples of this are presented in Chapters 3 and 4.

2.3 ANALYZER, LENS, AND MULTIPLIER

The final major component of our spectrometer is the analyzer, the Comstock AC-901 160° spherical sector electrostatic energy analyzer, and the Einzel lens, Comstock model EL-301. Figure 2.2 shows these crucial parts, which are made from oxygen free copper, with the exception of portions of the end cap. The data that were collected for this paper were collected only after repeated cleanings. While some of this difficulty might be attributed to the study of gases such as NO and O_2, there were times that three cleanings over a span of more than a week did not produce a working instrument. No experiments could be run during this time. After all of the data for this dissertation had been collected, the Cu apertures of the end caps were replaced with Mo apertures. At first, this has produced phenomenal improvement in instrument performance and reliability. Further, the current Mo apertures will be replaced with others that have a smaller diameter to improve instrument resolution. A grounded entrance cap performs the first step of the collimation process of the ejected electrons. "Grounded" means that electrons that come into contact with the cap are whisked away, through a conductor, to the earth − the ground! The electrons next encounter the lens, which lies 0.55" above the collision center
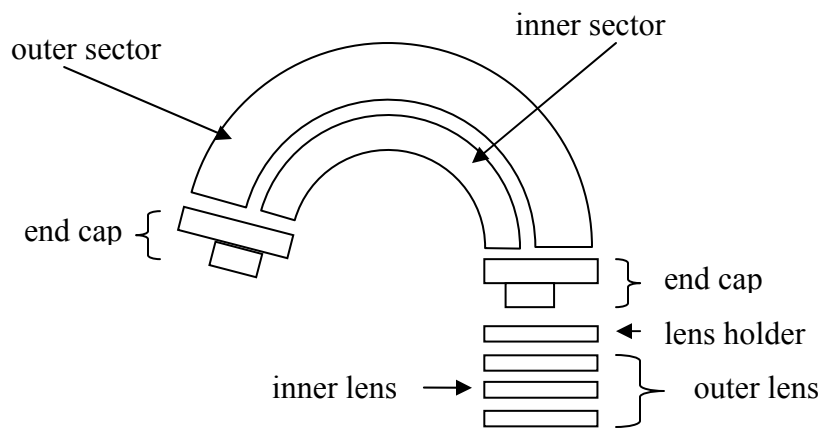
Figure 2.2: The electrostatic analyzer and Einzel lens. Side plates are not shown.

and is perpendicular to the plane of the molecular beams. The lens, which is a series of three "plates" (hole diameter = 2 mm), captures electrons that wander into its 0.002 sr acceptance angle, accelerating them in order to focus[43] them into the analyzer. The acceleration and subsequent focusing is achieved by a combination of voltages applied to the inner lens (+55 V) and the outer lens (+20 V). Typical voltages are shown in parentheses. See Figure 2.3.

After being focused the electrons traverse the sectors and, ultimately, reach the multiplier. This is the physical path of the electrons, but nothing has been said about how we *distinguish* the ejected electrons that have various kinetic energies. To achieve this, first note that we run the experiment at constant pass energy E_p (4.5 eV). "Constant pass energy" means that the *only* electrons that safely pass through the sectors to reach the detector do so with an energy of 4.5 eV. Geometry and applied voltages achieve this according to the equation[44]

$$E_p = \frac{\Delta V}{\left(\dfrac{r_1}{r_2} - \dfrac{r_2}{r_1} \right)}. \tag{3}$$

r_1 and r_2 are the radii of the sectors, 4.05 cm and 3.25 cm, respectively. Thus, $E_p = 2.254\ \Delta V$. ΔV is the electric potential difference (i.e., voltage) between the outer and inner sectors and equals 1.996 V, achieving a pass energy of 4.5 eV. (The average of the sector potentials is the pass energy.) Electrons that have kinetic energies different than this will be cast headlong into the sectors. As described so far, the only *ejected* electrons that can safely reach the multiplier are those with a kinetic energy of 4.5 eV. The way we discriminate between electrons of different kinetic energies is by applying a *ramping voltage*, E_V. As an example of how the ramping
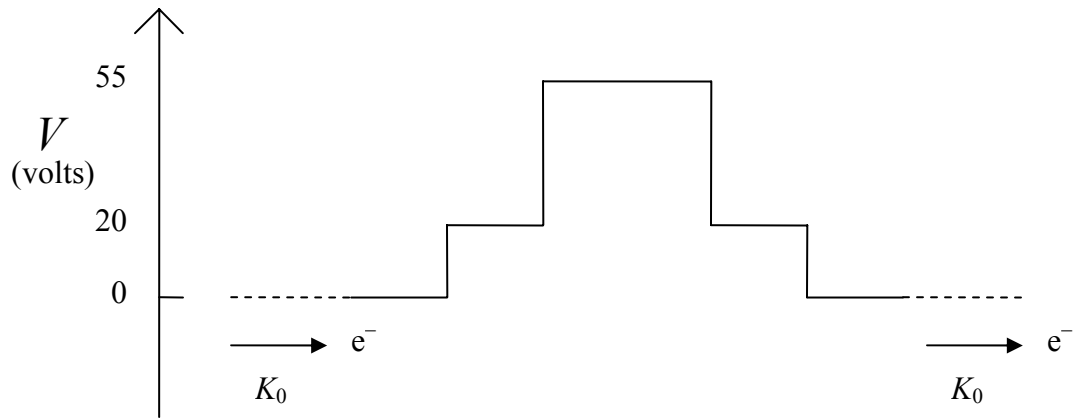
Figure 2.3: Lens voltages as applied to focus an electron of initial kinetic energy $K_0 = 4.5$ eV. The kinetic energy K at any point along the electron's path can be obtained from the formula $K = K_0 - eV$. K_0 is the kinetic energy of an ejected electron, e is the unit of charge (negative for an electron), and V is the applied voltage. While K will change as the electron travels through the lens, the electron will emerge from the lens with $K = K_0$.

voltage works, consider the HeI + N_2 experiment, where we scan for photoelectrons with kinetic energies in the range $0 - 6$ eV, using a ramping voltage range of $+4.5$ eV to -1.5 eV. The ramping voltage is slowly added to or subtracted from (some say "floated on") the initial voltage of the lenses and all of the parts of the analyzer (sectors, end caps, side plates) in small steps (20 meV), maintaining ΔV in Equation 3. At a ramping voltage of $+4.5$ eV (outer lens at $+24.5$ V and inner lens at $+59.5$ V) an electron of 0 eV will be "sucked" into the lens and accelerated to 4.5 eV. When the ramping voltage is at 0 V, electrons of 4.5 eV (if any) that are ejected from the reaction center enter the lens without acceleration or deceleration. In this case, the lens only performs its focusing duties with the lenses at $+20$ and $+55$ V. If an electron has a kinetic energy of 6 eV, a ramping voltage of -1.5 V is needed to slow down the electron to 4.5 eV. Thus, the initial lens voltages pull in many electrons of different kinetic energies, but the ramping acts as a filter, allowing only those with kinetic energy of 4.5 eV to reach their destination. A word about units is clearly in order. We appear to be mixing volts, the unit of electric potential, and eV, a unit of energy. Recall, however, that if a *single* electron travels through an electric potential difference of x V, it acquires x eV of kinetic energy. If an electron is ejected with 2 eV, the ramping voltage must supply an additional 2.5 eV of kinetic energy by applying a voltage of 2.5 V to the path that the electron takes. Thus, we can state $\varepsilon(R_i) + E_V = E_p$, and we can view the ramping voltage, E_V, as the energy in eV that the electron acquires or loses due to the applied potential. Note that we have not paid attention to the sign of the voltage.

The multiplier is a K and M Electronics CERAMAX 7551m channel electron multiplier. The most basic possible description of the function of this detector is that the front end of the multiplier, a cone shaped collector, is maintained at $\sim +200$ V while the back end is maintained

at +2.5 kV. This large potential difference encourages the electron cascade in the electron multiplier.

The final instrument component that we will describe here is the chopper that allows for real time background subtraction. This is accomplished with a tuning fork chopper that allows comparison of the signal when the chopper is open and closed. This counting is managed by the instrument's SR400 Two Channel Gated Photon Counter. Gate A counts when the chopper is open, and gate B counts when it is closed. A Tektronix 2235 100 MHz oscilloscope allows us to monitor the timing of the chopper to ensure that proper counting is maintained. Once the background is subtracted and a good signal to noise ratio is obtained, the voltage ramping, that is, the scan continues. This ends the brief instrument overview that was meant to highlight the key components of our spectrometer that functions as a PES or a PIES device.

3.0 ANALYSIS

3.1 DATA REDUCTION

Table 3.1 contains a summary of the reactions that are examined in this dissertation. Optimally, a two-step procedure is used to collect data on a particular target molecule X: a PES + PIES run of Ne*, HeI + X, followed by a PIES only run of Ne* + X. The different nozzle temperatures in the table for the less massive reactant allow us to achieve different Es, as explained above. In all cases, except that of Ne* + H_2, the less massive reactant is Ne*. The nozzle temperature of the more massive reactant was always 40 °C.

All of the data were analyzed with an in-house FORTRAN program, authored by group leader Peter E. Siska, called gelspec2.for. The peaks are fit to Gaussians through a gradient expansion least-squares calculation, using the Marquardt algorithm [44b]. The fit is assumed to be good after visual inspection and by minimizing χ^2, the square of the weighted difference between the data and the best fit curve. $\chi^2 \approx 5$ is sufficient for most purposes. While the fits generally pass the "visual inspection" test, the χ^2 values for some of the fits in this dissertation are somewhat higher than 5, in some cases nearing 20. The diatomic reactions for which we have Ne*, HeI + X spectra were analyzed as follows. In the first step of the data analysis, the PES + PIES calibration data are fit, where populations from the raw data are input and varied.

Table 3.1: Summary of Reactions

Target molecule	Calibration PIES reaction	Temperature(s) of less massive reactant (°C)
H_2	$Ne^*, He_I + H_2$	40, 200, 400, 600
	$Ne^* + H_2$	
CO	$Ne^*, He_I + CO$	40, 200, 400, 600
	$Ne^* + CO$	
N_2	$Ne^*, He_I + N_2$	40, 200, 400, 600
	$Ne^* + N_2$	
NO	$Ne^*, He_I + NO$	40, 150
	$Ne^* + NO$	
N_2	$He^* + N_2$	40, 200, 400
	$Ne^*(10\% \text{ in He}) + N_2$	
O_2	$Ne_I + O_2$	40
	$Ne^* + O_2$	
CO_2	$Ne^*, He_I + CO_2$	40, 110, 280, 450
	$Ne^* + CO_2$	
C_2H_2	$Ne^*, He_I + C_2H_2$	40, 245, 450
	$Ne^* + C_2H_2$	

The states that are present, the number of peaks in each state (e.g., the length of a progression), and the type of peaks (PES or PIES) are input parameters. For example, since the excitation energy of Ne*, the energy of HeI photons, and the ionization energies of the target molecules are known, the peaks that are present can be identified with relative ease, as discussed further in this Chapter and in Chapter 4. In ambiguous cases, where progressions might overlap or at low ε, repeated fits with different input parameters were performed until a good fit was achieved. Each PES peak is assumed to be a single Gaussian, and, thus, the FWHM was fixed at 45 meV, the resolution of the instrument. Further, the PES peaks were fit with an envelop function that uses the peak ratios and the actual energies from very accurate PES spectra. These accurate PES spectra, therefore, indicate where the PES peaks should be in our spectra. The $J = 0 : J = 2$ peak ratio for Ne* ($^3P_{2,0}$) was assumed to be 0.277 for all of the target molecules in this dissertation. This value can vary up to 0.33, and it is not a simple matter to measure this ratio[45]. (In fact three significant figures are difficult to justify since the ratio measurement was not made and instrument performance is not entirely consistent.) In addition to the populations (i.e., peak heights), the peak widths (FWHM) for the PIES peaks were varied, as were the PES and PIES energies ε. Peaks in the spectrum are shifted from their "true" values due to contact potentials or other instrumental flaws. Once determined by the fit, this *instrument shift*, usually around 0.2 eV, is applied to the entire spectrum. The PIES shift, more generally, the *line shift*, is the most important result we obtain from the calibration and our experiments in general; it details the repulsive or attractive interactions of the reactants, as discussed in Chapter 1. The line shift is fixed for the second step, the fit of the actual PIES spectrum (Ne* + X), and the instrument shift from the calibration is used as an initial guess. The instrument shift is varied in step two. If additional PIES peaks appear in the pure PIES spectrum due to other states, the parameter for the

PIES shift of the additional states was varied in order to fit these additional peaks. This is necessary because the PIES shift can differ greatly from state to state. For both steps 1 and 2, a transmission correction is needed to account for the fact that the Einzel lens is more successful at capturing slow electrons than fast ones. Briefly *and ideally*, PES spectra of N_2, CO, and O_2 are obtained at the prevailing set of experimental conditions at which the PIES experiments were performed. Since the relative peak intensities of N_2, CO, and O_2 PES spectra have been very well documented, comparison of our PES peak ratios to the actual ratios indicates how well or poorly our instrument is transmitting electrons at various energies in current experiments. Generally, the analyzer yields peak heights (counts) at low kinetic energy that are too large and peak heights at high kinetic energy that are too small, and we try to find the best-fit, linear (if possible) correction that shrinks the low kinetic energy peaks and enhances the high kinetic energy peaks. For this dissertation a linear transmission correction was assumed. More on this process is found in Reference 20, and difficulties with it are briefly discussed in Section 5.1.

Before we analyze actual data, it will be helpful to define the line/PIES shift in a less conceptual manner than shown in Chapter 1. If for no other reason, we do this because the initial formulation by Miller was for atom-atom collisions, and we need to include vibrations for diatomic (or larger) molecules. The more general term in the literature is line shift, and we will use that from this point forward. We give the line shift the symbol $\Delta\varepsilon_s$ and define it as $\Delta\varepsilon_s = \varepsilon_p - \Delta\varepsilon_0(J, v')$. ε_p is the peak position (i.e., the measured kinetic energy ε of the ejected electron) of each J state, and $\Delta\varepsilon_0(J, v') = E^*(J) - IE(v')$, which is the difference between the excitation energy of Ne* and the vibronic energy of the target molecules. $\Delta\varepsilon_0(J, v')$ is sometimes called the nominal energy. For Ne $E^*(J)$ represents Ne*($^3P_2$) = 16.6191 eV or Ne*($^3P_0$) = 16.7156 eV. For

all molecules in this dissertation the line shift for each E is assumed to be constant for all v' of J = 0 or 2, given our inability to resolve the difference between the two states. Correspondingly, our fitting program gives us the same $\Delta\varepsilon_s$ for both J states. Of course, the best way to determine if there are differences due to different J states is to use state-selection and run the PIES reactions with a single J state. State-selection has been performed successfully in our lab in the past. Current levels of financial support do not allow for us to refurbish our apparatus to allow for this. Finally, note that throughout this dissertation, we assume that the theoretical PES peak positions are immutable at these experimental conditions; the electron energy levels are not altered by the interaction of the HeI photon with the target molecules. This is the standard assumption for systems that do not involve excitation from very intense sources (e.g., lasers), where the simultaneous absorption of many photons can lead to significant changes in the electron energy levels (radiation or power broadening[46]).

As a specific, explicit example, let us examine the case of CO. Figure 3.1 shows the calibration spectrum, Ne*(40 °C), HeI + CO(40 °C), that has been adjusted for the instrument shift, 0.274 ± 0.002 eV. This spectrum was plotted to determine the quality of the fit of the data; a good fit ensures a reliable line shift $\Delta\varepsilon_s$. The result of the fit of the calibration is $\Delta\varepsilon_s = 0.056 \pm 0.002$ eV. Next, $\Delta\varepsilon_s$ is fixed and the raw data of Ne*(40 °C) + CO(40 °C) is fit, giving Figure 3.2 and allowing us to obtain the population data.

Since there is *only a single vibrational mode* for diatomic molecules, the vibrational progressions are usually easy to assign; this is mostly true here. Note from Table 1.1 that the excitation energy for Ne* ($2p^5 3s\ ^3P_2$) is 16.6191 eV. Thus, based purely on orbital energies, the

first peak in the Ne*($^3P_2$) + CO spectrum would appear at ε = (16.6191 − 14.0139) eV = 2.6052

eV, using data from Table 1.3. If anharmonicity is neglected, additional peak positions in the $^3P_2$

progression would appear at 2.3307, 2.0561 eV, …, given that the vibrational levels are

separated by v = 2214.24 cm^{-1} = 0.274531 eV[47]. (These values only hold if the harmonic

oscillator approximation is valid, that is, $E_v = hc\,\bar{v}\,(v + \frac{1}{2})$. The overstrike on v stresses that

vibrational frequencies (e.g., v_1, v_2, etc.) are often given in units of cm^{-1}. It is convention,

however, to omit the overstrike when, for example, 1244.3 cm^{-1} is listed as "v_1" of CO_2. It

should be clear from context what is meant by the symbol.) The slight shoulder on the right of

the largest peak is assigned to ionization due to Ne*($2p^5 3s\ ^3P_0$), with excitation energy 16.7154

eV. Thus, the first peak in the $^3P_0$ progression should appear at ε = (16.7154 − 14.0139) eV =

2.7015 eV, and the additional, *harmonic* peaks in the progression appear at 2.4270, 2.1524 eV,

… and so on. Since Penning reactions are of a *chemical nature*, however, the peaks are often

shifted from the value based on orbital energies (i.e., the nominal energy). Assigning the first ten

peaks of the spectrum in Figure 3.2 to the $X\,^2\Sigma^+$ state v' = 0 → 9 progression leaves the final peak

unassigned. We attempted to fit the peaks with a $X\,^2\Sigma^+$ state v' = 0 → 10 progression, as well as

a $X\,^2\Sigma^+$ state v' = 0 → 10 plus an $A\,^2\Pi$ v' = 0 peak. The first method yielded a very poor fit of the

peak at low energy, and the second method produced peaks with very large errors in the

populations. The best fit was obtained with a $X\,^2\Sigma^+$ state v' = 0 → 9 progression plus an $A\,^2\Pi$ v'

= 0 peak, but the data near 0 eV are difficult to fit properly. See below. The $A\,^2\Pi$ v' = 0 peak for

Ne* ($^3P_2$) + CO should appear at ε = (16.6191 − 16.5440) eV = 0.0751 eV, and the $A\,^2\Pi$ v' = 0

peak for Ne* ($^3P_0$) + CO should appear at ε = (16.7154 − 16.5440) eV = 0.1714 eV using data

from Tables 1.1 and 1.3. Lescop *et al.* [13] report that the overlap of the A state with the X state

starts at v' = 9. Thus, they fit only through v' = 8 in their paper.
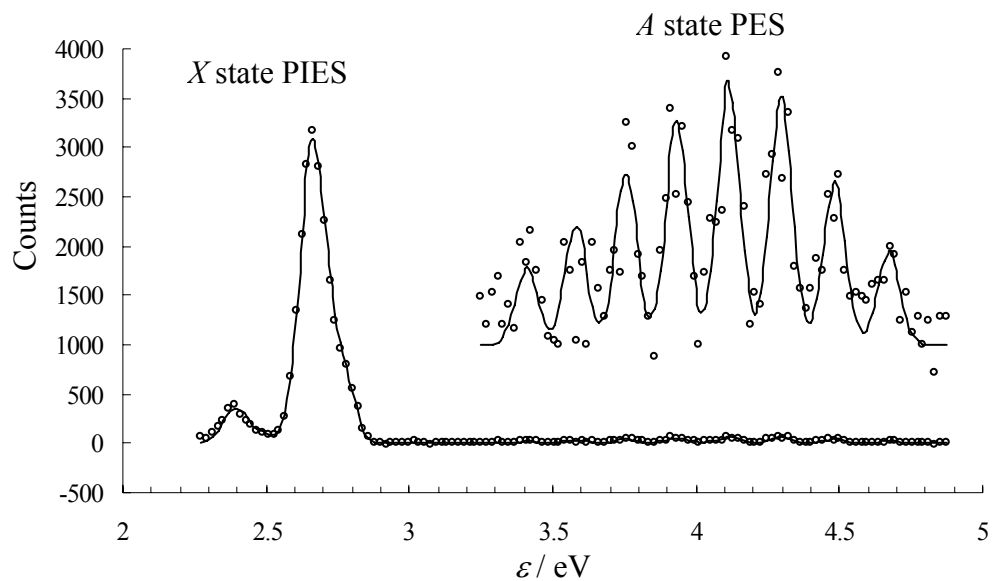
Figure 3.1: Energy-corrected spectrum for Ne*(40 °C), HeI + CO(40 °C). The open circles are raw data, and the smooth curve is the best fit of the raw data. These data are not transmission corrected. The inset shows the envelop function that was used to fit the PES raw data peaks.
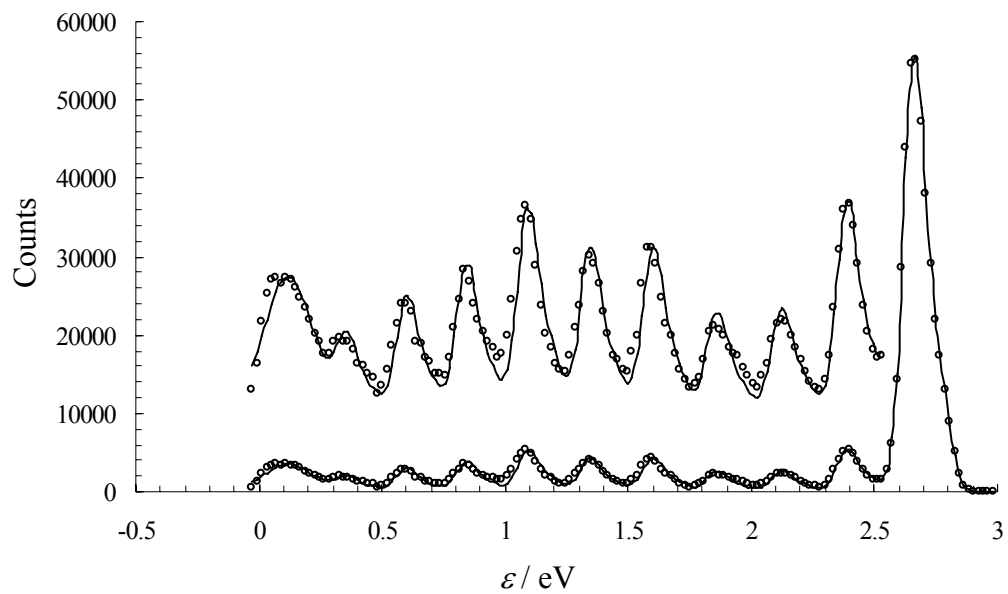
Figure 3.2: Final fit for Ne*(40 °C) + CO(40 °C). The open circles are transmission corrected data, and the smooth curve is the best fit of this data. The inset shows a close up of the fit for the less intense transitions.

The $^3P_2$ progression, adjusted for anharmonicity, is shown in Figure 3.3 in typical "pitchfork" fashion.   The $^3P_0$ progression is shown in Figure 3.4.
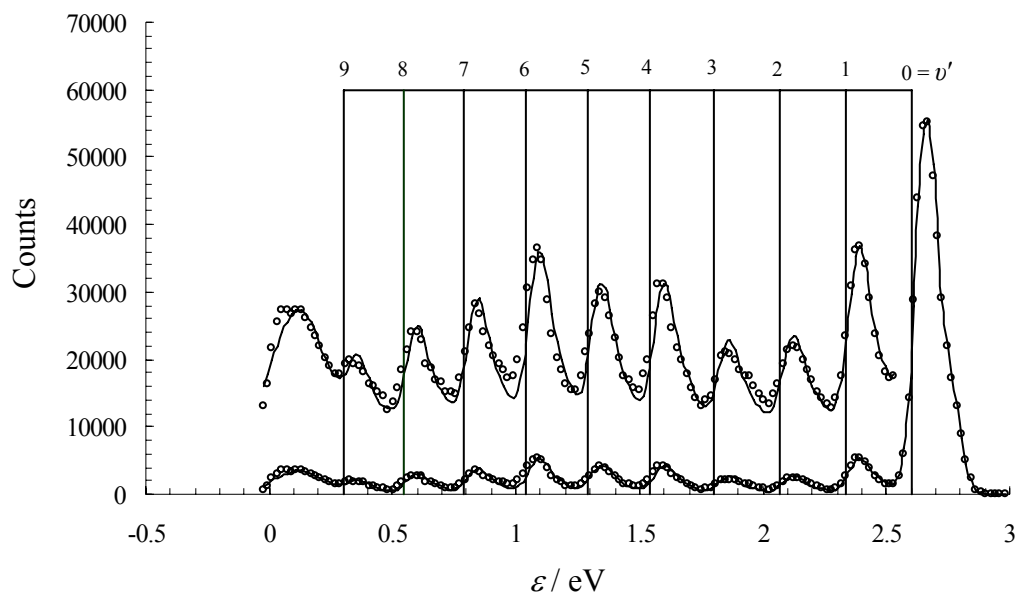
Figure 3.3: Final fit of Ne*(40 °C) + CO(40 °C). The pitchfork shows the position of the $^3P_2$ vibrational progression, adjusted for anharmonicity.
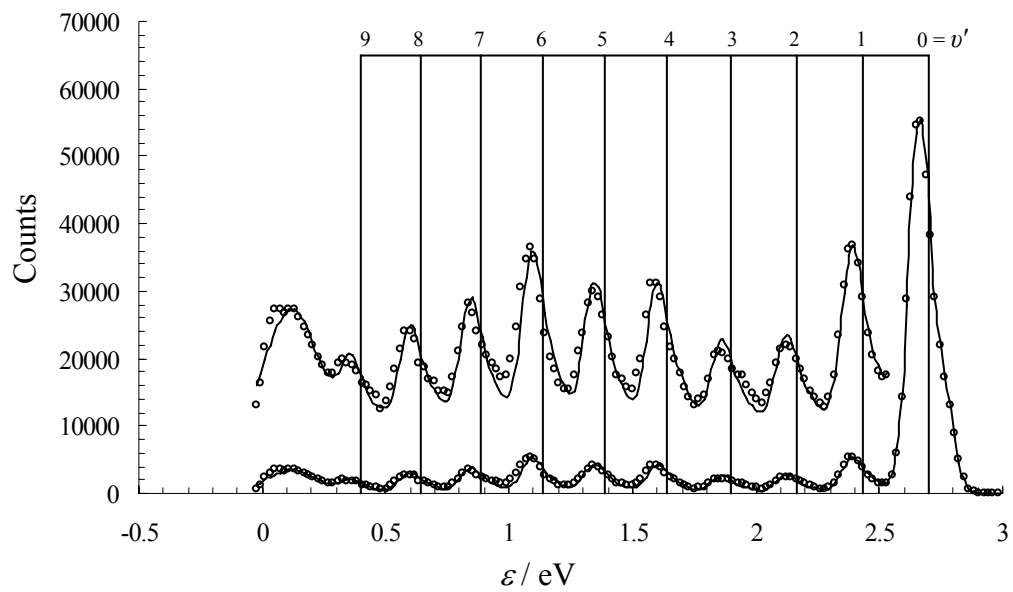
Figure 3.4: Final fit of Ne*(40 °C) + CO(40 °C). The pitchfork shows the position of the $^3P_0$ vibrational progression, adjusted for anharmonicity.

Figures 3.3 and 3.4 clearly show that there is a blue shift, indicating a repulsive interaction between the reactants in the Ne*(40 °C) + CO(40 °C) reaction. Next, we highlight the difficulty of trying to fit peaks at low ε. Figure 3.5 shows a close up view of the near-zero region of the spectrum of Figure 3.3 with the $A\,^2\Pi\,v' = 0$ theoretical values for Ne* $(^3P_2,\,^3P_0)$ + CO shown by vertical lines.
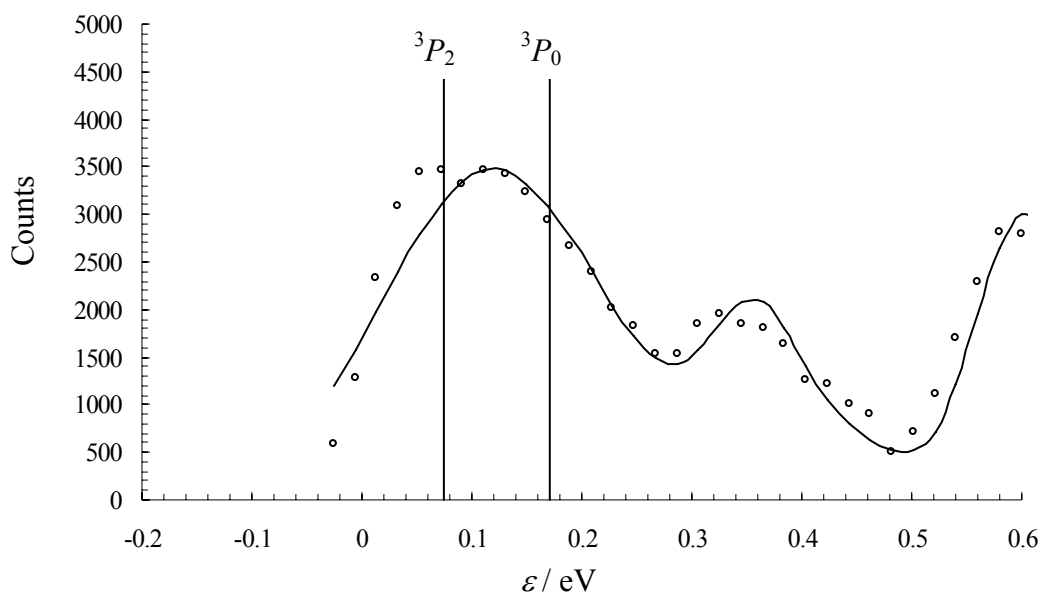
Figure 3.5: Low ε region for Ne*(40 °C) + CO(40 °C).

The first thing to note is that there are two data points that have negative kinetic energies. These points are, of course, meaningless, and they also shed doubt on the nearby points, indicating difficulty in determining the correct energy shift at low ε. A careful examination of the first six data points (at the left) shows that there is a sharp rise in intensity that is not matched on the right side of the first peak. This is also due to the difficulty in transmission correcting data near zero kinetic energy. This problem gets worse at higher E, leading to a peak that looks legitimate but that can not be fit, as we mentioned above. Thus, we believe that this "peak", due to the first 6-8 points of this spectrum, is spurious. This spurious "peak" is present at each E, and it increases in height with increasing E. This dependence on E remains a mystery at this time.

The next step is to reduce the data for the other Ne* + CO(40 °C) reactions with Ne* nozzle temperatures of $T = 200, 400,$ and 600 °C. The result of this is shown in Figure 3.6, where the populations have been normalized for comparison. Note that the blue shift increases with increasing E and that the peaks broaden as E increases. To highlight the increasing blue shift and the broadening of the peaks as E increases, we plot in Figure 3.7 the $v = 0 \rightarrow v' = 0$ transition from Figure 3.6. Note that the above method is less reliable if there is significant overlap of the PIES and PES peaks. If this is the case, one can seed the target gas with a different noble gas (e.g., Xe), providing well resolved peaks and a more reliable energy correction and calibration. The process of data analysis shown above for CO was repeated for H_2, N_2, and NO. The results have been compiled in Chapter 4. The NO fit was, however, very difficult. When the fit of the entire Ne* + NO spectrum was attempted in the usual fashion, the $v' = 0$ to $v' = 6$ peaks of the X state were found to be significantly less intense than what is accurate, and the a state peaks were completely erroneous.
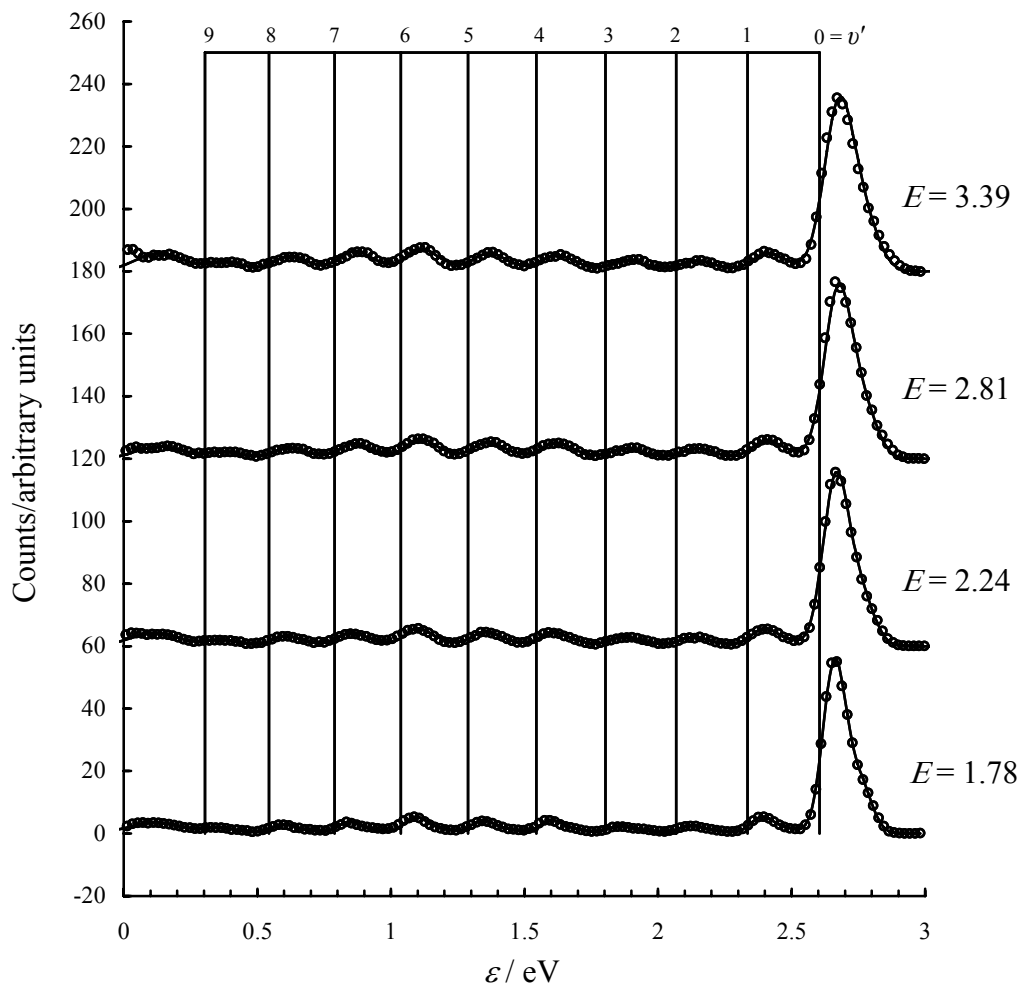
Figure 3.6: Ne* + CO(40 °C) for Ne* at $T = 40$, 200, 400, and 600 °C. The pitchfork shows the position of the ${}^3P_2$ vibrational progression, adjusted for anharmonicity. The data have been normalized to equal intensity for each E(kcal/mol), and the baselines have been shifted for display. The circles are the transmission corrected data, and the solid line is the best fit of the transmission corrected data.
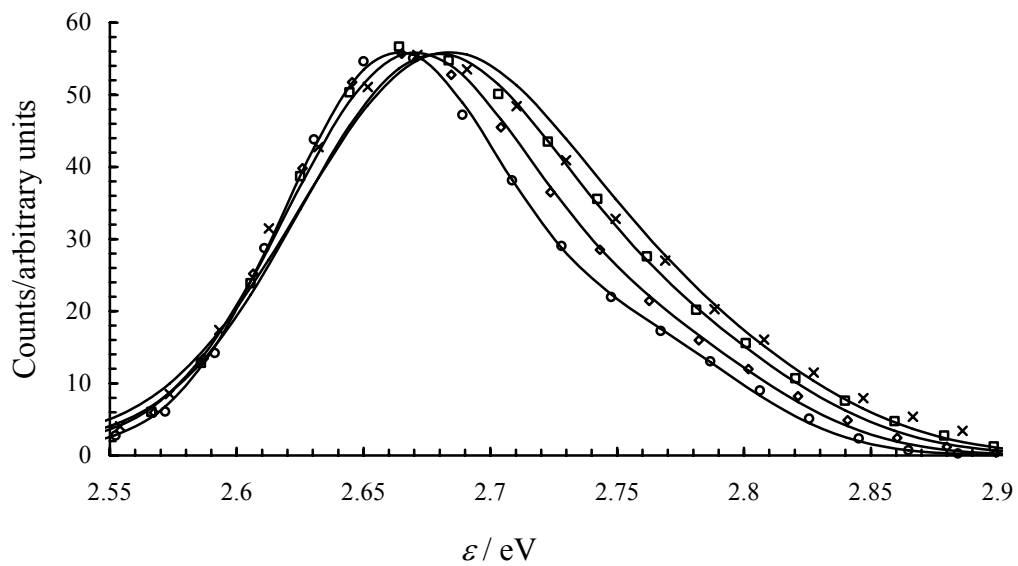
Figure 3.7: The $v = 0 \rightarrow v' = 0$ transition for Ne*(T) + CO(40 °C) at $T = 40$ (circles), 200 (diamonds), 400 (squares), and 600 (×'s) °C. The symbols are the transmission corrected data, and the solid line is the best fit of the transmission corrected data.

The fit of Ne* + NO was only achieved by first determining the line shift from the Ne*, HeI + NO experiment. Second, gelspec2.for was run on the Ne* + NO data to obtain transmission corrected data. Third, the transmission corrected values for the $v' = 0$ to $v' = 6$ peaks of the X state were fixed. Fourth, only the remaining X state peaks were fit, where their heights and widths were allowed to vary as usual. Fifth, all X state peaks were held constant while the a state peaks were fit. During the fifth step, the X state line shift and the instrument shift were not varied. The line shift for the a state, then, is the result of the fifth step.

The Ne* (seeded) + N_2 reaction required a method of analysis that was similar to that of H_2, CO, and N_2. Here, however, there is no separate experiment needed for the calibration. The He* atoms that comprise most of the beam in which the Ne* is seeded serve this purpose. In a seeded beam under supersonic conditions, the kinetic energies of atoms or molecules in the beam are proportional to their atomic or molecular masses, since all particles reach the same average terminal speed.[48] Thus, heavy atoms possess large kinetic energies, leading to large Es. (An analogy is a bunch of ping pong balls (the He atoms) being used to push BB's (the Ne atoms).) Note that E is calculated (from Equation 9 in the Appendix) by using the reduced mass (μ) for Ne and N_2. When calculating the most probable velocity v_{mp} (from Equations 4 and 7 in the Appendix) the average mass of He and Ne is used for m in Equation 4. For Ne and He $m = 5.621$ amu at 90% He and 10% Ne. The calibration was performed by first noting that $\mu_{Ne^*, H_2} / \mu_{Ne^*, N_2}$ = 0.2986. μ is the reduced mass. For the Ne*(seeded beam) + N_2 experiments we have $E =$ 4.06, 5.69, and 7.73 kcal/mol. Thus, for He*(seeded beam) + N_2 $E = 0.2986(4.06 \text{ kcal/mol}) =$ 1.21, 1.70, and 2.31 kcal/mol, respectively. From previous work (no seeded beams) of the group[49] for He* + N_2 we plotted the line shift that was determined from these experiment versus

E. Next, the values of 1.21, 1.70, and 2.31 kcal/mol were located on the graph of $\Delta\varepsilon_s$ versus *E*,

giving the line shift for He*(seeded beam) + N_2: $\Delta\varepsilon_s = 0$ (extrapolated), 4.7, and 12.6 kcal/mol,

respectively. (The error in these shifts is estimated to be ±1 kcal/mol.) Finally, in Figure 4.19

note the peaks for the He* + N_2 reaction (*B* state). In the fitting procedure these peaks were

fixed at the shifts noted above, and the line shift for the Ne* + N_2 reaction was then allowed to

vary (along with the usual instrument shift), yielding the $\Delta\varepsilon_s$ values in the results section.

Like NO, O_2 is reactive and difficult to analyze in the instrument. At present, we only

have a run of NeI + O_2 and a run of Ne* + O_2. Note that there is not the usual calibration run

with HeI. Further, the Ne* + O_2 spectrum contains an underlying continuum of signal that

increases towards zero kinetic energy . See Figure 3.8. This rise in signal that starts around $v' =$

10 of the *X* state of the PIES spectrum is not noise since the instrument is designed to subtract

the background in real-time. See Chapter 2. The problem with rising signal below ~ 0.2 eV, of

course, still remains. Additionally, the NeI + O_2 PES spectrum does not contain this rising

background, as no PI reaction is possible (of course). For this reason we used gelspec2.for to

obtain line and instrument shift values for the O_2^+ $X\,^2\Pi_g$ state $v' = 0 \rightarrow 9$ progression, but in

general the population information will be too unreliable to report. We first fit the NeI + O_2 data

to obtain the instrument shift. (The energies of the $^1P_1$ and $^3P_1$ states of NeI are 16.8483 and

16.6711 eV, respectively. Also, for Ne photons, the higher energy state has the larger intensity,

with a ratio of 0.16 for $^3P_1/^1P_1$.) Similar to NO, we had to hold the first three peak heights fixed

in order to fit the remaining peaks. This instrument shift value was fixed, and the $\Delta\varepsilon_s$ parameter

was allowed to vary to fit the Ne* + O_2 PIES data.
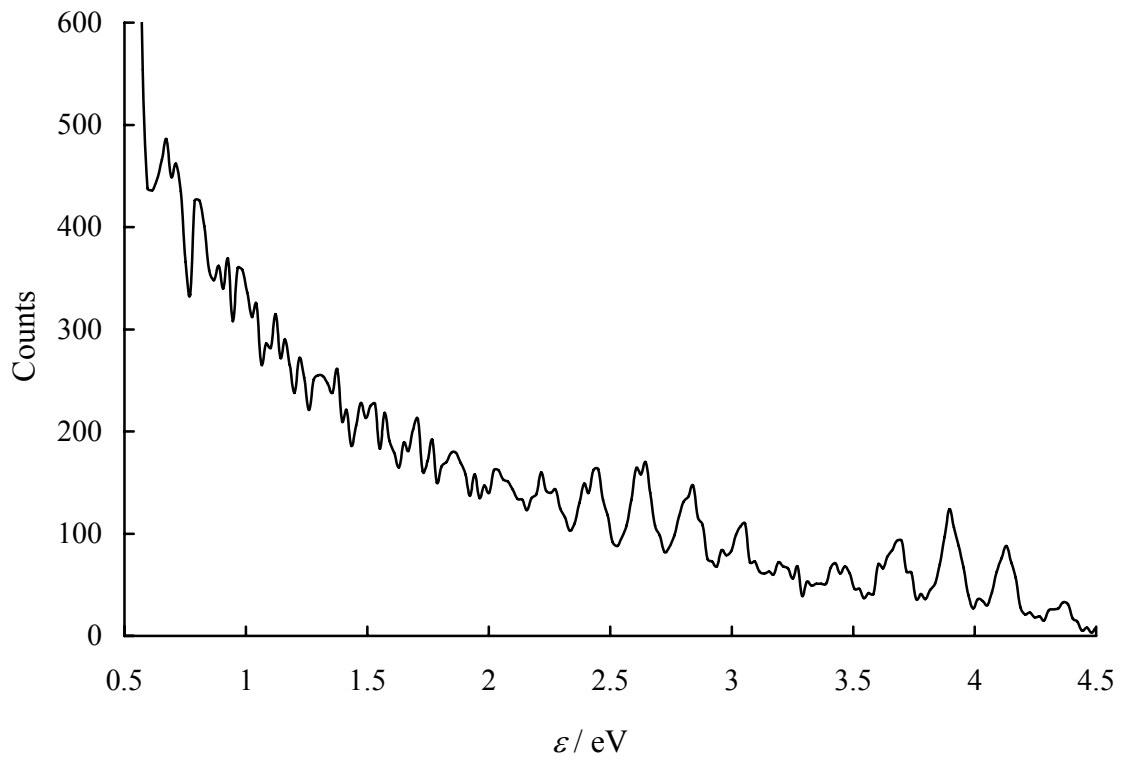
Figure 3.8: Raw data spectrum of Ne*(40 °C) + O_2(40 °C).

For CO_2 and C_2H_2 the situation is more complex than the diatomic case due to the presence of more than one vibrational mode and a general lack of anharmonicity constants for these molecules. At present, the gelspec2.for program has not been sufficiently modified for general, multi-mode analysis of triatomic or larger molecules. This is a goal for the future, given the need to analyze CO_2 more precisely and N_2O, another molecule that has been examined recently by our group[50]. gelspec2.for was modified enough, however, to perform a complete fit of $C_2H_2^+$ (X) and a determination of the line shift for CO_2, as well as a partial fit and peak assignment of the Ne* + CO_2 spectra. This modification was relatively simple because only the symmetric stretch vibrations give significant intensity for the first four peaks of the CO_2 spectrum and the entire X state portion of the $C_2H_2^+$ spectrum. Thus, the fitting is analogous to the diatomic case where there is only a single vibrational mode. The excitation of multiple vibrational modes or combination bands, however, is significantly more complex, and modification to deal with that is a future goal. The line shift for CO_2 was determined by fitting the $n = 0$ and 1 peak (assuming no anharmonicity) of the HeI PES B state progression and the CO_2^+ X state $n = 0$ peak from the nv_1 progression in the calibration spectrum. See Figure 3.9, the raw spectrum for the Ne*(40 °C),HeI + CO_2 experiment. This line shift determination for CO_2 is similar to what was done for the diatomic molecules, but we did not fit the full progressions due to a lack of anharmonicity constants and problems similar to that encountered with NO where the program would not fit a large number of peaks at one time. Figure 3.9 shows, however, that the $n = 0$ peak from the HeI PES B state progression is close to the CO_2^+ X state $n = 0$ peak, and little error should occur from fitting only three peaks. A good fit of the first four peaks of the Ne* + CO_2 spectrum was achieved by assigning these peaks to the $n = 0, 1, 2,$ and 3 peaks of the nv_1 progression. Portions of the CO_2^+ spectrum remain unfit, a problem we explore below. For the

C_2H_2 calibration, the entire PES X state progression and the $n = 0$ and 1 peaks of the $C_2H_2^+$ X state $n\nu_2$ progression were fit, using the anharmonicity constant of 6 cm^{-1} for $\omega_e x_e$ for ν_2 (the CC stretch) from Ruett *et al.*[51], yielding $\Delta\varepsilon_s$.   The Ne* + C_2H_2 runs were fit in the same manner as a diatomic molecule.
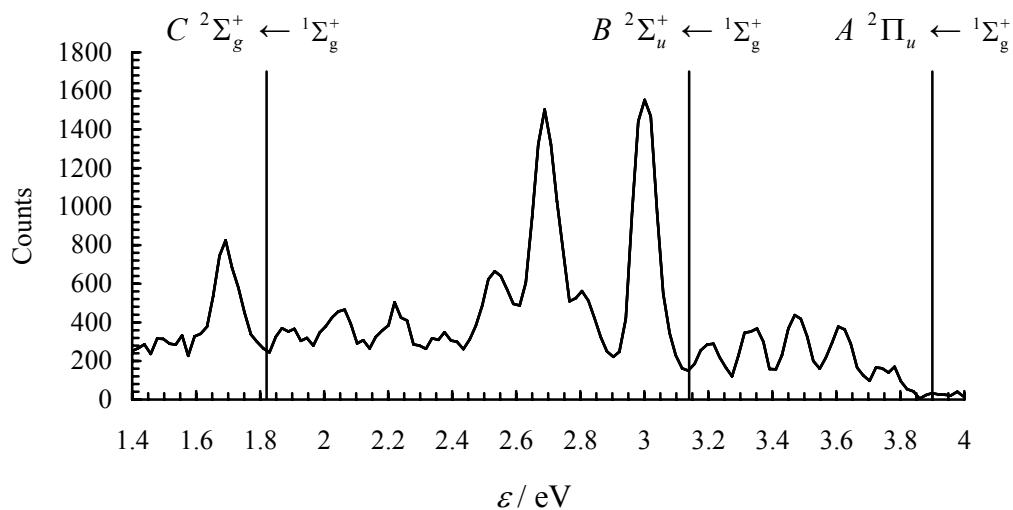
Figure 3.9: Ne*(40 °C), HeI + CO_2 calibration raw spectrum. The vertical lines indicate the literature peak positions for the PES adiabatic transitions for the *A, B*, and *C* states of CO_2^+. Our peaks for these transitions are red-shifted by 0.14 eV. The accepted values for the adiabatic transitions are given by subtracting the values in Table 1.3 from 21.21804 eV.

3.2 POPULATIONS AND FRANCK-CONDON FACTORS

It is common in spectroscopy to compare experimental results to Franck-Condon factors (FCfs), which we discuss immediately. A FCf has the form $|\langle \upsilon | \upsilon' \rangle|^2$ and is, therefore, a measure of the overlap between a vibrational wave function (in vibrational level υ) in the (usually) ground electronic state of the neutral molecule and any vibrational wave function (in vibrational level υ') in any electronic state (e.g., X, A, B, etc.) of the ionic molecule. Quantum mechanically, the probability (intensity) of a transition is proportional to the FCf for the two vibronic states involved in the transition. (More specifically, the transition probability is proportional to the square of the transition moment integral of which the FCf is a part.) In Chapter 4 two key results are presented: $P(\upsilon')/P(\upsilon'_{max})$ and $\dfrac{|\langle \upsilon | \upsilon' \rangle|^2}{|\langle \upsilon | \upsilon'_{max} \rangle|^2}$. The symbol $P(\upsilon')$ is given to the peak area or

population of a transition. For example, the symbol $P(0)$ is the population corresponding to the transition from $\upsilon = 0$ to $\upsilon' = 0$. $P(1)$ is the symbol for the population corresponding to the transition from $\upsilon = 0$ to $\upsilon' = 1$. This notation (e.g., $P(0)$) ignores hot band transitions; it assumes that υ always equals 0. These populations are normalized with respect to the tallest peak in the spectrum for ease in comparison. For example, we make the Ps relative to $\upsilon'_{max} = 0$ for CO and N_2 since these are the tallest peaks in the PIES spectra. Thus, we calculate $P(\upsilon')/P(0)$. For H_2 the $\upsilon'_{max} = 2$, and we, therefore, calculate $P(\upsilon')/P(2)$. Obviously, we get a value of 1 when the υ's are equal.

The ratios of FCfs are calculated in a similar manner. For example, in the case of CO and

N$_2$, the notation that applies is $\dfrac{\left|\langle 0|v'\rangle\right|^2}{\left|\langle 0|0\rangle\right|^2}$. For H$_2$ the notation is $\dfrac{\left|\langle 0|v'\rangle\right|^2}{\left|\langle 0|2\rangle\right|^2}$.

The comparison of populations to FCfs is based on the following outline. The process

starts with the assumption of the validity of the Born-Oppenheimer approximation, which states

that we can treat electronic and nuclear motions separately. Thus, we can write the total

molecular wave function as $\psi_{\text{tot}} = \psi_\text{e}(R,r)\psi_\text{n}(R)$. R represents nuclear coordinates, and r

represents electronic coordinates. This is then substituted into the transition moment integral

where the operator is the dipole moment operator. The key assumption involves finding an

average R for the transition because ψ_e depends on R. The derivation is present in many

textbooks and is still a subject of interest[52]. The key here is that the derived transition moment

integral is proportional to $\left|\langle v|v'\rangle\right|$. As above, its square is the FCf for the transition under

consideration. FCfs are largest when the vibrational wave functions in the lower and upper states

have large amplitudes at the same internuclear separation. A large (small) FCf implies large

(small) intensity for a peak in a vibrational spectrum. Thus, systems that exhibit "FC behavior"

are those for which the *relative* populations ($P(v')/P(v'_{\text{max}})$) of peaks in a spectrum are the same

as the *relative* values of the FCfs, $\dfrac{\left|\langle v|v'\rangle\right|^2}{\left|\langle v|v'_{\text{max}}\rangle\right|^2}$. That is, FCfs are proportional to the observed

populations, *if* the approximations that we described above are accurate. If the relative

populations differ markedly from the relative FCfs, then the electronic transitions that give rise

to the spectrum can't be explained with our simple overlap model. In other words, peaks that

arise from non-FC behavior are not the result of a direct process (e.g., photoionization), a process

that is the result of the overlap a vibrational wave function in the ground state with one in the excited state. In the results section we explore other mechanisms that might be responsible for the observed spectra in this dissertation.

The calculation of FCfs in this dissertation is done via the RKR method[53], using an in-house FORTRAN program called FCfRKR.for. This method is numerical (as opposed to analytical) with input data that consists of spectroscopic constants (vibrational and rotational) for the lower and upper states. First, the program calculates the classical turning points for a vibration (the *only* vibration for a diatomic molecule) of the molecule *assuming that we have standard vibrational wave functions* − a so-called semi-classical inversion method. Second, these turning points are then interpolated to yield potential curves for the lower and upper electronic states. Typical curves are shown in Figure 3.10. Third, the program determines, numerically, vibrational wave functions that fit within these potential curves. Lastly, the FCfs are determined from the integral $\left|\langle \upsilon | \upsilon' \rangle\right|^2$.

The calculation of FCfs for polyatomic (triatomic or larger) molecules is far more difficult than in the diatomic case because there is more than one normal mode of vibration which in general means that one must calculate $3N - 6$ (or $3N - 5$ for linear) dimensional overlap integrals[54], that is, a polydimensional surface is required to represent the potential energy curves[55]. (The single normal mode of vibration in diatomic molecules makes things easy!) The calculation of FCfs in such cases has been explored by many, including Lucas[56], Luis *et al.*[57], and the many references therein. Our efforts will be concentrated here in the near future, and

work such as that of Ibrahim[58] will be of interest, as it concerns linear to bent transitions of linear triatomic molecules. This topic is explored further in Chapter 5 for CO_2 and C_2H_2.
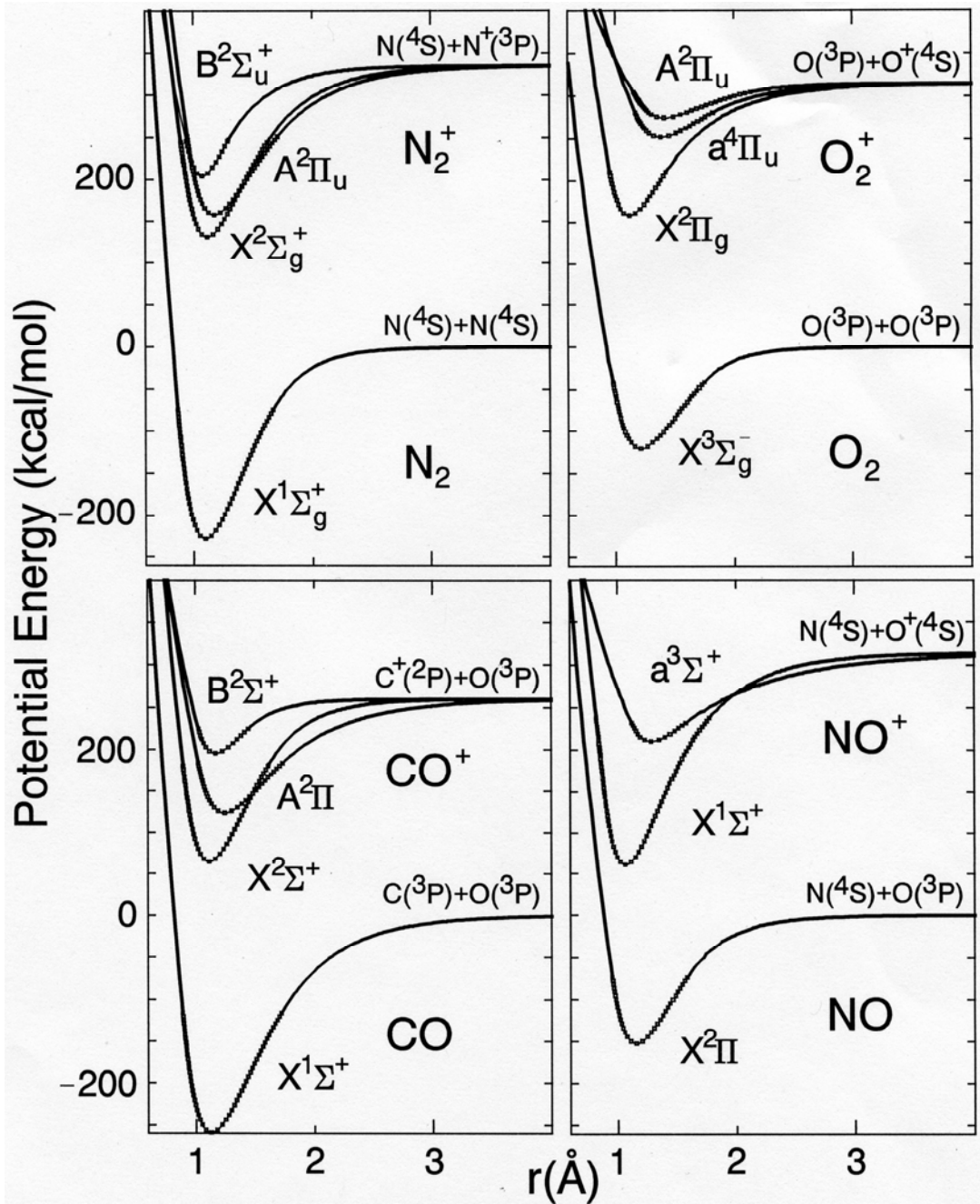
Figure 3.10: Potential energy curves from RKR calculations.

4.0 RESULTS

4.1 HYDROGEN

The final fits of all four Es for Ne* + H_2 are shown in Figures 4.1 and 4.2. For E = 1.83, 2.50, 3.16, and 3.89 kcal/mol, $\Delta\varepsilon_s$ = 64 ± 1, 84 ± 1, 94 ± 1, and 107 ± 1 meV, respectively. These results are shown graphically in Figure 4.3, which contains a point (the square in the plot) that is estimated from the spectrum figure in work by Bussert $et\ al.$.[59] There, they reported $\Delta\varepsilon_s$ = 52 meV for Ne* + H_2 at a thermal energy of $E \approx 1.2$ kcal/mol. Their result falls very nicely in line with ours. The relative vibrational populations (relative peak areas) and relative FCfs for Ne*(3 $^3P_2$) + H_2 are shown in Table 4.1. The error on the $P(v')/P(1\ or\ 2)$ average is the sample standard deviation for the four data points. For all spectra in this paper the populations for the J = 0 state can be obtained by multiplying the J = 2 population by 0.277, the assumed $^3P_0/^3P_2$ peak ratio for Ne*. Table 4.2 contains a comparison of our populations to those of Reference 59. Our results are in fairly good agreement.

Using Tables 1.1 and 1.3, the first peak in the Ne* + H_2 spectrum should appear at ε = (16.6191 − 15.42593) eV = 1.1932 eV. If anharmonicity is neglected, additional peak positions in the $^3P_2$ progression are at 0.9048, 0.6163 eV, …, given that the vibrational levels are separated by v = 2326.6 cm^{-1} = 0.28845 eV. The slight shoulder on the right of the largest peak is assigned

54

to ionization due to Ne*($2p^5 3s\ ^3P_0$). Thus, the first peak in the $^3P_0$ progression should appear at ε = (16.7154 − 15.42593) eV = 1.2886 eV, and the additional, *harmonic* peaks in the progression appear at 1.0002, 0.7117 eV, … and so on. The peaks are assigned to the $X\ ^2\Sigma_g^+$ state $v' = 0 \rightarrow 4$ progression. Figures 4.1 and 4.2, as well as Table 4.1, indicate that, with the fitting procedure used here, there is uncertainty as to which peak is the most intense. (See Chapter 5.) This is most obvious in the middle two runs. If FC behavior is to be observed, the $v' = 2$ peak should be the most intense, and the ratio of the $v' = 1$ peak to the $v' = 2$ peak should be 0.920. The $v' = 2$ peak was the most intense for $E = 1.83$ and 3.16 kcal/mol. The $v' = 1$ peak was the most intense for $E = 2.50$ and 3.89 kcal/mol. It is very unlikely that this oscillatory behavior is the true behavior. To be true to the data, however, Table 4.1 contains two averages, one for which $v' = 1$ is the most intense peak and one for which $v' = 2$ is the most intense peak. See the Chapter 5 for justification, but the results for $E = 1.83$ and 3.16 kcal/mol are believed to be accurate. The plot of normalized FCfs along with the normalized data already presented in the low E plot of Figure 4.1 is shown in Figure 4.4. Our results are nearly in line with FC behavior for $v' = 0$ to $v' = 2$. Beyond that, however, the intensities are well below those predicted by the FCfs.
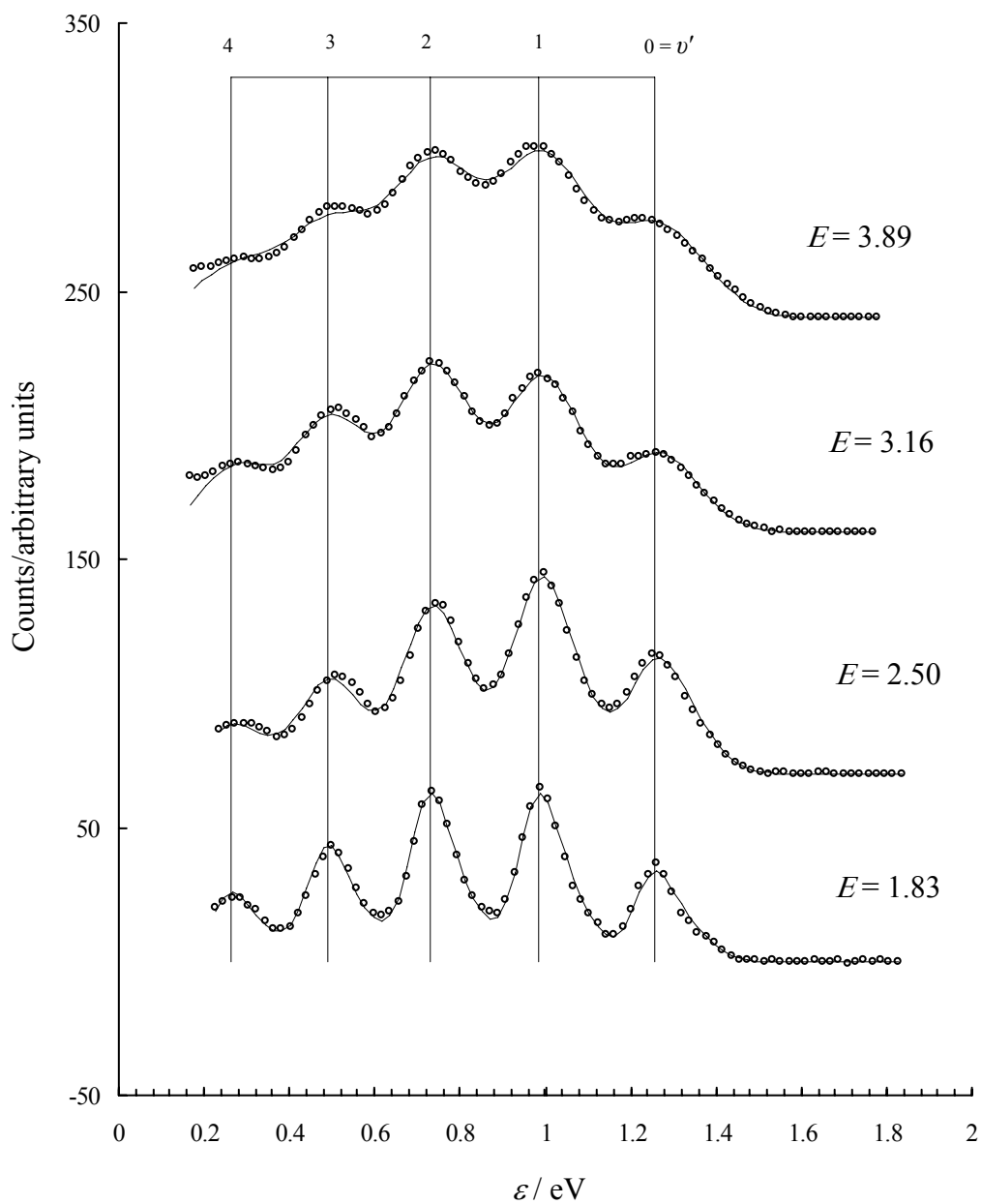
Figure 4.1: Ne* + H_2(40 °C) for Ne* at $T = 40$, 170, 300, and 450 °C. The pitchfork shows the position of the $^3P_2$ vibrational progression, adjusted for anharmonicity. The data have been normalized to equal intensity with respect to the $v' = 2$ peak for each E(kcal/mol), and the baselines have been shifted for display. The circles are the transmission corrected data, and the solid line is the best fit of the transmission corrected data.

Figure 4.2: Ne* + H_2(40 °C) for Ne* at T = 40, 170, 300, and 450 °C. The pitchfork shows the position of the $^3P_0$ vibrational progression, adjusted for anharmonicity. The data have been normalized to equal intensity with respect to the v' = 2 peak for each E(kcal/mol), and the baselines have been shifted for display. The circles are the transmission corrected data, and the solid line is the best fit of the transmission corrected data.

Figure 4.3: Collision energy dependence of the line shift for Ne* + H$_2$. The circles are our data, and the square is estimated from Reference 59.

Table 4.1: Nascent H_2^+ populations (P) and FCfs for Ne*(3 $^3P_2$) + H_2

v' X state	$P(v')/P$(1 or 2)				$P(v')/P(1)$ average of runs 2 and 4	$P(v')/P(2)$ average of runs 1 and 3	Franck-Condon factors
	E = 1.83 kcal/mol	E = 2.50 kcal/mol	E = 3.16 kcal/mol	E = 3.89 kcal/mol			
0	0.5390 ± 0.0022	0.5898 ± 0.0015	0.4751 ± 0.0014	0.5725 ± 0.0011	0.5812 ± 0.0122	0.5071 ± 0.0452	0.523
1	0.9987 ± 0.0038	1	0.9371 ± 0.0026	1	1	0.9679 ± 0.0436	0.920
2	1	0.8521 ± 0.0023	1	0.9584 ± 0.0019	0.9053 ± 0.0752	1	1
3	0.6890 ± 0.0035	0.4765 ± 0.0019	0.6880 ± 0.0024	0.5904 ± 0.0015	0.5335 ± 0.0805	0.6885 ± 0.0007	0.877
4	0.4114 ± 0.0040	0.2514 ± 0.0022	0.4056 ± 0.0023	0.3294 ± 0.0014	0.2904 ± 0.0552	0.4085 ± 0.0041	0.686

Table 4.2: Population (P) comparison and FCfs for Ne*(3 $^3P_2$) + H_2

v' X state	$P(v')/P(2)$ average of runs 1 and 3	$P(v')/P(2)$ Ref. 59	Franck-Condon factors
0	0.5071 ± 0.0452	0.56 ± 0.03	0.523
1	0.9679 ± 0.0436	0.96 ± 0.03	0.920
2	1	1	1
3	0.6885 ± 0.0007	0.77 ± 0.06	0.877
4	0.4085 ± 0.0041	0.52 ± 0.01	0.686
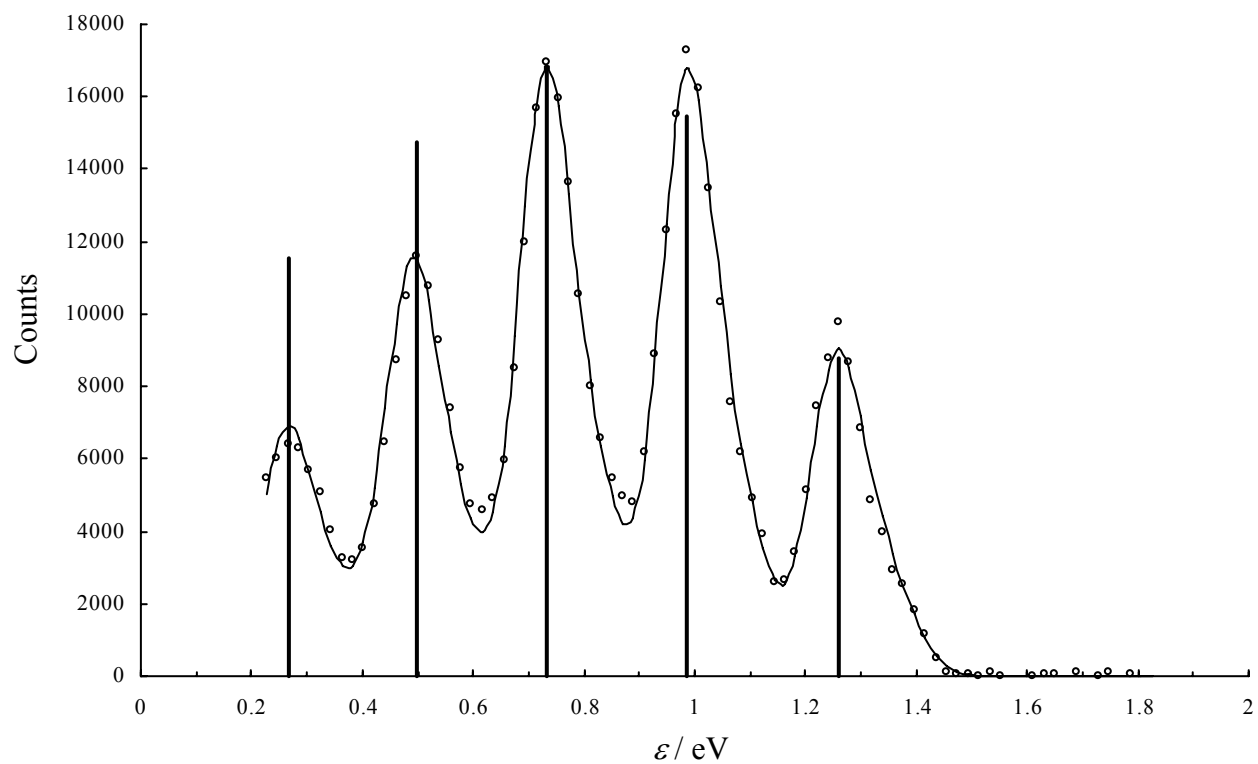
Figure 4.4: Relative FCfs for Ne*(40 °C) + H$_2$(40 °C). The FCfs appear as thick black lines, positioned arbitrarily at the peak maximum.

4.2 CARBON MONOXIDE

Figure 3.6 in Section 3.1 shows the final fits of all four Es for Ne* + CO, along with the $^3P_2$ pitchfork progression. Figure 4.5 shows the final fits of all four Es for Ne* + CO, along with the $^3P_0$ pitchfork progression. For E = 1.78, 2.24, 2.81, and 3.39 kcal/mol, $\Delta\varepsilon_s$ = 56 ± 2, 61 ± 1, 69 ± 3, and 72 ± 1 meV, respectively. (See Chapter 5 for a brief discussion of the value for E = 2.81 kcal/mol.) These results are shown graphically in Figure 4.6. Lescop *et al*. [13] reported *no line shift* for Ne* + CO for $E \approx$ 1.3 kcal/mol. If we extrapolate Figure 4.6, we can estimate $\Delta\varepsilon_s \approx$ 51 meV at $E \approx$ 1.3 kcal/mol. The finding of Lescop *et al*. is rather amazing, drastically different from our results. No reliable estimate can be made from the only plot of their data in their paper to counter the claim they make in the text of their paper. The relative vibrational populations (relative peak areas) and relative FCfs for Ne*(3 $^3P_2$) + CO are shown in Table 4.3. Although slightly larger, our population ratios are similar to those of Reference 13. The plot of normalized FCfs along with the normalized data already presented in Figure 3.6 is shown in Figure 4.7. The FCfs fall off very quickly; only two FCf lines are visible at the scale used. FC behavior is exhibited, at most, in only the first two peaks of the Ne* + CO spectra. Note that, unlike H$_2$, CO has two accessible states, the X and A states. This is important because population data makes the most sense when reported relative to the other peaks within the same state or progression. Also, relative FCfs are calculated *within* each state. While FCfs were calculated for the X and A state of CO$^+$, the unreliability of our data below 0.2 eV clouds the interpretation of FCfs in the region where the A state is accessible. The calculated A state FCfs peak at v' = 2. With only one

61

A state peak, however, we can not state relative populations. Thus, Table 4.3 contains only the *X*

state populations and FCfs.
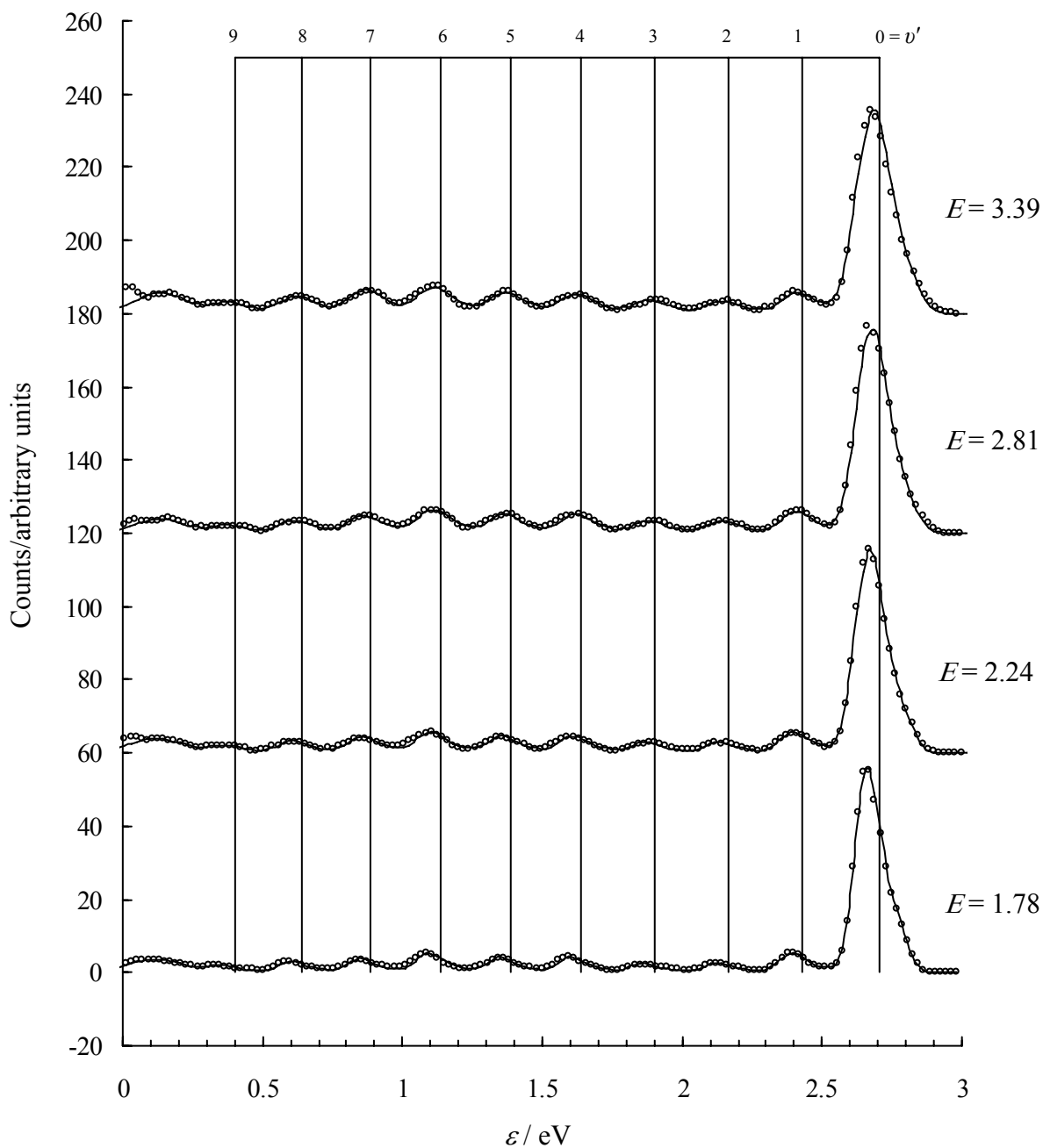
Figure 4.5: Ne* + CO(40 °C) for Ne* at $T = 40, 200, 400$, and 600 °C. The pitchfork shows the position of the $^{3}P_{0}$ vibrational progression, adjusted for anharmonicity. The data have been normalized to equal intensity for each E(kcal/mol), and the baselines have been shifted for display. The circles are the transmission corrected data, and the solid line is the best fit of the transmission corrected data.
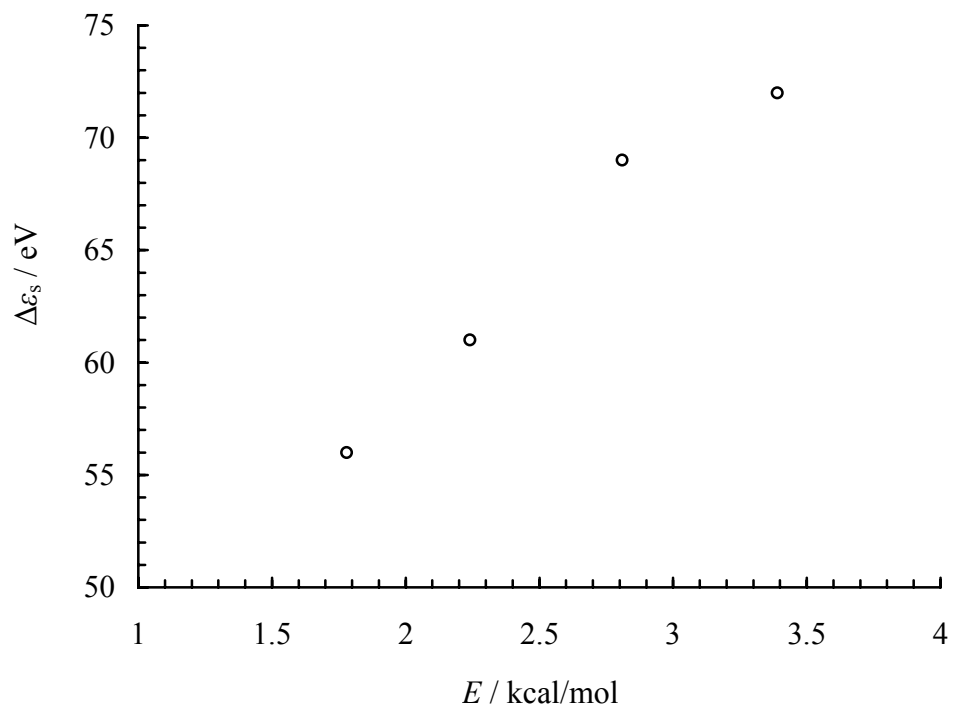
Figure 4.6: Collision energy dependence of the PIES shift for Ne* + CO.

Table 4.3: Nascent CO^+ populations (P) and FCfs for $Ne^*(3\ ^3P_2)$ + CO

v' X state	$P(v')/P(0)$				$P(v')/P(0)$ average	$P(v')/P(0)$ Ref. 13	Franck-Condon factors
	$E = 1.78$ kcal/mol	$E = 2.24$ kcal/mol	$E = 2.81$ kcal/mol	$E = 3.39$ kcal/mol			
0	1	1	1	1	1	1	1
1	0.0964 ± 0.0003	0.1016 ± 0.0005	0.1064 ± 0.0004	0.1041 ± 0.0005	0.1021 ± 0.0043	0.069	0.038
2	0.0483 ± 0.0003	0.0534 ± 0.0004	0.0605 ± 0.0004	0.0618 ± 0.0004	0.0560 ± 0.0063	0.033	0.0001
3	0.0462 ± 0.0003	0.0554 ± 0.0005	0.0611 ± 0.0004	0.0661 ± 0.0004	0.0572 ± 0.0085	0.025	—
4	0.0765 ± 0.0004	0.0809 ± 0.0006	0.0921 ± 0.0005	0.0932 ± 0.0006	0.0857 ± 0.0083	0.035	—
5	0.0765 ± 0.0005	0.0840 ± 0.0007	0.0970 ± 0.0006	0.1037 ± 0.0007	0.0903 ± 0.0123	0.037	—
6	0.0942 ± 0.0006	0.1009 ± 0.0009	0.1133 ± 0.0008	0.1279 ± 0.0010	0.1091 ± 0.0148	0.047	—
7	0.0682 ± 0.0007	0.0797 ± 0.0009	0.0885 ± 0.0008	0.1157 ± 0.0010	0.0880 ± 0.0202	0.039	—
8	0.0538 ± 0.0008	0.0604 ± 0.0011	0.0638 ± 0.0010	0.0875 ± 0.0012	0.0664 ± 0.0147	0.035	—
9	0.0328 ± 0.0017	0.0356 ± 0.0019	0.0390 ± 0.0016	0.0526 ± 0.0019	0.0400 ± 0.0088	—	—
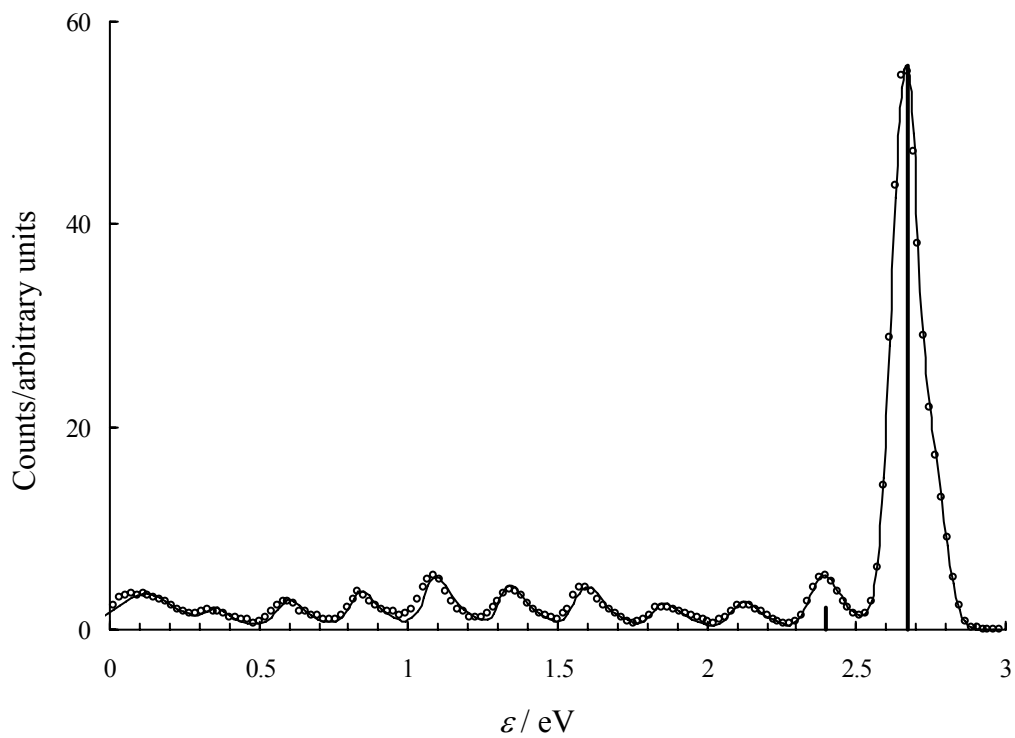
Figure 4.7: Relative FCfs for Ne*(40 °C) + CO(40 °C). The FCfs appear as thick black lines, positioned arbitrarily at the peak maximum. Only two FCfs are visible at this scale.

4.3 NITROGEN

The final fits of all four Es for Ne* + N_2 are shown in Figures 4.8 and 4.9. For E = 1.77, 2.23, 2.80, and 3.38 kcal/mol, $\Delta\varepsilon_s$ = 37 ± 1, 45 ± 1, 62 ± 1, and 67 ± 1 meV, respectively. These results are shown graphically in Figure 4.10, which contains a point (the square in the plot) that is from Lescop *et al*. [12] who reported a shift of 60 ± 5 and 65 ± 5 meV for the J = 2 and J = 0 states, respectively, for E ≈ 1.2 kcal/mol. (Recall that we can not determine a difference in the shift for the two J states, so we plot an average shift value of 63 kcal/mol in Figure 4.10.) This is larger than the value we obtained even at E = 2.23 kcal/mol. Note that Figure 4.10 also contains the three line shifts that we obtained from the seeded beam as well. See Section 4.5. The relative vibrational populations (relative peak areas) and FCfs for Ne*(3 $^3P_2$) + N_2(40 °C) are shown in Table 4.4. The population ratios in Table 4.4 from Reference 12 are for Ne*($^3P_2$). Their values for Ne*($^3P_0$) are slightly higher than our population ratios.

Again, using Tables 1.1 and 1.3, the first peak in the Ne* + N_2 spectrum should appear at ε = (16.6191 − 15.5808) eV = 1.0383 eV. If anharmonicity is neglected, additional peak positions in the $^3P_2$ progression are at 0.7647, 0.4910 eV, …, given that the vibrational levels are separated by v = 2207.00 cm^{-1} = 0.273633 eV. Again, the slight shoulder on the right of the largest peak is assigned to ionization due to Ne*($2p^5 3s\ ^3P_0$). Thus, the first peak in the $^3P_0$ progression should appear at ε = (16.7154 − 15.5808) eV = 1.1346 eV, and the additional, *harmonic* peaks in the progression appear at 0.8610, 0.5873 eV, … and so on. The peaks are

best assigned to the $X\,^2\Sigma_g^+$ state $\upsilon = 0 \rightarrow 4$ progression. The fair, at best, fit of the $\upsilon = 4$ peak can be attributed mostly to our inability to accurately perform a transmission correction on very low kinetic energy electrons. It should be noted also that the A state *is* energetically accessible (but by only 0.017 eV) with the $^3P_0$ state of Ne*. Since only 28% of the excited beam is Ne*($^3P_0$), the signal is expected to be small, however, for this transition. Attempts to fit the peaks with an $X\,^2\Sigma_g^+$ $\upsilon = 0 \rightarrow 4$ progression and an $A\,^2\Pi_u$ $\upsilon = 0 \rightarrow 0$ progression did not produce reliable improvement. In Figures 4.8 and 4.9 the expected peak broadening with increasing E is seen more readily than in the case for CO. Figure 4.11 contains a plot of the FCfs for the run of Ne*(40 °C) + N_2(40 °C). As in the case of CO, the FCfs die off quickly, indicating that Frank-Condon behavior is not observed in the case of N_2.
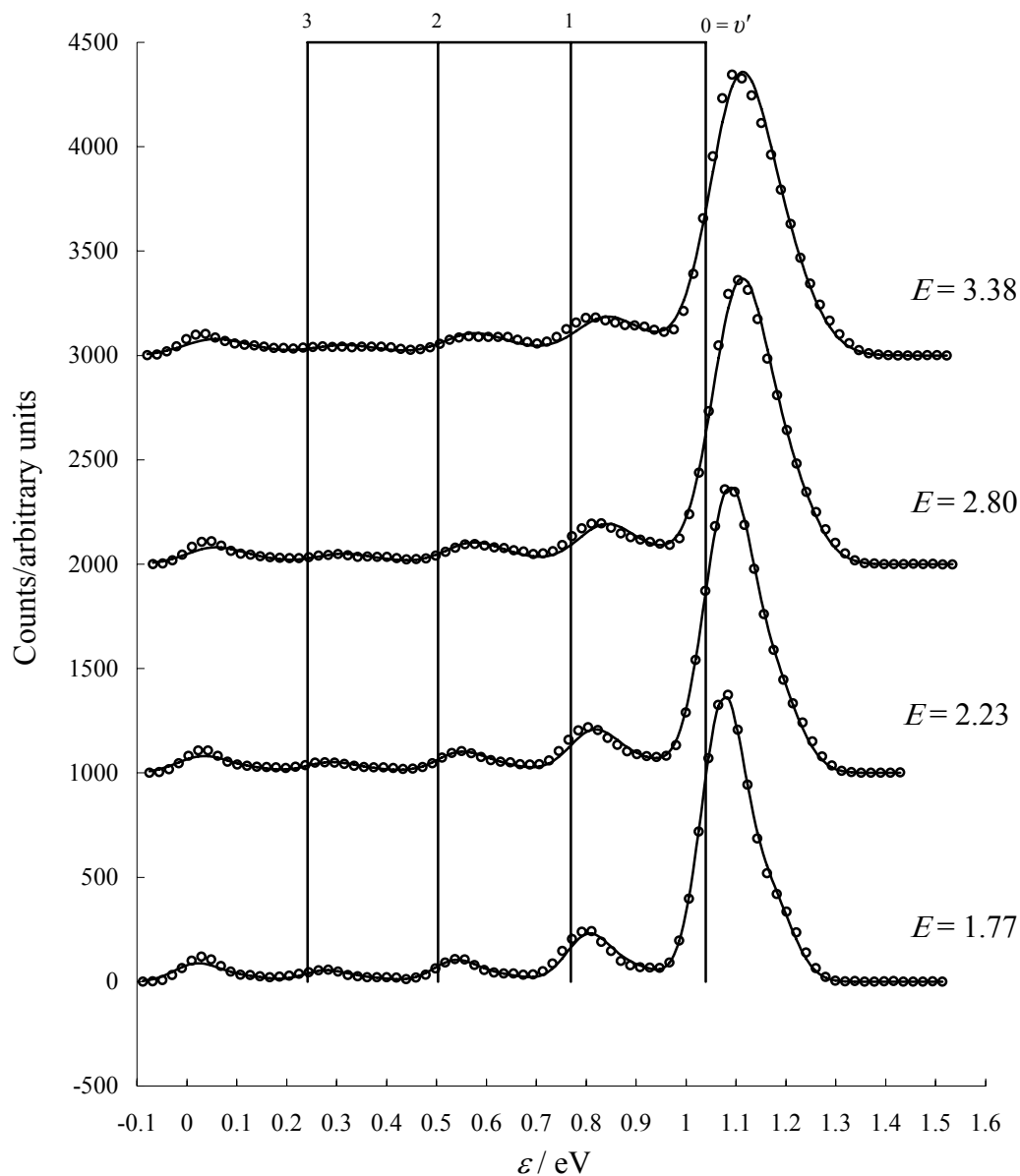
Figure 4.8: Ne* + N_2(40 °C) for Ne* at $T = 40, 200, 400$, and 600 °C. The pitchfork shows the position of the $^3P_2$ vibrational progression, adjusted for anharmonicity. (The v' = 4 state is not accessible.) The data have been normalized to equal intensity for each E(kcal/mol), and the baselines have been shifted for display. The circles are the transmission corrected data, and the solid line is the best fit of the transmission corrected data.
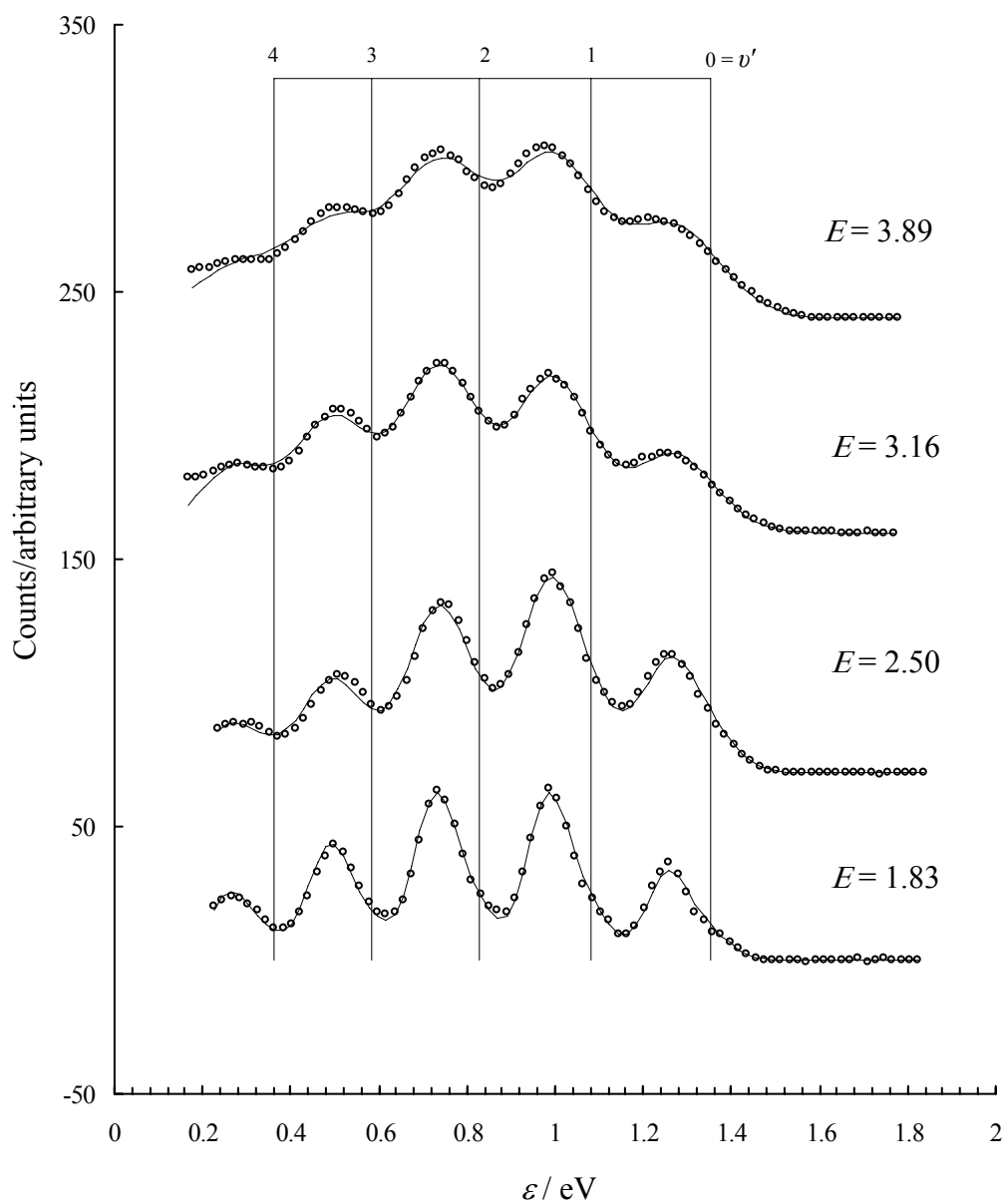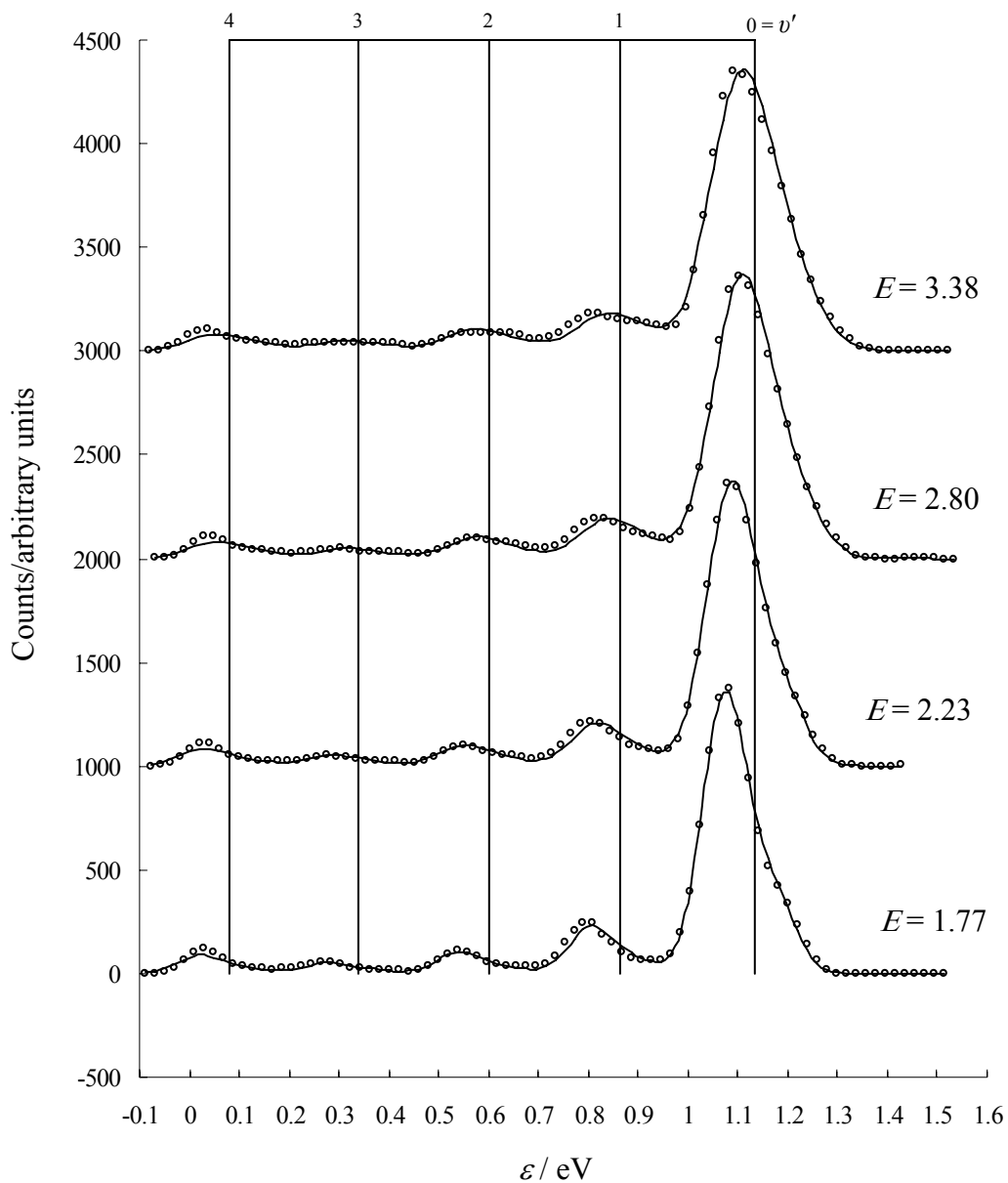
Figure 4.9: Ne* + N_2(40 °C) for Ne* at $T = 40, 200, 400$, and 600 °C. The pitchfork shows the position of the $^3P_0$ vibrational progression, adjusted for anharmonicity. The data have been normalized to equal intensity for each E(kcal/mol), and the baselines have been shifted for display. The circles are the transmission corrected data, and the solid line is the best fit of the transmission corrected data.
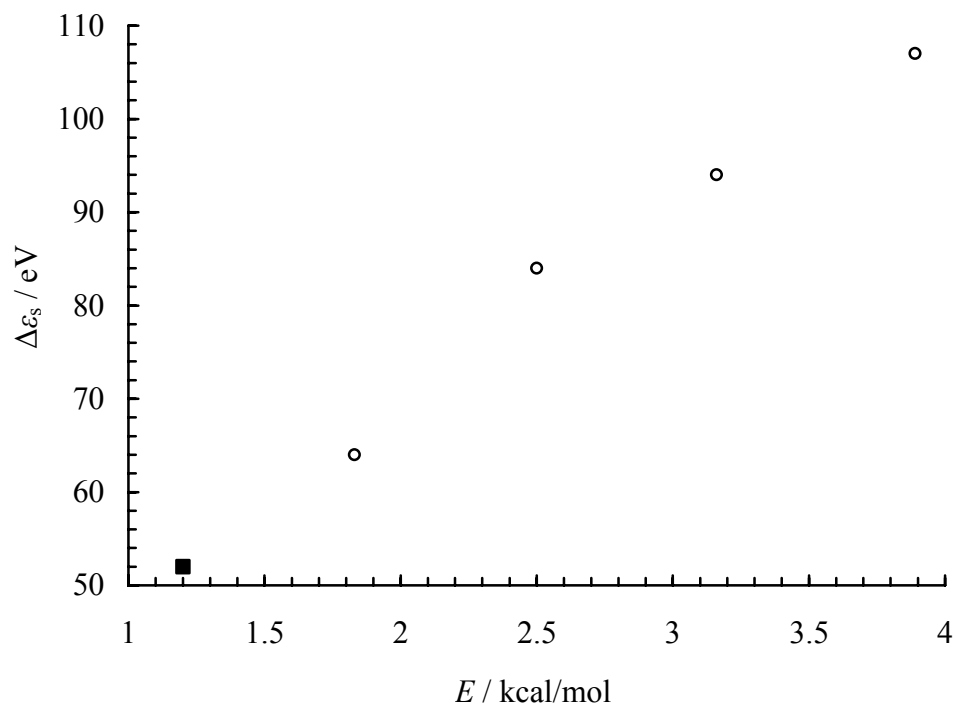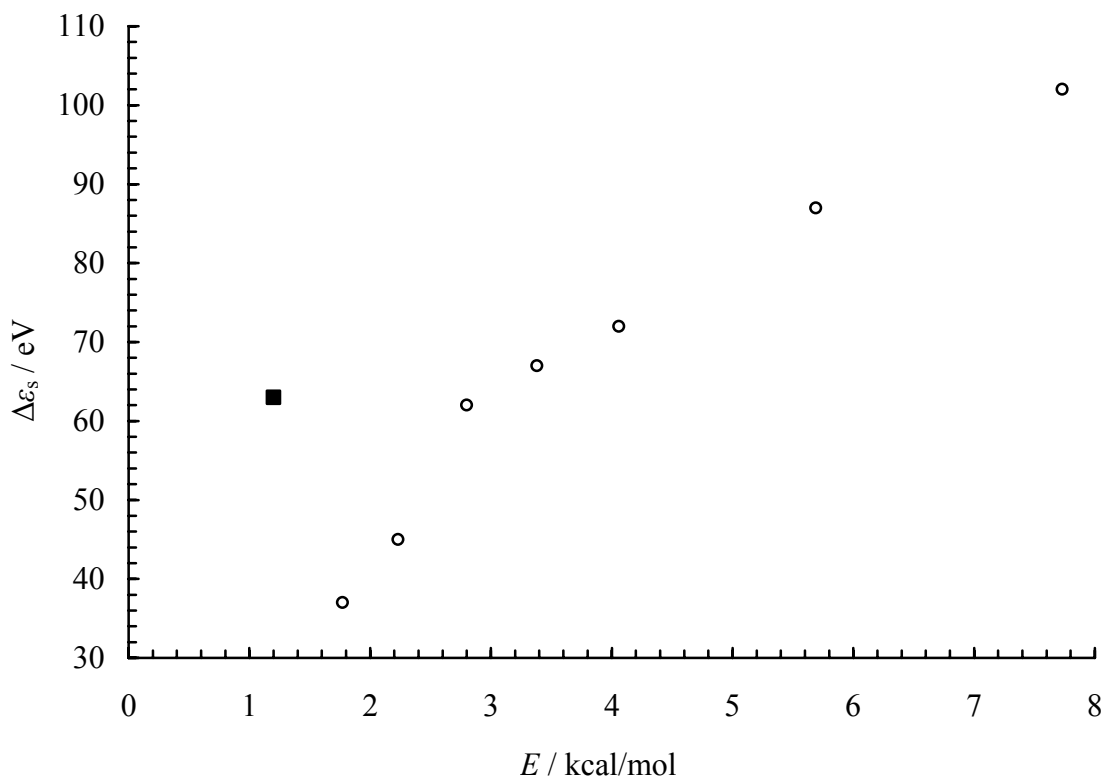
Figure 4.10. Collision energy dependence of the PIES shift for Ne* + N_2. The circles are our data, and the square is averaged from the two J state values reported in Reference 12.

Table 4.4: Nascent N_2^+ populations (P) and FCfs for Ne*($3\,^3P_2$) + N_2

| v' X state	$P(v')/P(0)$				$P(v')/P(0)$ average	$P(v')/P(0)$ Ref. 12	Franck-Condon factors
	$E = 1.77$ kcal/mol	$E = 2.23$ kcal/mol	$E = 2.80$ kcal/mol	$E = 3.38$ kcal/mol			
0	1	1	1	1	1	1	1
1	0.1691 ± 0.0006	0.1523 ± 0.0004	0.1409 ± 0.0004	0.1367 ± 0.0004	0.1498 ± 0.0145	0.20 ± 0.02	0.085
2	0.0767 ± 0.0005	0.0752 ± 0.0003	0.0761 ± 0.0004	0.0780 ± 0.0004	0.0765 ± 0.0012	0.12 ± 0.02	0.005
3	0.0404 ± 0.0008	0.0381 ± 0.0005	0.0362 ± 0.0006	0.0368 ± 0.0006	0.0379 ± 0.0019	0.08 ± 0.02	0.0003
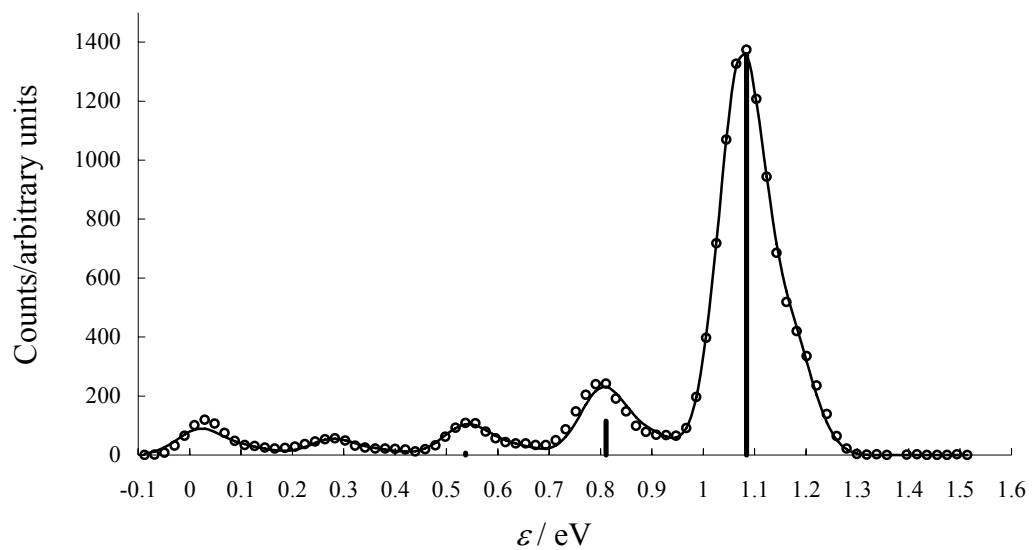
Figure 4.11: Normalized FCf's for Ne*(40 °C) + N$_2$(40 °C). The FCf's appear as thick black lines, positioned arbitrarily at the peak maximum. Only three FCf's are visible at this scale, including the very small line at 0.54 eV.

4.4 NITROGEN MONOXIDE

The final fits for both Es for Ne* + NO are shown in Figures 4.12 and 4.13. For $E = 1.76$ and

2.10 kcal/mol, $\Delta\varepsilon_s = 17 \pm 3$ and 7 ± 3 meV, respectively, for the X state. For the a state, $\Delta\varepsilon_s = 64$

± 1 and 53 ± 1 meV, respectively, for $E = 1.76$ and 2.10 kcal/mol. These results are shown

graphically in Figure 4.14. The relative vibrational populations (relative peak areas) and FCfs

for Ne*$(3\,^3P_2)$ + NO(40 °C) are shown in Tables 4.5 and 4.6.

Again, using Tables 1.1 and 1.3, the first peak in the Ne* + NO spectrum should appear

at $\varepsilon = (16.6191 - 9.264)$ eV $= 7.355$ eV. If anharmonicity is neglected, additional peak positions

in the $^3P_2$ progression are at 7.060, 6.766 eV, …, given that the vibrational levels are separated

by $v = 2376.721$ cm^{-1} $= 0.29468$ eV. Again, the slight shoulder on the right of the largest peak is

assigned to ionization due to Ne*$(2p^53s\,^3P_0)$. Thus, the first peak in the $^3P_0$ progression should

appear at $\varepsilon = (16.7154 - 9.264)$ eV $= 7.451$ eV, and the additional, *harmonic* peaks in the

progression appear at 7.156, 6.862 eV, … and so on. The progression of the $X\,^1\Sigma^+$ state $v = 0 \rightarrow$

25 in Figures 4.12 and 4.13 is a very remarkable progression that ends, we suggest, with the

appearance of three peaks, present at both Es, from hot band transitions. The spacing of these

suspected hot bands simply do not allow them to be part of the X or a state progressions. The

next set of peaks that we can assign is due to the a state. The first peak in the Ne*$(^3P_2)$ $a\,^3\Sigma^+$

state progression should appear at $\varepsilon = (16.6191 - 15.663)$ eV $= 0.956$ eV. If anharmonicity is

neglected, additional peak positions in this progression are at 0.794, 0.633 eV, …, given that the

vibrational levels are separated by $v = 1303.07$ cm^{-1} = 0.16156 eV. The spacing in the a state progression is as expected for the $v = 0, 1, 2,$ and 3 peaks, but between the $v = 3$ and the $v = 4$ peak there is a sudden decrease in spacing, suggesting that underlying peaks are not identified properly or the low ε region is again unreliable. No simple explanation exists for this. As is the case for CO and N$_2$, there is an energetically accessible state very near the region of zero kinetic energy. Here it is the $b\ ^3\Pi$ state ($v = 0 \rightarrow 0$) for which Ne*($^3P_2$) should produce electrons with ε = (16.6191 − 16.560) eV = 0.0591 eV. Ne*($^3P_0$) should produce electrons with ε = (16.7156 − 16.560) eV = 0.1556 eV. As usual the data in this region are suspect, and no attempt was made to fit the lone b state peak.
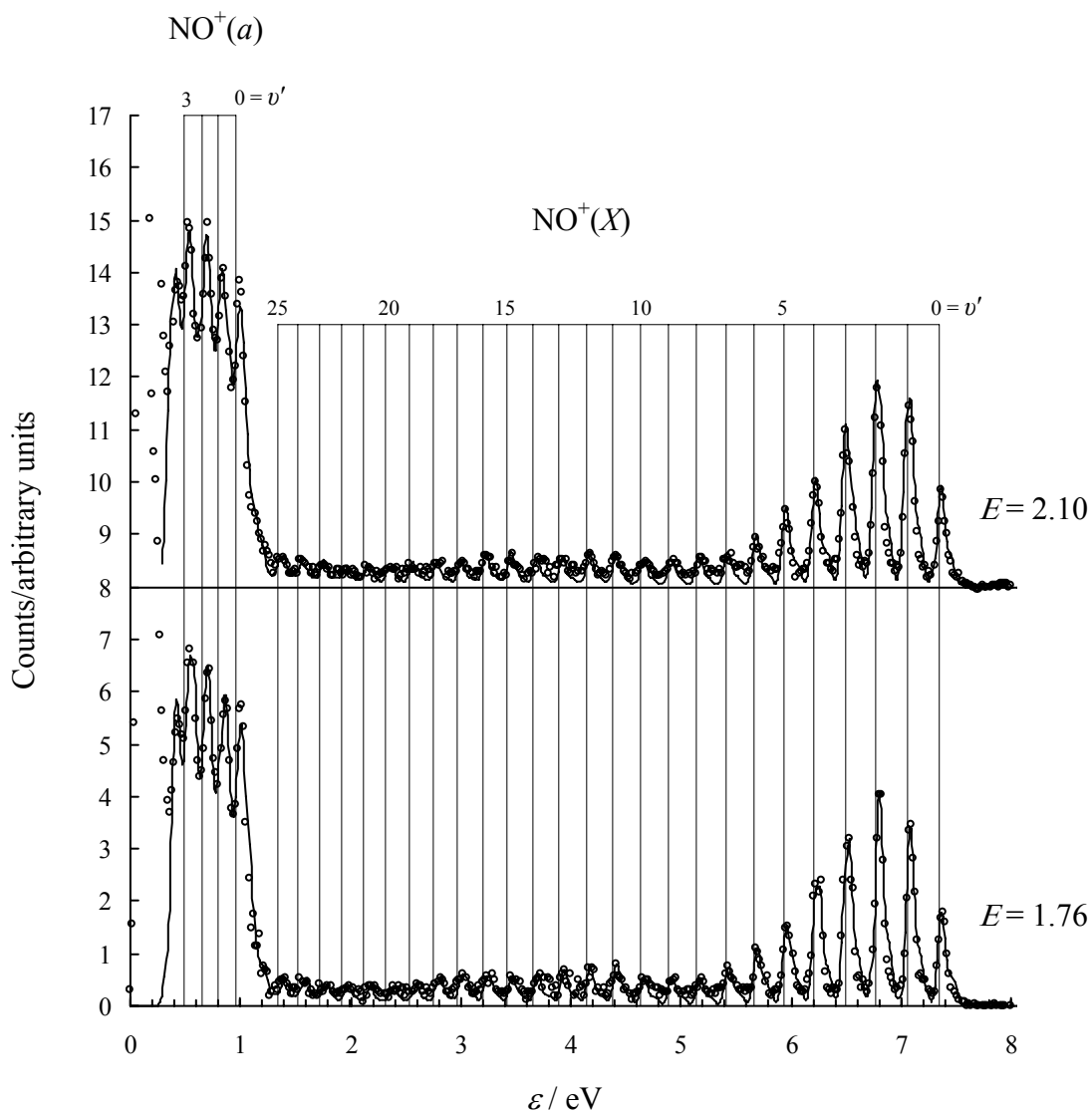
Figure 4.12: Ne* + NO(40 °C) for Ne* at $T = 40$ and 150 °C. The pitchfork shows the position of the $^3P_2$ vibrational progression, adjusted for anharmonicity. The data have been normalized to equal intensity for each E(kcal/mol), and the baselines have been shifted for display. The circles are the transmission corrected data, and the solid line is the best fit of the transmission corrected data.
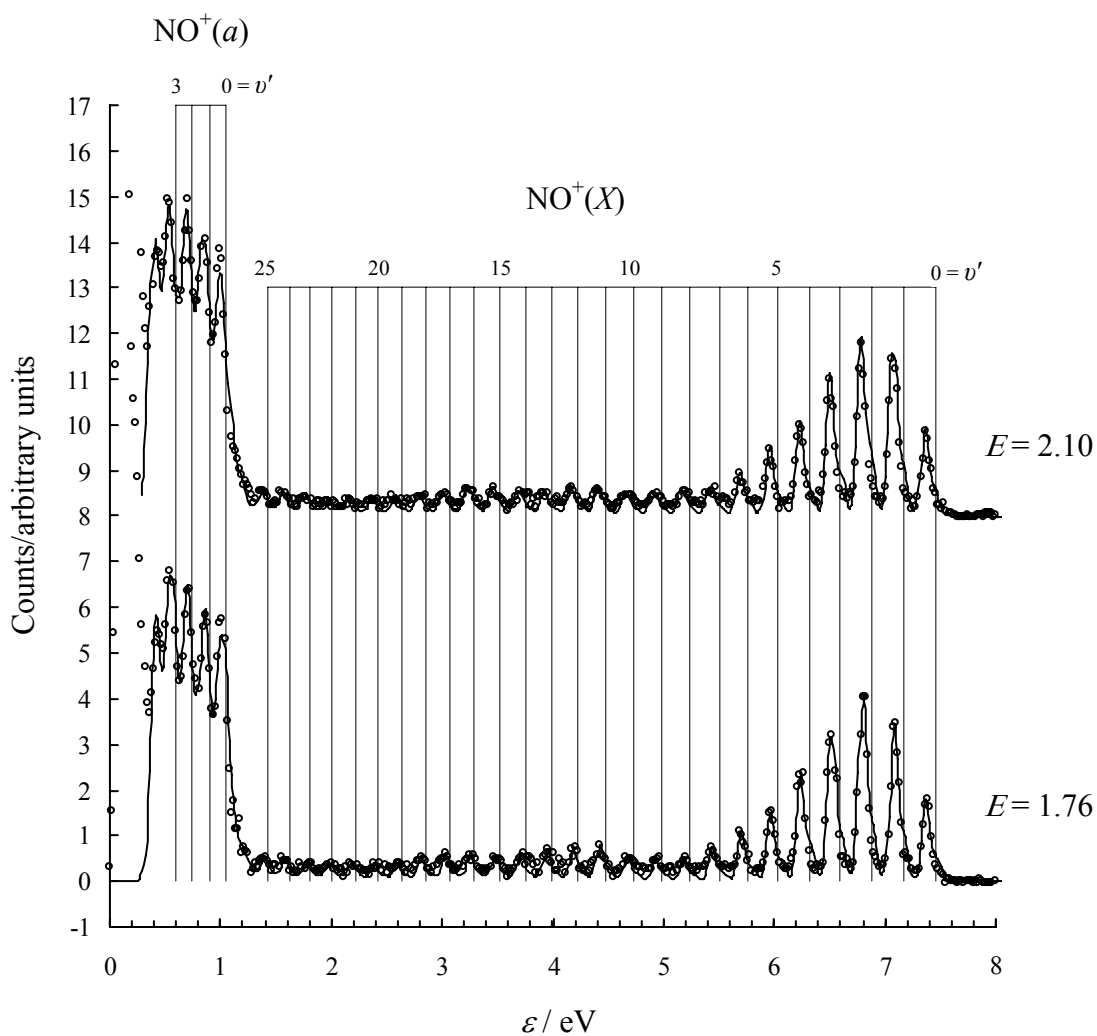
Figure 4.13: Ne* + NO(40 °C) for Ne* at $T = 40$ and 150 °C. The pitchfork shows the position of the $^3P_0$ vibrational progression, adjusted for anharmonicity. The data have been normalized to equal intensity for each E(kcal/mol), and the baselines have been shifted for display. The circles are the transmission corrected data, and the solid line is the best fit of the transmission corrected data.
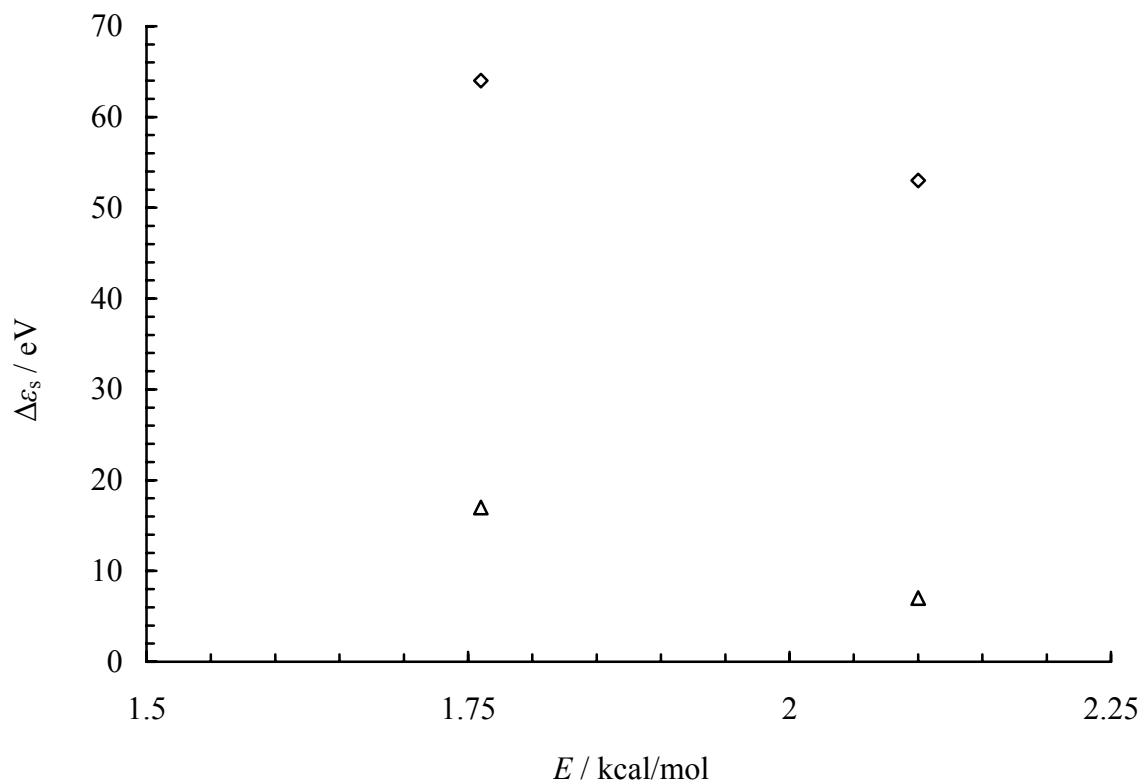
Figure 4.14: Collision energy dependence of the PIES shift for Ne* + NO. The triangles (*X* state) and diamonds (*a* state) are for *E* = 1.76 and 2.10 kcal/mol, respectively.

A close up of the *X* state of Ne* + NO(40 °C) for Ne* at $T = 40$ and 150 °C is shown in
Figure 4.15. Note the decreasing blue shift with increasing energy. This is atypical.
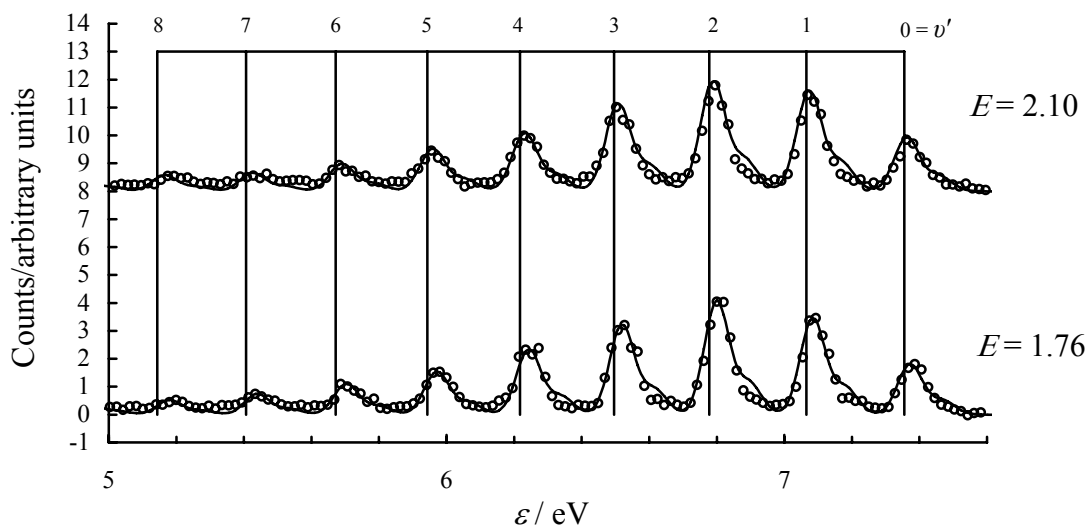
Figure 4.15: Close up of a portion of the *X* state progression for Ne* + NO(40 °C) for
Ne* at $T = 40$ and 150 °C. The progression is for the $^3P_2$ vibrational progression,
adjusted for anharmonicity.

A close up of the *a* state of Ne* + NO(40 °C) for Ne* at $T = 40$ and 150 °C is shown in Figure 32. The large blue shift is readily observed.
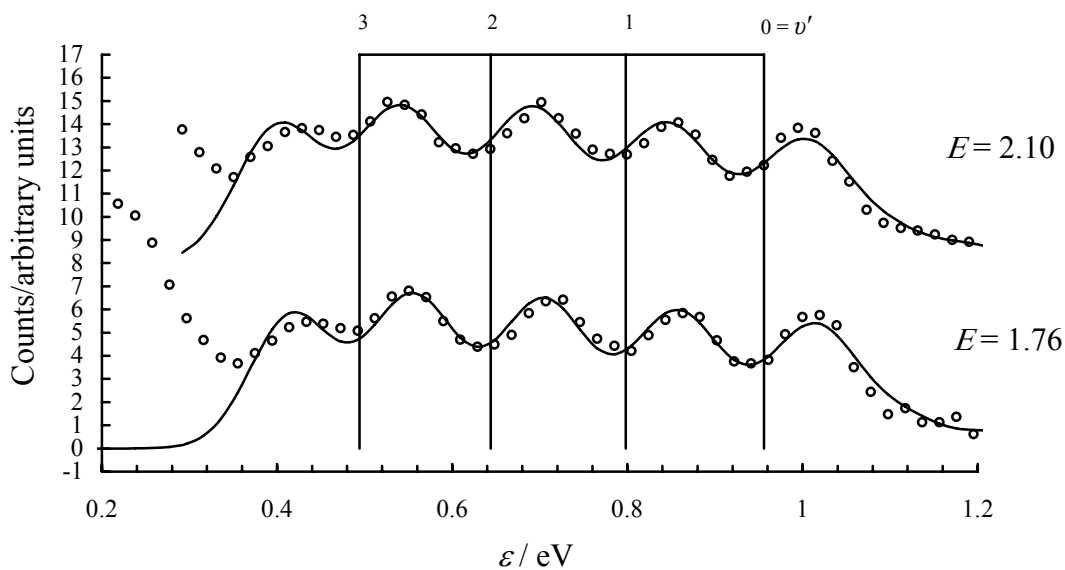
Figure 4.16: Close up of a portion of the *a* state progression for Ne* + NO(40 °C) for Ne* at $T = 40$ and 150 °C. The progression is for the $^3P_2$ vibrational progression, adjusted for anharmonicity.

When compiling the relative population results for NO, we must distinguish between the X state and the a state in order to compare the results to FCfs. Table 4.5 contains population and FCf information on Ne*(3 $^3P_2$) + NO(40 °C) for the X state only. Table 4.6 is for the a state only. In Table 4.5 the relative populations are calculated from the fixed values used in the final fit. The errors in Table 4.5 for the first seven peaks are from a fit where their heights were not held constant. As described in Chapter 3.1, however, these peak heights had to be held constant to get a reasonable final fit. For the $v' = 7$ to 25 peaks, the errors are from the X state fit in which the first seven peak heights were held constant. Thus, all of the errors in Table 4.5 should be regarded as an estimate only. Obtaining errors for the X state peaks from the final fit of the a state is not possible; *no X state peak heights were varied in the final fit.* The FCfs are not significant beyond $v' = 7$ for the X state.

The populations reported in Table 4.6 are from the final fit in the usual manner since we varied the peak heights as usual − with one exception. The $v' = 4$ peak was not reported since the values were from the region of the spectrum where the data can't be trusted. All a state populations were taken relative to $v' = 3$. The results in Tables 4.5 and 4.6 indicate that FC behavior is not observed for NO. For the X state, the PIES spectrum and the FCfs do not even peak at the same vibrational level. For the a state the ratios of the peak heights are quite different. Figure 4.17 contains the relative FCfs for the X state of Ne*(3 $^3P_2$) + NO(40 °C) at $T = $ 40 °C. Only the region where significant FCfs exist is shown. Figure 4.18 contains the relative FCfs for the a state of Ne*(3 $^3P_2$) + NO(40 °C) at $T = 40$ °C. Only the first four peaks in the progression are shown since we can not trust the data at low kinetic energy.

Table 4.5. Nascent X state NO^+ populations (P) and FCfs for Ne*(3 $^3P_2$) + NO

| v' | $P(v')/P(0)$ | | $P(v')/P(0)$ | FCfs | v' | $P(v')/P(0)$ | | $P(v')/P(0)$ |
	$E = 1.76$ kcal/mol	$E = 2.10$ kcal/mol	average			$E = 1.76$ kcal/mol	$E = 2.10$ kcal/mol	average
0	0.4454 ± 0.0011	0.4870 ± 0.0011	0.4662 ± 0.0294	0.492	13	0.1724 ± 0.0012	0.1367 ± 0.0011	0.1546 ± 0.0252
1	0.8530 ± 0.0019	0.9112 ± 0.0018	0.8821 ± 0.0412	1	14	0.1509 ± 0.0010	0.1426 ± 0.0009	0.1468 ± 0.0059
2	1	1	1	0.892	15	0.1369 ± 0.0009	0.1665 ± 0.0008	0.1517 ± 0.0209
3	0.7922 ± 0.0018	0.7938 ± 0.0017	0.7930 ± 0.0011	0.459	16	0.1458 ± 0.0010	0.1583 ± 0.0009	0.1521 ± 0.0088
4	0.5731 ± 0.0015	0.5242 ± 0.0014	0.5487 ± 0.0346	0.151	17	0.1524 ± 0.0010	0.1289 ± 0.0009	0.1407 ± 0.0166
5	0.3790 ± 0.0012	0.3837 ± 0.0011	0.3814 ± 0.0033	0.033	18	0.1339 ± 0.0010	0.1140 ± 0.0009	0.1240 ± 0.0141
6	0.2700 ± 0.0010	0.2471 ± 0.0009	0.2586 ± 0.0162	0.005	19	0.1015 ± 0.0010	0.1168 ± 0.0010	0.1092 ± 0.0108
7	0.1840 ± 0.0007	0.1657 ± 0.0006	0.1749 ± 0.0128	0.0004	20	0.0971 ± 0.0012	0.0978 ± 0.0011	0.0975 ± 0.0005
8	0.1297 ± 0.0006	0.1450 ± 0.0006	0.1374 ± 0.0108	—	21	0.0921 ± 0.0014	0.1011 ± 0.0013	0.0966 ± 0.0064
9	0.1287 ± 0.0006	0.1385 ± 0.0006	0.1336 ± 0.0069	—	22	0.0966 ± 0.0017	0.1073 ± 0.0015	0.1020 ± 0.0076
10	0.1339 ± 0.0007	0.1260 ± 0.0006	0.1300 ± 0.0056	—	23	0.0966 ± 0.0019	0.1272 ± 0.0017	0.1119 ± 0.0216
11	0.1984 ± 0.0008	0.1585 ± 0.0007	0.1785 ± 0.0282	—	24	0.1314 ± 0.0022	0.1174 ± 0.0019	0.1244 ± 0.0099
12	0.1774 ± 0.0009	0.1716 ± 0.0008	0.1745 ± 0.0041	—	25	0.1235 ± 0.0023	0.1467 ± 0.0022	0.1351 ± 0.0164

Table 4.6. Nascent a state NO^+ populations (P) and FCfs for $Ne^*(^3P_2) + NO$

v' a state	$P(v')/P(0)$ $E = 1.76$ kcal/mol	$P(v')/P(0)$ $E = 2.10$ kcal/mol	$P(v')/P(0)$ average	Franck-Condon factors
0	0.8327 ± 0.0072	0.8024 ± 0.0058	0.8176 ± 0.0214	0.270
1	0.9083 ± 0.0082	0.8961 ± 0.0068	0.9022 ± 0.0086	0.683
2	0.9816 ± 0.0088	1.0144 ± 0.0077	0.9980 ± 0.0232	0.961
3	1	1	1	1
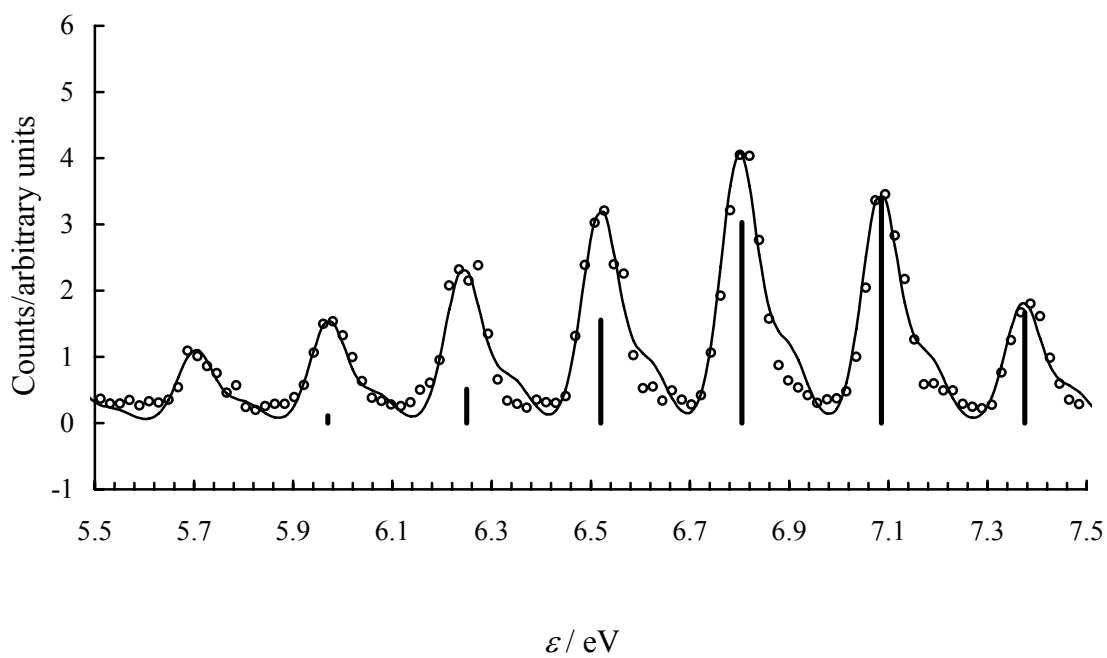
Figure 4.17: Normalized FCf's (*X* state) for Ne*(40 °C) + NO(40 °C). The FCf's appear as thick black lines, positioned arbitrarily at the peak maximum. Only significant FCfs are shown.
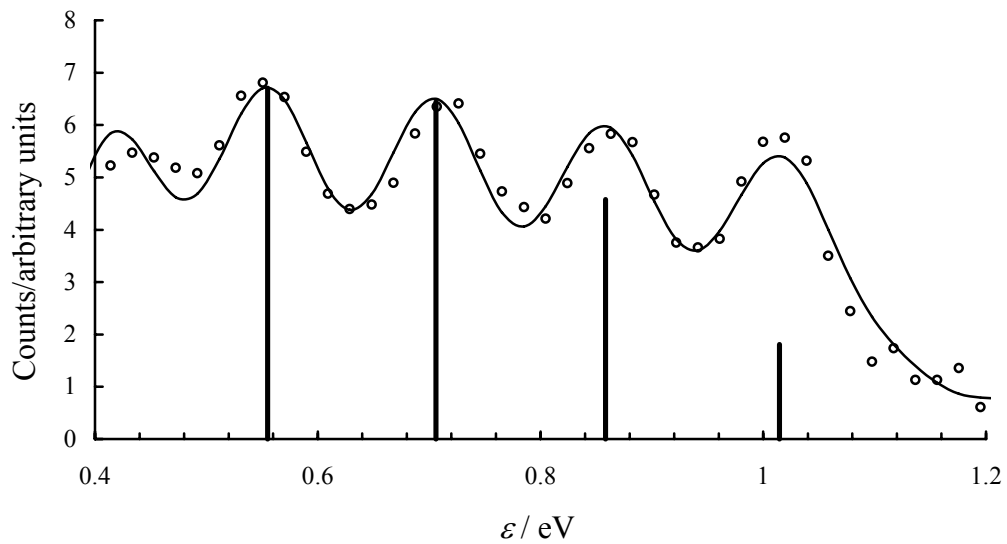
Figure 4.18: Normalized FCfs (*a* state) for Ne*(40 °C) + NO(40 °C). The FCfs appear as thick black lines, positioned arbitrarily at the peak maximum.

4.5 NITROGEN AND THE SEEDED BEAM

As described in Section 3.1 we ran the Ne* + N_2 reaction at higher Es than shown in Section 4.3 by seeding a He* beam with Ne*. (The spacing between vibrational levels for N_2 was discussed in Section 4.3.) The final fits of all three Es for Ne* (seeded beam) + N_2 are shown in Figures 4.19 and 4.20. For E = 4.06, 5.69, and 7.73 kcal/mol, $\Delta\varepsilon_s$ = 72 ± 1, 87 ± 1, and 102 ± 1, respectively. These results are shown graphically in Figure 4.10, along with the results at lower E from Section 4.3. The relative vibrational populations (relative peak areas) and FCfs for Ne*($3\,^3P_2$, seeded) + N_2(40 °C) are shown in Table 4.7.
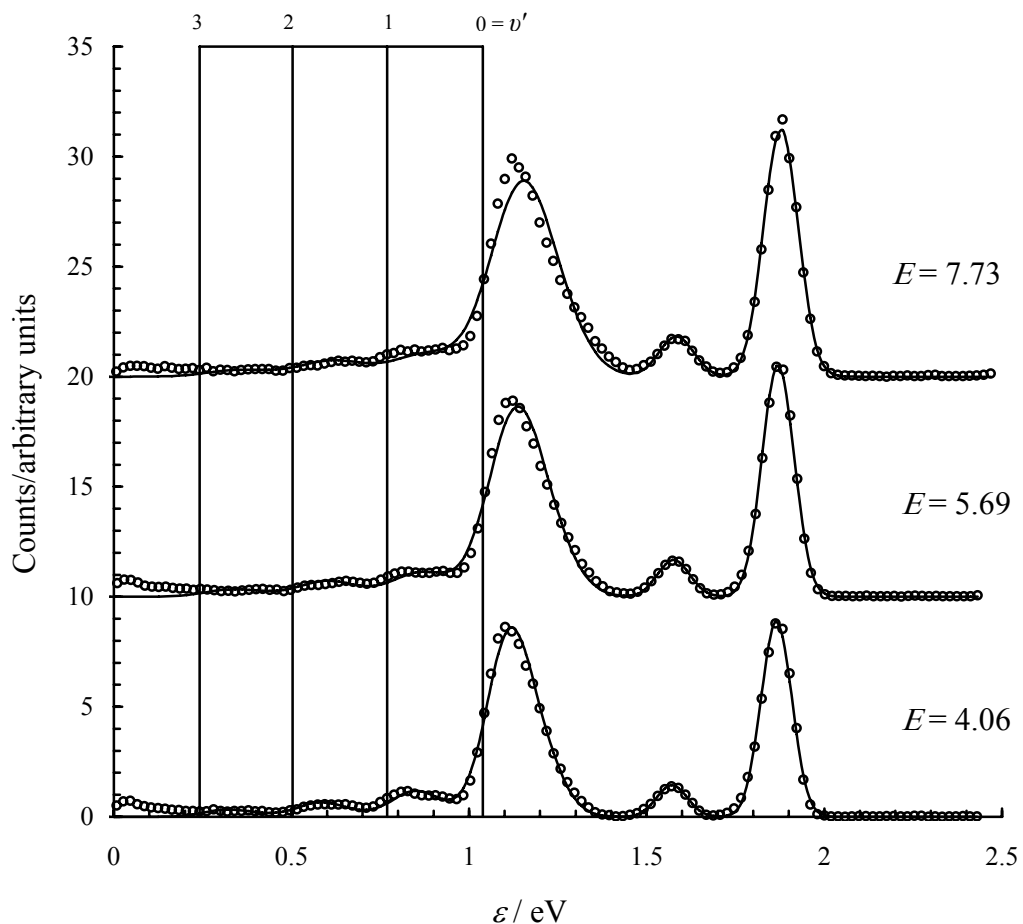
Figure 4.19: Ne*(seeded beam) + N_2(40 °C) for Ne* at T = 40, 200, and 400 °C. The pitchfork shows the position of the $^3P_2$ vibrational progression, adjusted for anharmonicity. The data have been normalized to equal intensity for each E(kcal/mol), and the baselines have been shifted for display. The circles are the transmission corrected data, and the solid line is the best fit of the transmission corrected data. Note that the first two peaks on the right are the calibration peaks from the reaction He* + N_2.
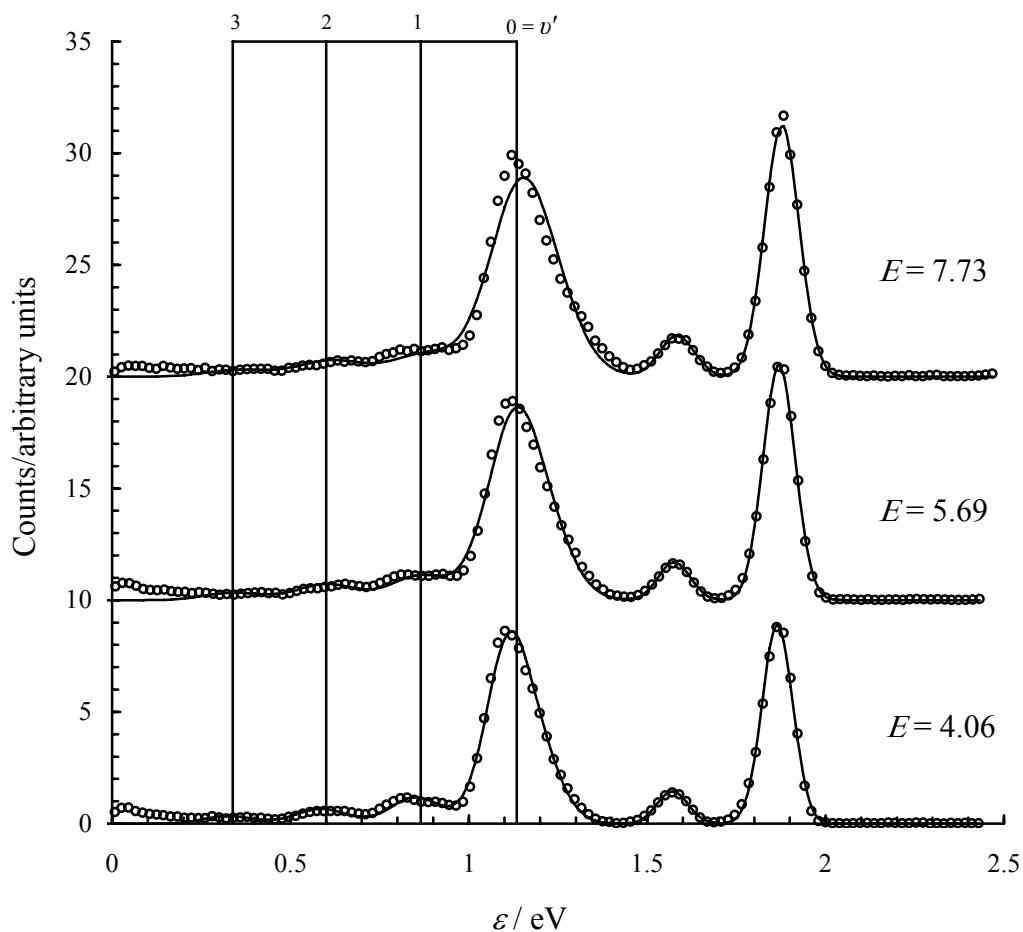
Figure 4.20: Ne*(seeded beam) + N_2(40 °C) for Ne* at $T = 40$, 200, and 400 °C. The pitchfork shows the position of the $^3P_0$ vibrational progression, adjusted for anharmonicity. The data have been normalized to equal intensity for each E(kcal/mol), and the baselines have been shifted for display. The circles are the transmission corrected data, and the solid line is the best fit of the transmission corrected data. Note that the first two peaks on the right are the calibration peaks from the reaction He* + N_2.

Table 4.7: Nascent N_2^+ populations (P) and FCfs for Ne*($3\ ^3P_2$, seeded) + N_2

v' X state	$P(v')/P(0)$			$P(v')/P(0)$ average	Franck-Condon factors
	$E = 4.06$ kcal/mol	$E = 5.69$ kcal/mol	$E = 7.73$ kcal/mol		
0	1	1	1	1	1
1	0.1368 ± 0.0008	0.1283 ± 0.0008	0.1142 ± 0. 0004	0.1264 ± 0.0114	0.085
2	0.0767 ± 0.0009	0.0833 ± 0.0008	0.0825 ± 0. 0003	0.0808 ± 0.0036	0.005
3	0.0389 ± 0.0014	0.0392 ± 0.0012	0.0347 ± 0. 0001	0.0376 ± 0.0025	—

4.6 OXYGEN

The transmission-corrected spectrum for the well-resolved portion of the Ne*(40 °C) + O_2(40 °C) X $^2\Pi_g$ state $v' = 0 \rightarrow 9$ progression is presented in Figure 4.21. For $E = 1.82$ kcal/mol, $\Delta\varepsilon_s = -6 \pm 1$ meV for the X state. As discussed in Section 3.1, the O_2 spectrum is very difficult to fit due to an underlying continuum from unknown transitions, and only the line shift value is valid with the current fit, not the populations. For the sake of reference the FCfs for O_2 are given in Table 11, and from these values it is evident that the O_2 X $^2\Pi_g$ state progression exhibits peaks well beyond that predicted from photoionization.

Tables 1.1 and 1.3 indicate that the first peak in the Ne* + O_2 spectrum should appear at $\varepsilon = (16.6191 - 12.071)$ eV $= 4.548$ eV. If anharmonicity is neglected, additional peak positions in the $^3P_2$ progression are at 4.312, 4.076 eV, …, given that the vibrational levels are separated by $\upsilon = 1903.85$ cm$^{-1} = 0.236047$ eV. Again, the slight shoulder on the right of the largest peak is assigned to ionization due to Ne*($2p^53s$ $^3P_0$). Thus, the first peak in the $^3P_0$ progression should appear at $\varepsilon = (16.7154 - 12.071)$ eV $= 4.644$ eV, and the additional, *harmonic* peaks in the progression appear at 4.407, 4.171 eV, … and so on.

Table 4.8. FCfs for O_2 (X)

v'	FCf
0	0.184
1	0.362
2	0.293
3	0.126
4	0.031
5	0.0043
6	0.00033
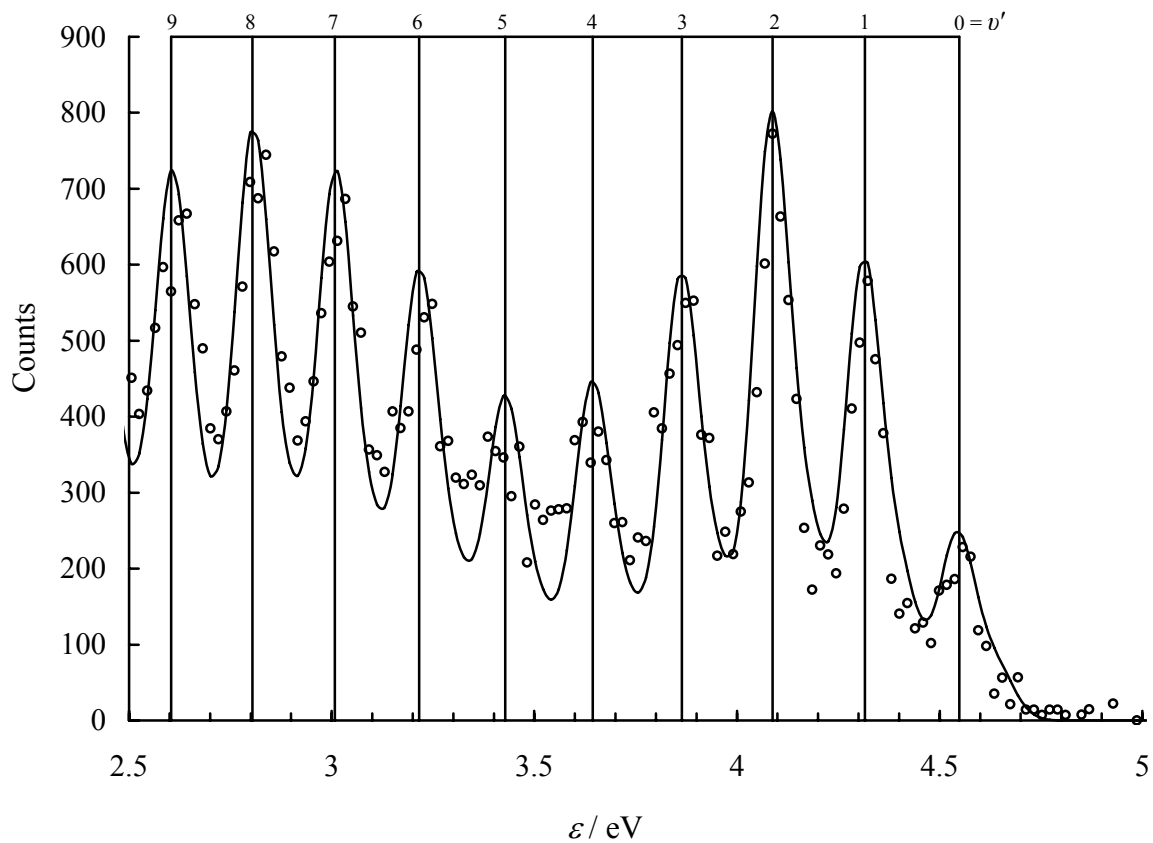
Figure 4.21: Ne*(40 °C) + O_2(40 °C). At these conditions E = 1.82 kcal/mol. The pitchfork shows the position of the $^3P_2$ vibrational progression, adjusted for anharmonicity. The circles are the transmission corrected data, and the solid line is the best fit of the transmission corrected data.

4.7 CARBON DIOXIDE

The final fits of the portions of the Ne* + CO_2 spectra that are due to v_1 excitation (we propose) are shown in Figures 4.22 and 4.23. For E = 1.73, 1.97, 2.55, and 3.13 kcal/mol, $\Delta\varepsilon_s$ = -18 ± 1, -18 ± 1, -19 ± 3, and 3 ± 1 meV, respectively. These results are shown graphically in Figure 4.24, which contains a point (the square in the plot) that is from Lescop *et al*. [7] who reported a line shift of 16 ± 2 meV for Ne*($^3P_2$) and 22 ± 2 meV for Ne*($^3P_0$) for Ne* + CO_2 at $E \approx 56$ meV = 1.3 kcal/mol. Again, $\Delta\varepsilon_s$ does not depend on J for our fits, so we plot an average shift value of 19 kcal/mol in Figure 4.24. For CO_2 v_1 excitation is represented by nv_1 and (n00), and, therefore, (100), (200), and so on. For CO_2 the ionization cross section decreases with increasing E, and the peak structure becomes less obvious as E increases, a result seen above for the diatomic molecules. (The ionization cross section is, qualitatively, a measure of the probability of reaction.) This result for CO_2 has been quantitatively determined previously. [14] This is of note, in particular, because there is a broad band of signal between 0.5 and 1.5 eV that is evident for the first two Es but that is not present at the two higher Es. See Figure 4.25. The assignment of the peaks buried in this region is a daunting task, and it is not attempted here. As for the region above 1.5 eV, Ne* can only ionize into the CO_2^+ $X\,^2\Pi_g$ electronic ground state, simplifying matters slightly. As a first attempt at fitting the well-resolved peaks above 1.5 eV, we assumed that nv_1 excitation is responsible for all of the well-resolved peaks. If true (see Tables 1.1 and 1.3), the largest peak in the Ne* + CO_2 spectrum, therefore, should appear at

(16.6191 − 13.7772) eV = 2.8419 eV. As above for the diatomics, additional peaks in the $^3P_2$

(n00) progression appear at (v' = 1 to 6) 2.6876, 2.5334, 2.3791, 2.2248, and 2.0706 eV, since

the nv_1 vibrational levels are separated by 1244.3 cm^{-1} = 0.15427 eV[60]. The shoulder on the

right of the largest peak is assigned to ionization due to Ne*($2p^5 3s$ $^3P_0$), with (harmonic) peaks in

the Ne* ($^3P_0$) progression at 2.9382, 2.7839, 2.6297, 2.4754, 2.3211, and 2.1669 eV. nv_1

excitation appears to account for the spectrum up through n = 3. (Such a result may be typical

for linear triatomics, as the Vecchiocattivi result [15] for the PIES spectrum for Ne* + N_2O bears

a resemblance to the PIES spectrum for Ne* + CO_2. The spectrum that they show, however, for

Ne*($^3P_{2,0}$) + N_2O contains no signal below 3.25 eV and only indicates peaks for the N_2O^+ $X\,^2\Pi$

vibrational progression for n = 0, 1, and 2.) As mentioned in Chapter 3, anharmonic correction

was not done, but, from PES spectra [29], we know that the anharmonicity is small for v_1 of

CO_2^+, and the fit should not be affected too much by this. Figure 4.26 shows a close up of the

1.8 − 2.5 eV region of the Ne* + CO_2 spectrum, where the n = 3 peak is at the far right. This

peak is fit very well, but the fit for the remaining intensity is very poor, indicating that nv_1

excitation is not solely responsible for the remaining peak intensities.

Previously, Cermak[61] and Lescop et al. [7] proposed that the vibrational progressions

present in the spectra of Ne* + CO_2 are the nv_1 and $nv_1 + 2v_3$ progressions. Lescop et al. [7]

indicate that the $nv_1 + 2v_3$ combination contributes from n = 2 to 5 and that the nv_1 progression

contributes to all five well-resolved peaks in the spectrum. We obtained a good fit without

contribution to the n = 2 and 3 peaks from the $nv_1 + 2v_3$ progression. Still, nv_1 can't explain the

whole spectrum, and $nv_1 + 2v_3$ is a good place to start to fit the additional peaks.
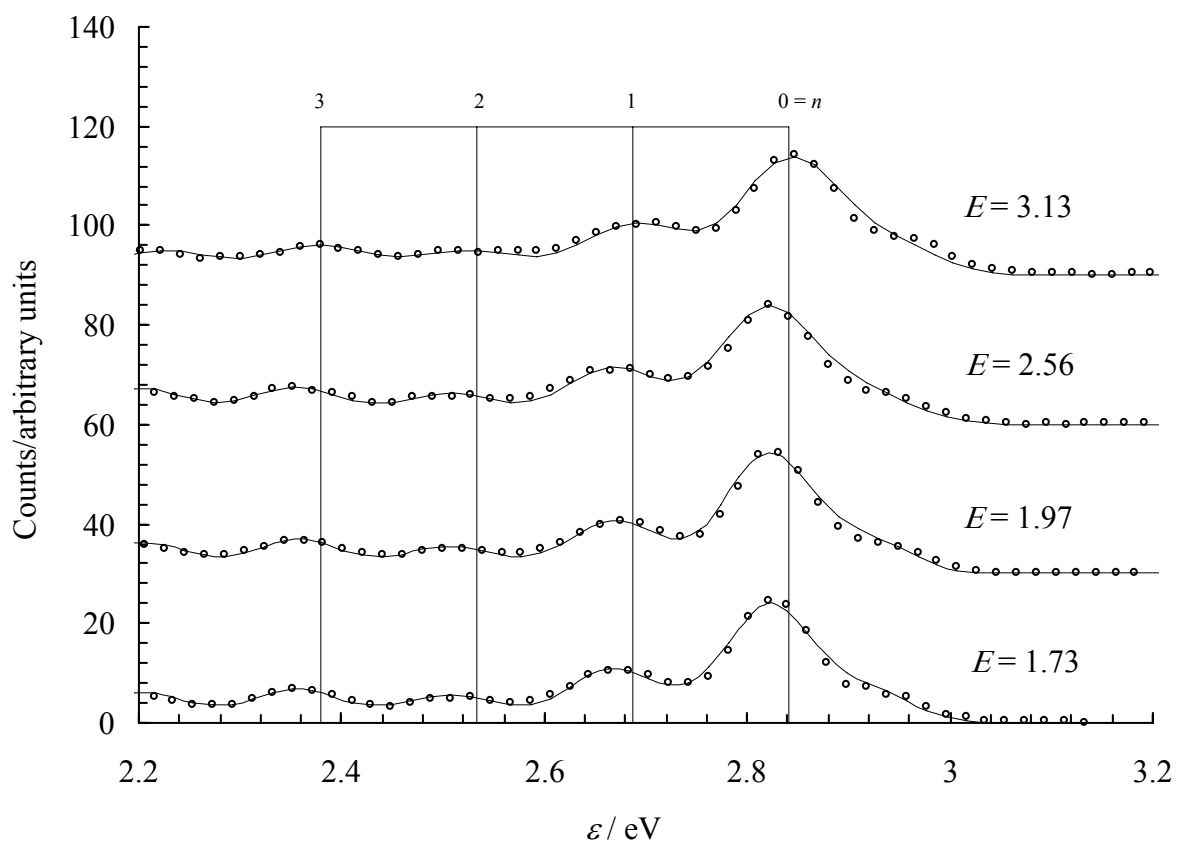
Figure 4.22: Ne* + CO_2(40 °C) for Ne* at T = 40, 110, 280, and 450 °C. The pitchfork shows the position of the $^3P_2$ vibrational progression for nv_1 excitation *only*, assuming harmonic behavior. The data have been normalized to equal intensity for each E(kcal/mol), and the baselines have been shifted for display. The circles are the transmission corrected data, and the solid line is the best fit of the transmission corrected data.
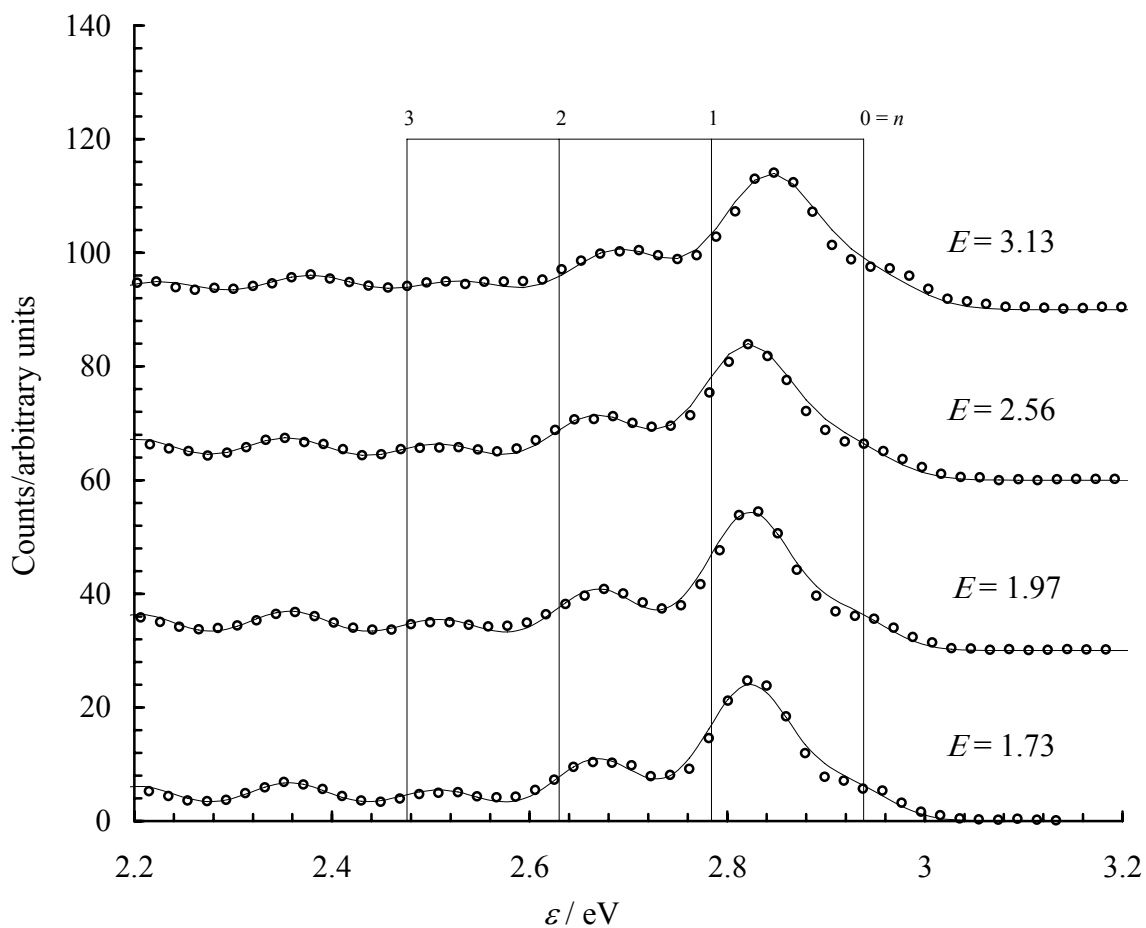
Figure 4.23: Ne* + CO_2(40 °C) for Ne* at T = 40, 110, 280, and 450 °C. The pitchfork shows the position of the $^3P_0$ vibrational progression for nv_1 excitation *only*, assuming harmonic behavior. The data have been normalized to equal intensity for each E(kcal/mol), and the baselines have been shifted for display. The circles are the transmission corrected data, and the solid line is the best fit of the transmission corrected data.
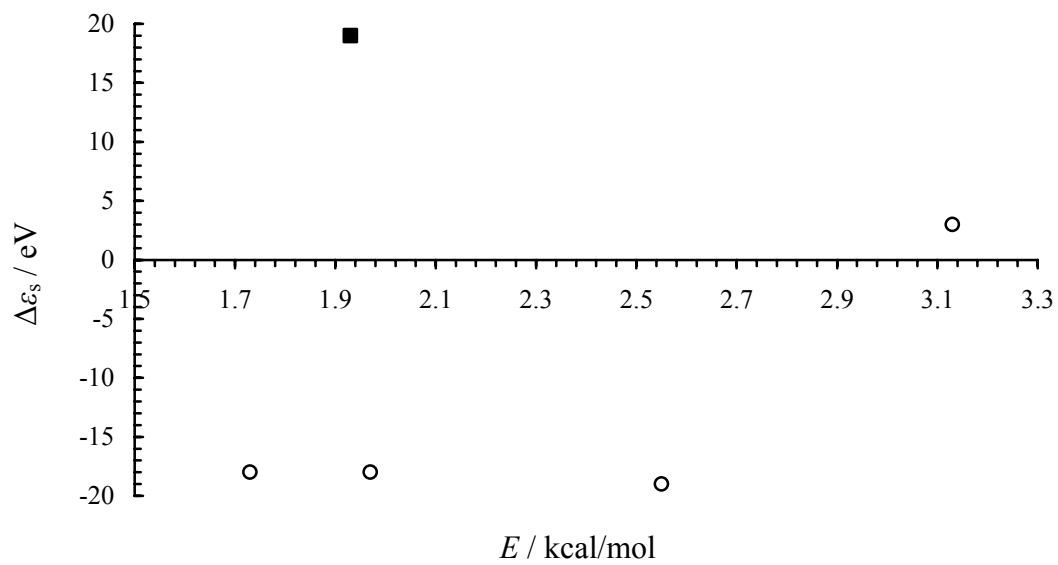
Figure 4.24: Collision energy dependence of the PIES shift for Ne* + CO_2. The circles are our data, and the square is averaged from the two J state values reported in Reference 7.
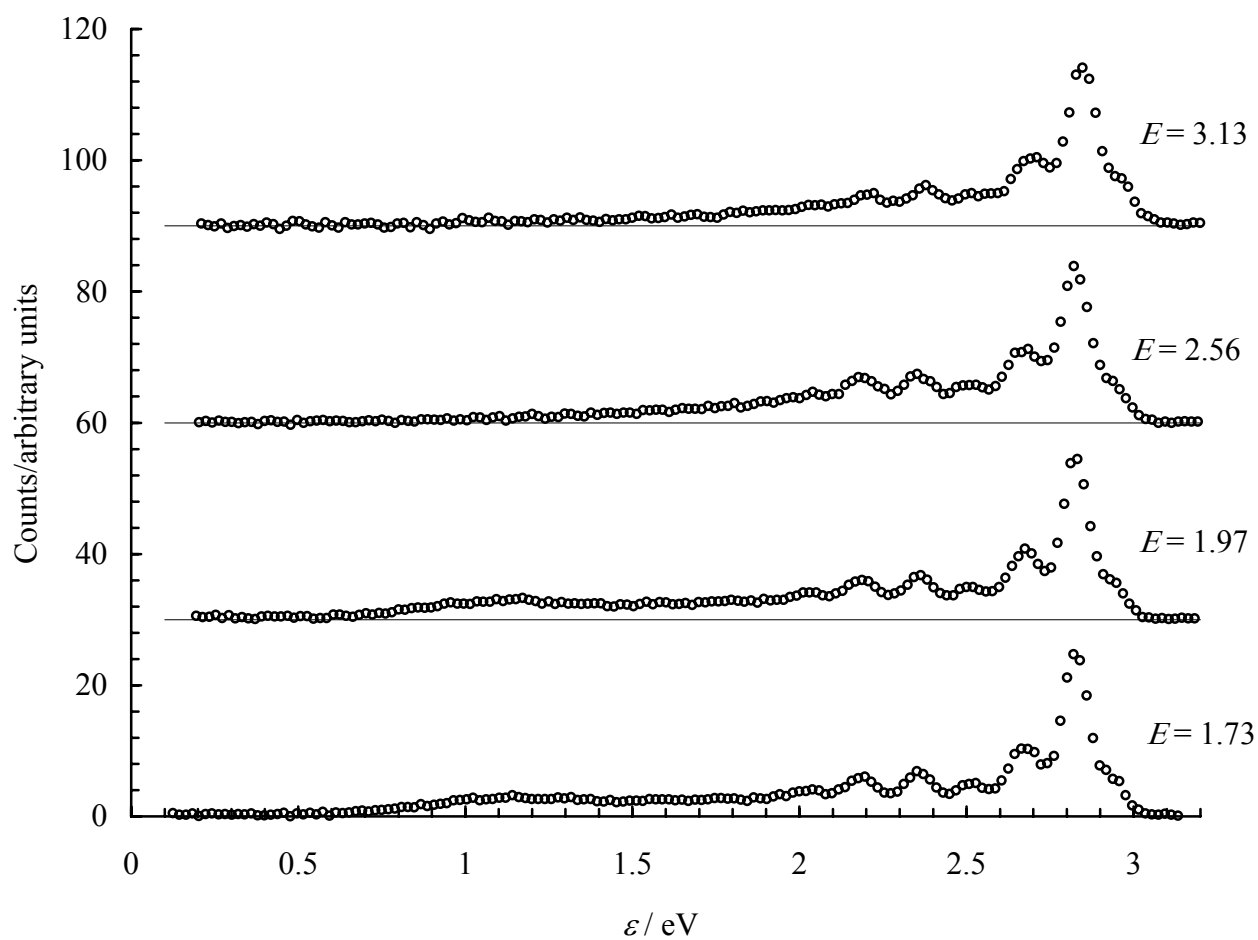
Figure 4.25: Normalized, transmission corrected, energy corrected PIES spectra for Ne* + CO_2 at four collision energies. ε is the kinetic energy of the ejected electrons. The collision energies E are in kcal/mol. The data points are separated by 0.0195 eV. Note the disappearance of the signal below 1.5 eV as E increases.
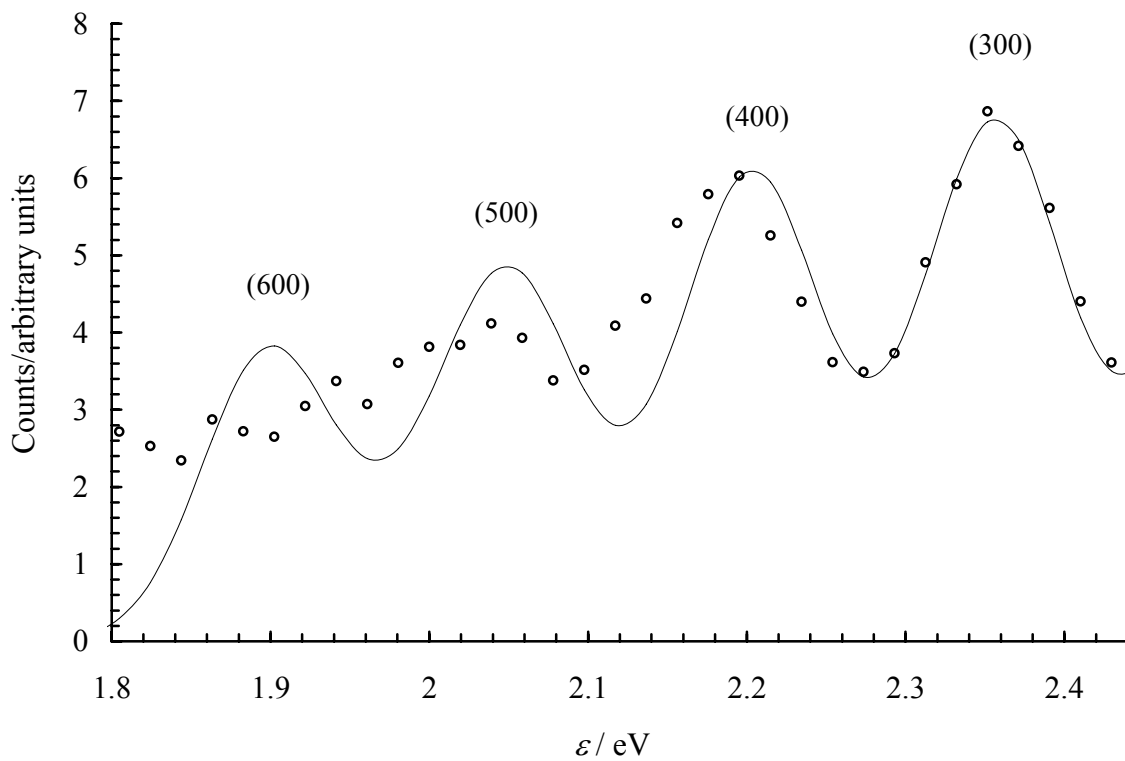
Figure 4.26: Attempted fit of a portion of the Ne*(40 °C) + CO_2 spectrum with only nv_1 excitation. The $n = 3$ peak is well represented by the fit, but the remaining peaks are poorly fit, indicating other vibrational modes are responsible for the intensity.

This assertion is not a random combination, of course, but it comes from selection rules that are pointed out by (at least) Eland and Danby:[62] the selection rule against excitation of the bending mode (v_2) is rigorous, and the antisymmetric stretch (v_3) can only be excited in units of two quanta. Further, a combination with $4v_3$, $6v_3$, … is expected to be much weaker than that with $2v_3$. Thus, this seems like a very reasonable assertion. However, our ability to fit the first four peaks of the Ne* + CO_2 spectrum with only nv_1 indicates that care must be taken to fit the spectrum independently before agreeing. Until populations can be determined and the proper intensity assigned to the nv_1 and $nv_1 + 2v_3$ progressions via a systematic fitting procedure, we can't suggest the contribution of the $nv_1 + 2v_3$ vibrational progressions ($^3P_2$ ($n02$) and $^3P_0$ ($n02$)) to the Ne* + CO_2 spectrum. To be quantitative, note that the v_3 vibrational levels are separated by 1423.08 cm^{-1} = 0.17644 eV. [29] It was shown above that the first peak in the $^3P_2$ v_1 progression should appear at 2.8419 eV. Thus, the first peak in the $^3P_2$ $nv_1 + 2v_3$ vibrational progression should appear at [2.8419 − 2(0.17644)]eV = 2.4890 eV. The spacing continues in units of 0.15427 eV, yielding peak positions of 2.3347, 2.1805, 2.0262 eV. Likewise, it was shown above that the first peak in the $^3P_0$ v_1 progression should appear at 2.9382 eV. Thus, the first peak in the $^3P_0$ $nv_1 + 2v_3$ vibrational progression should appear at [2.9382 − 2(0.17644)]eV = 2.5853 eV. The spacing continues in units of 0.15427 eV, yielding peak positions of 2.4311, 2.2768, and 2.1225 eV. Figure 4.27 contains a plot of these progressions with the transmission and energy corrected spectrum for E = 1.73 kcal/mol, showing that these progression do, indeed, appear at the appropriate energies to influence the spectrum. The degree to which they do is open to debate. Finally, the populations for the fit portion of the CO_2 spectra are given in Table 4.9 along with data from Lescop *et al.* [7] that has been estimated from Figure 3 in their paper. The table of data they give for $^3P_2$ nv_1 populations contains at least two errors.

Table 4.9: Nascent CO_2^+ populations[a] (P) and FCfs[63] for Ne*(3 $^3P_2$) + CO_2

nv_1 X state	$P(n)/P(0)$				$P(n)/P(0)$ average	$P(n)/P(0)$ Ref. 7	FCfs Ref. 63
	$E = 1.73$ kcal/mol	$E = 1.97$ kcal/mol	$E = 2.56$ kcal/mol	$E = 3.13$ kcal/mol			
0	1	1	1	1	1	1	1
1	0.4557 ± 0.0047	0.4428 ± 0.0067	0.4772 ± 0.0198	0.4430 ± 0.0087	0.4547 ± 0.0162	0.45	0.122
2	0.2074 ± 0.0030	0.2050 ± 0.0059	0.2444 ± 0.0173	0.1882 ± 0.0072	0.2113 ± 0.0237	0.14	0.019
3	0.2678 ± 0.0035	0.2694 ± 0.0051	0.2929 ± 0.0147	0.2409 ± 0.0057	0.2678 ± 0.0213	0.17	–

[a] These data assume that the v_1 CC symmetric stretch is the only mode to give significant intensity at this resolution.
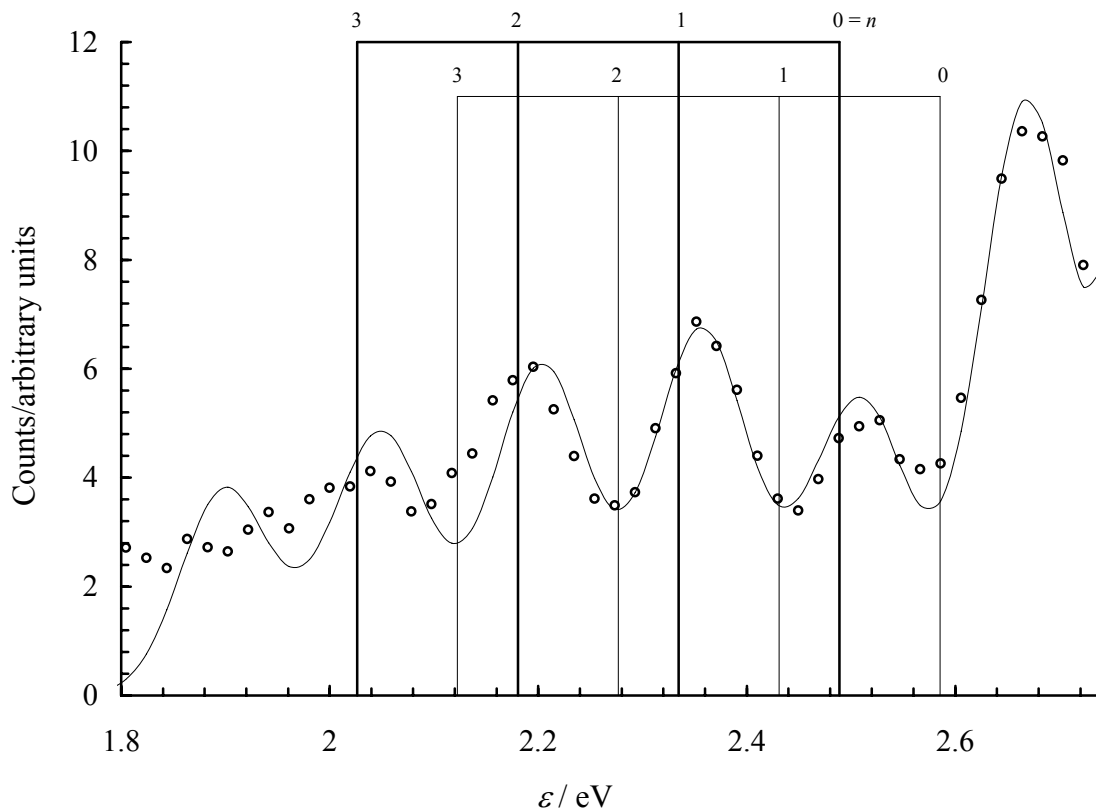
Figure 4.27: Ne*(40 °C) + CO_2 spectrum with transmission and energy corrected data. The circles are transmission corrected data. The curve is the fit of the data, assuming only $n v_1$ excitation. The dark pitchfork shows the $^3P_2$ (n02) progression. The light pitchfork shows the $^3P_0$ (n02) progression.

For $n = 4$ and 5 Lescop *et al*. [7] give populations of 0.12 and 0.08, but no comparison is made to these values in Table 4.9 because these were not part of the fit obtained here. Using the figure they provide, we get excellent agreement on the relative populations of the first two peaks in the spectrum.

Figure 4.28 contains a plot of the FCfs for the run of Ne*(40 °C) + CO_2(40 °C). The FCfs die off quickly, indicating that Frank-Condon behavior is not observed in the case of CO_2. We note a few observations before moving on. The reactions at $E =$ 1.73, 1.97, and 2.56 eV shown in Figure 4.22 are very similar with respect to peak shape and peak position, each occurring with a small red shift. Further, the broad peakshape for the $v = 0 \rightarrow v' = 0$ transition with FWHM $\approx$ 0.12 eV, which is significantly larger than the shift. This small shift and relatively large FWHM indicates that the electron ejection occurs very near the crossing point of V_0, that is, over geometries that occur at positive and negative regions of V_0. Our initial finding of a red shift must be contrasted with the blue shift reported by Lescop *et al*. [7] This E is below what we measured, and it is possible that changing collision dynamics, such as transition state geometry, could alter $\Delta\varepsilon_s$ between 1.3 kcal/mol and 1.73 kcal/mol. Our reaction for which $E =$ 3.13 kcal/mol differs in peak position from the other three reactions, and the slight blue shift indicates that its ionization must occur at significantly shorter R and, therefore, at a more repulsive region of the V_0 curve. (Remember, we are ignoring the complexity of potential *surfaces* (not 1-D curves), which are the true representation for Penning ionization of *molecules*.) This, coupled with the Lescop *et al*. result, would mean that the Ne* + CO_2 reaction alternates between blue, red, and blue shifts. This is surprising if true, but it could indicate competing mechanisms, as we explore below.

Figure 4.28: Normalized FCf's for Ne*(40 °C) + CO_2(40 °C). The FCf's appear as thick black lines, positioned arbitrarily at the peak maximum. Only three FCf's are visible at this scale, including the very small line at 2.51 eV.

4.8 ETHYNE

The Ne* + C_2H_2 experiment was performed at $E = 1.80$, 2.37, and 2.94 kcal/mol, giving $\Delta\varepsilon_s = 48 \pm 1$, 34 ± 1, and 33 ± 2 meV, respectively. These results are shown graphically in Figure 4.29. The square in Figure 4.29 is an average of the data from Lescop *et al.* [10] who reported $\Delta\varepsilon_s = 25 \pm 4$ meV for Ne*($^3P_2$) and 30 ± 4 meV for Ne*($^3P_0$) for $E \approx 1.3$ kcal/mol. Figure 4.30 shows the difficulty associated with the Ne* + C_2H_2 calibration. Namely, the *A* state PES peaks and the *X* state PIES peaks overlap in the $\varepsilon = 4.5 - 5$ eV region, and, more importantly, even the C_2H_2 PES spectrum by itself (i.e., no simultaneous Ne* + C_2H_2 experiment) is not resolved well enough with our data to accurately determine the adiabatic peak for the *A* state, evidenced by comparison of our spectra with the high resolution spectra that have been obtained by Ruett *et al.* [51] and Avaldi *et al.* [40]. See Figure 4.30. The adiabatic transition value that is given in these papers occurs weakly due to very poor FC overlap, which is likely the result of a significant rearrangement from linear to bent geometry in the *A* state. For this reason, only the *X* state PES peaks were fit in the calibration. This assumes the instrument shift is constant over the range of interest, which is generally what has been observed. The difficulty with transmission correction at low energy, along with the complex *A* state spectrum of $C_2H_2^+$, manifests itself in data at low ε which is unable to be trusted or fit for the Ne* + C_2H_2 reaction. Consequently, only the *X* state for $C_2H_2^+$ is fit. (The previous work of Lescop *et al.* [10] on Ne* + C_2H_2 likewise did not include a presentation of the *A* state.) This is somewhat surprising when one notes that the difference between the *A* state adiabatic ionization energy for C_2H_2 and Ne*($^3P_2$) is 0.322 eV and

0.418 eV for Ne*($^3P_0$). (See Tables 1.1 and 1.3.) The lack of structure in the spectra at εs that

are trustworthy (0.322 and 0.418 eV) must, therefore, be due to the complex structure of the *A*

state spectrum and the very weak peaks early in the *A* state progression. See Figure 4.31. The

large peak at ~ 0.08 eV is the result of unsuccessful transmission correction of the data at very

low ε. This same problem is evident in Figures 4.5 and 4.8. It is noteworthy, though, that the

signal at low ε *is* PIES signal, because, for example, the Ne* + CO_2 reaction produces no such

peak; Penning spectra are very "quiet".
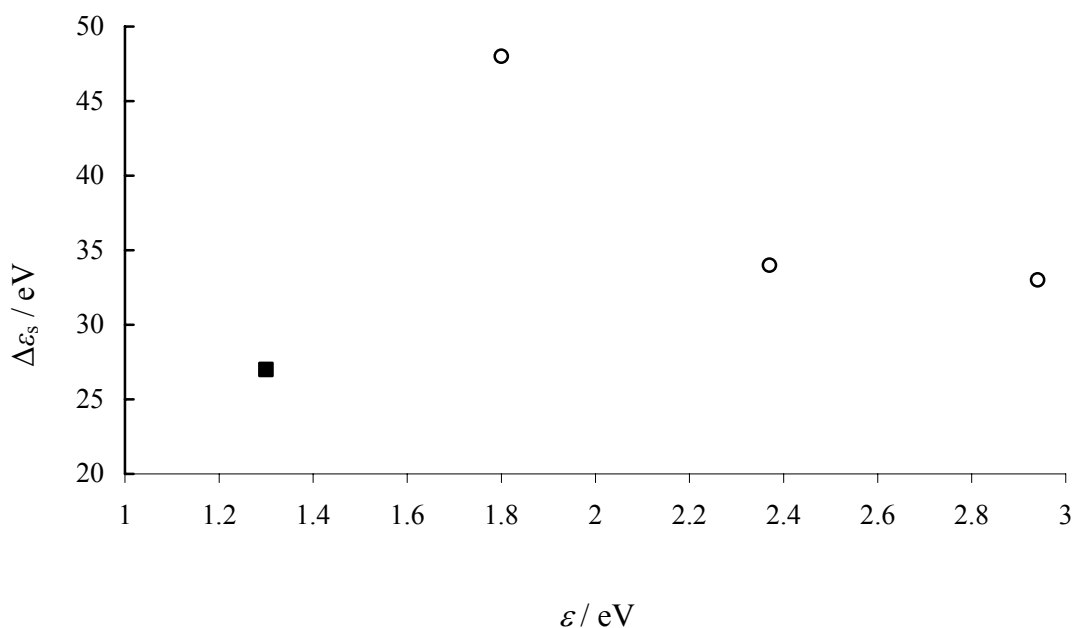
Figure 4.29: Collision energy dependence of the PIES shift for Ne* + C_2H_2. The circles
are our data, and the square is the average of the line shifts for both *J* states from
Reference 10.
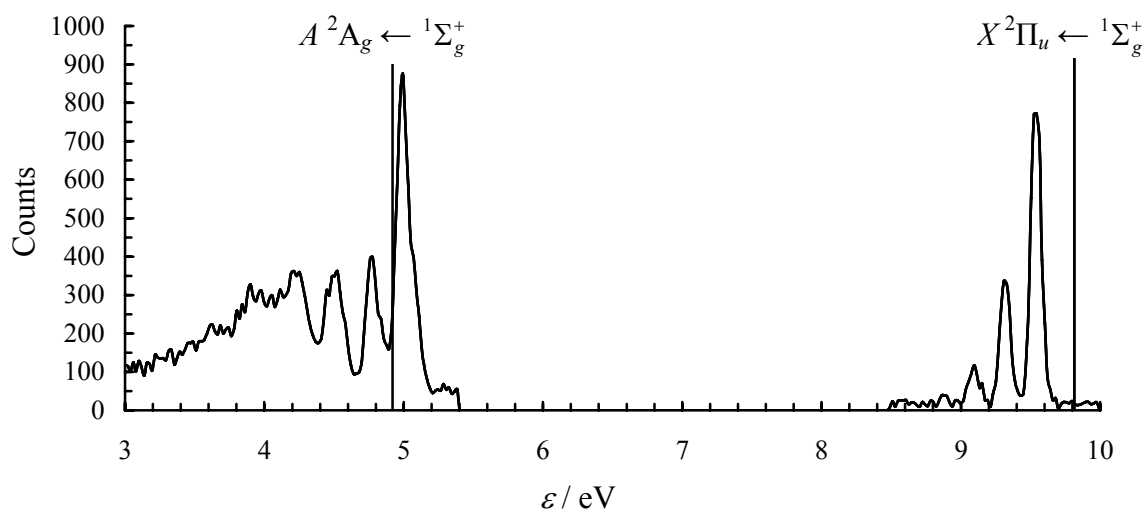
Figure 4.30: Ne*(40°C),HeI + C_2H_2 calibration. The vertical lines indicate the literature peak positions for the PES adiabatic transitions for the X and A states of $C_2H_2^+$. The accepted values for the adiabatic transitions are given by subtracting the values in Table 1.3 from 21.21804 eV. Only the X state can be resolved for calibration purposes. (Some authors, for convenience, use the notation $A\,^2\Sigma_g^+ \leftarrow {}^1\Sigma_g^+$, but this is only true for $D_{\infty h}$ symmetry, which the A state ion does not possess. [40, 51])
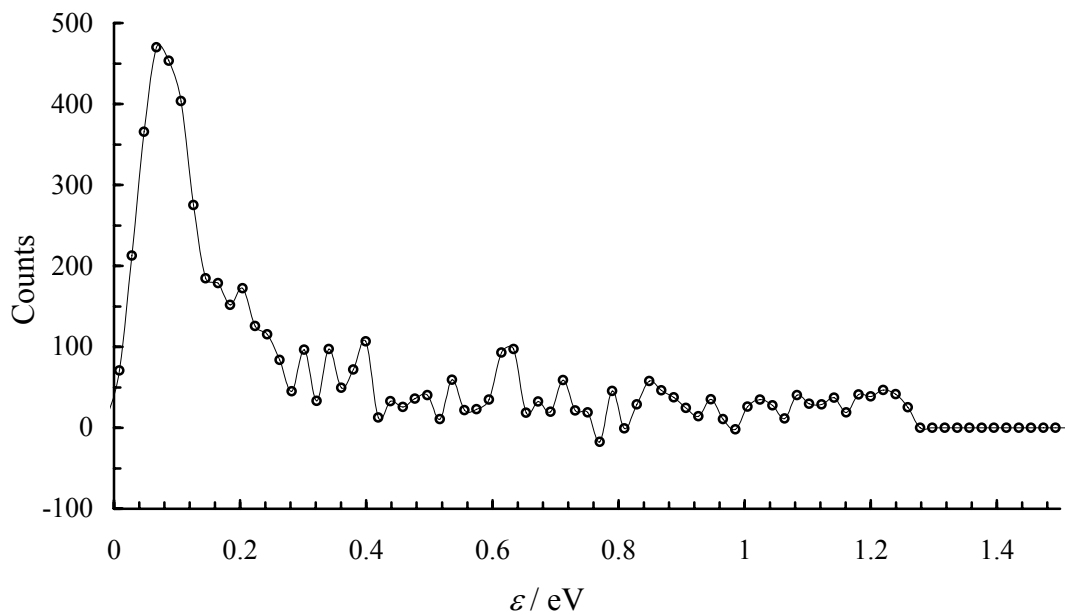
Figure 4.31: Transmission corrected Ne*(40 °C) + C_2H_2 PIES spectrum. ε is the kinetic energy of the ejected electrons. The line and circles represent the same data.

The final fits of all three Es for Ne* + C_2H_2 are shown in Figures 4.32 and 4.33. The spacing of our data agrees well with fits assigned to the $n = 0 \rightarrow 3$ progression of the $C_2H_2^+$ X $^2\Pi_u$ (0n000) state. n is the quantum number for excitation of nv_2 (the CC stretch) which equals[64] 1829 cm^{-1} = 0.2268 eV. (Yang and Mo[65] reported a value of 1818 cm^{-1} for v_2 in $C_2H_2^+$.) Tables 1.1 and 1.3 give ε_0 = 5.216 eV for the adiabatic transition into the $C_2H_2^+$ X electronic state for reaction with Ne* ($^3P_2$). For Ne* ($^3P_0$), ε_0 = 5.312 eV. Thus, as shown above for the other molecules, the spacing between the peaks due to the $^3P_{2,0}$ harmonic progressions are determined by simply subtracting units of 0.2268 eV from 5.216 and 5.312 eV, respectively. Also as above, Figures 4.32 and 4.33 indicate the pitchforks with anharmonic correction. The relative vibrational populations (relative peak areas) and FCfs for Ne*(3 $^3P_2$) + C_2H_2(40 °C) are shown in Table 4.10. Figure 4.34 clearly shows that C_2H_2 + Ne* exhibits FC behavior.

Increasing blue shift and concomitant peak broadening are consistent with transitions that occur over a predominantly repulsive excited-state potential energy curve, a result seen in previous work for Ne* + H_2. [20] Our results for C_2H_2, as seen in Figure 4.32, however, are mixed. All of the spectra have a sizable blue shift ($\Delta\varepsilon_s > 0$), indicating that electron ejection occurs primarily on the repulsive part of V_0, as described above, but the blue shift *decreases* with increasing E. To explain *increasing* blue shift as E increases, refer to Figure 1.3. As E increases, the reactants are able to approach more closely, that is, reach smaller R values, before reaction occurs. Therefore, they are higher up on the repulsive part of V_0 when the transition occurs, leading to larger blue shifts. That we get *decreasing* blue shift with increasing E is not typical and could be due to changing dynamic factors as E increases. A survey of the literature
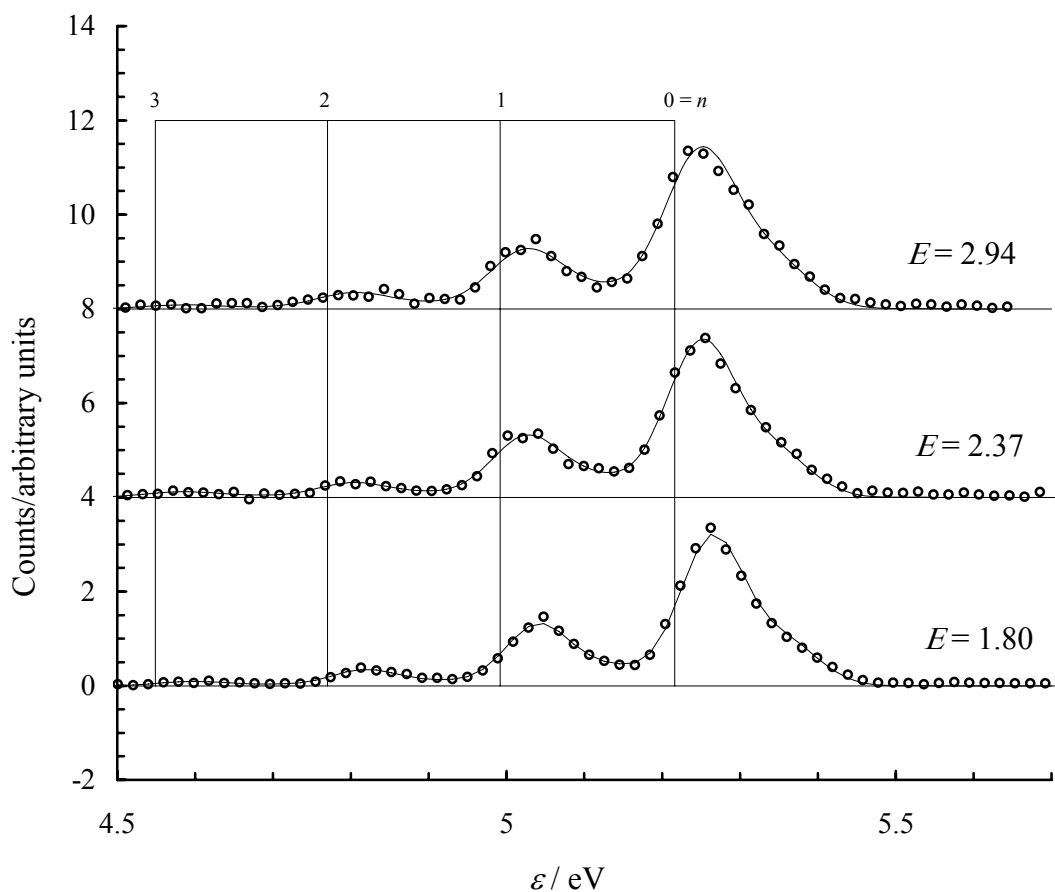
Figure 4.32: Ne* + C_2H_2(40 °C) for Ne* at T = 40, 245, and 450 °C. The pitchfork shows the position of the Ne* ($^3P_2$) vibrational progression for v_2, adjusted for anharmonicity. The data have been normalized to equal intensity for each E(kcal/mol), and the baselines have been shifted for display. The circles are the transmission corrected data, and the solid line is the best fit of the transmission corrected data. n refers to the notation ($0n000$) for the v_2 normal mode as described in Chapter 2.
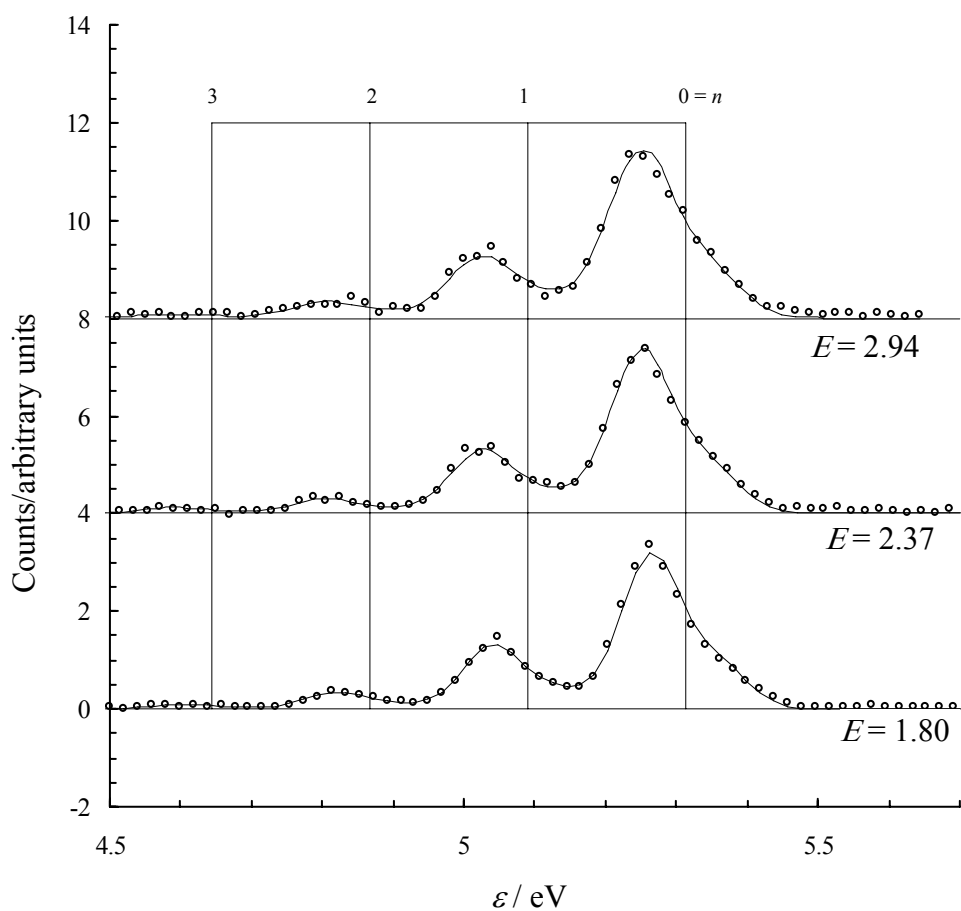
Figure 4.33: Ne* + C_2H_2(40 °C) for Ne* at $T = 40$, 245, and 450 °C. The pitchfork shows the position of the Ne* ($^3P_0$) vibrational progression for v_2, adjusted for anharmonicity. The data have been normalized to equal intensity for each E(kcal/mol), and the baselines have been shifted for display. The circles are the transmission corrected data, and the solid line is the best fit of the transmission corrected data. n refers to the notation ($0n000$) for the v_2 normal mode as described in Chapter 2.

Table 4.10: Nascent $C_2H_2^+(X)$ populations[a] (P) and FCfs[66] for Ne*(3 $^3P_2$) + C_2H_2

nv_2 X state	$P(n)/P(0)$ $E = 1.80$ kcal/mol	$P(n)/P(0)$ $E = 2.37$ kcal/mol	$P(n)/P(0)$ $E = 2.94$ kcal/mol	$P(n)/P(0)$ average	$P(n)/P(0)$ Ref. 10 ($^3P_2$)	$P(n)/P(0)$ Ref. 10 ($^3P_0$)	FCf experimental Ref. 66
0	1	1	1	1	1	1	1
1	0.4120 ± 0.0027	0.3946 ± 0.0020	0.3719 ± 0.0023	0.3928 ± 0.0201	0.42	0.57	0.42
2	0.1081 ± 0.0012	0.0935 ± 0.0010	0.1017 ± 0.0012	0.1011 ± 0.0073	0.11	0.16	0.12
3	0.0404 ± 0.0008	0.0357 ± 0.0008	0.0249 ± 0.0008	0.0337 ± 0.0079	0.03	0.05	0.02

[a]These data assume that the v_2 CC symmetric stretch is the only mode to give significant intensity at this resolution.
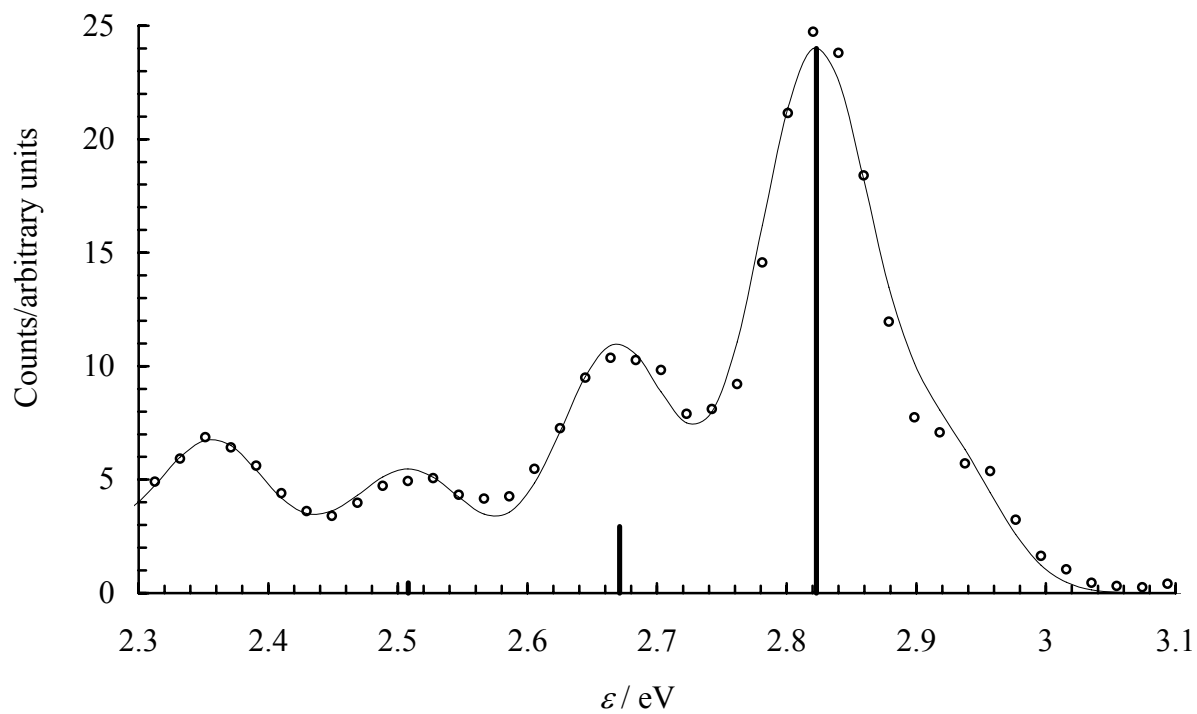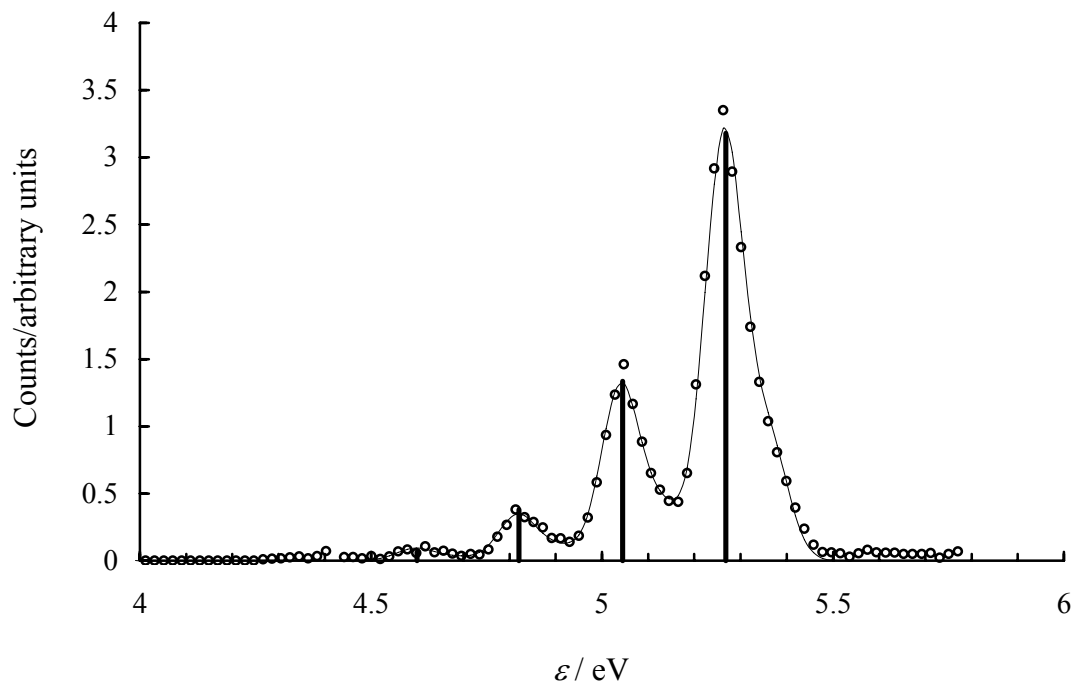
Figure 4.34: Normalized FCf's (*X* state) for Ne*(40 °C) + C_2H_2(40 °C). The FCf's appear as thick black lines, positioned arbitrarily at the peak maximum. Only significant FCfs are shown.

produced no other dependence of the line shift on E studies for Ne* + C_2H_2, so we do not have another group's work with which to compare our result. Lescop *et al*. [10] did conduct Ne* + C_2H_2 at E = 1.2 kcal/mol and found a blue shift of $\Delta\varepsilon_s$ = 25 ± 4 meV for the $^3P_2$ (01000) ← (00000) transition and $\Delta\varepsilon_s$ = 30 ± 4 meV for the $^3P_0$ (01000) ← (00000) transition. See Figure 4.29. Their value does not agree with our observed trend, but they did find a blue shift. Further, both groups have found that the magnitude of $\Delta\varepsilon_s$ was larger for C_2H_2 than for CO_2. Figure 4.32 also shows that there is peak broadening as E increases. For the $v' = 0 \leftarrow v = 0$ transitions FWHM ≈ 0.1 eV for E = 1.80 kcal/mol and FWHM ≈ 0.12 eV for E = 2.94 kcal/mol. Peak broadening is chiefly the result of the sharp increase in $\Gamma(R)$ at short R. $\Gamma(R)$ is an "enabler" for the reaction, and, as described above, it is quantum mechanical. Thus, as $\Gamma(R)$ grows, the range of R values over which the *same transition* can occur increases, and the peak broadens. A minor contributing factor to peak broadening is that the velocity distribution in our beam increases as E increases. See Chapter 2. (The above explanation implies that we should never see a red shift and peak broadening. If anything, the peaks might become more narrow.)

5.0 EXPERIMENTAL CONCLUSIONS

5.1 EXPERIMENTAL AND PEAK FITTING ISSUES

Above we mentioned that *ideally* the transmission correction would be performed at the prevailing conditions for each experiment. This was simply not possible in all cases and is of concern because the heights of the peaks are ultimately determined by the transmission correction. Note that even with a consistently functioning instrument, the transmission correction function is difficult to determine, as Bussert *et al*. [59] have also stated. Obtaining an accurate transmission correction is difficult, owing to a large flux of low-energy background electrons when the UV resonance lamp is on and to surface charge(s) in unknown places in the analyzer or elsewhere. The noise at low ε makes the correction even more problematic in this region, and this, in turn, makes fitting peaks at or near threshold (less than ~0.2 eV) impossible. All of the data that were fit in this paper employed a linear transmission correction, even though the actual function might be more complicated. Thus, a goal for a second round of fitting is to determine the effect, if any, of more complex transmission correction functions.

Over time, cleaning the instrument analyzer, which involves baking the analyzer, has warped it. This leads to a slightly altered ΔV, as described in Section 2.3, Equation 3. Since the kinetic energy that the instrument output meters display depends on the pass energy being what

the dials indicate, warping of the analyzer leads to error. The exact magnitude of the impact of the warped analyzer is virtually impossible to know, but, when we are looking for shifts on the order of 10's of meV, it is a concern. There is also hope that the new Mo apertures in the analyzer will provide better reproducibility. The fact that the data for NO and C_2H_2 show decreasing blue shift with increasing E is rather uncommon, and a return to these experiments for new data is strongly desired. Since it happened for two different target molecules and was obtained with high quality spectra, this trend appears to be genuine. The meaning of it, however, remains a mystery. The error on our line shift values was low. Note, however, that one run of CO and both X state values for NO had errors of ± 3. The $E = 2.81$ kcal/mol value for CO had more noisy PES peaks than usual, as did the NO PIES peaks in their respective calibration runs. More noise is always expected when the UV lamp is on, but these were three cases where the data were more noisy that usual. We can suggest that the $\Delta\varepsilon_s = 69 \pm 3$ meV value for CO is possibly lower because, while a linear relation between $\Delta\varepsilon_s$ and E has in no way been proven here, Figure 4.6 may indicate that the value for $E = 2.81$ kcal/mol is slightly high. Of course, within the error of each value this is not proven either.

Another experimental issue is the accuracy of the Ne*($2p^53s\ ^3P_2$) / Ne*($2p^53s\ ^3P_0$) intensity ratio of 3.35 ± 0.20. As mentioned above, this is difficult to measure and, in fact, was not measured during the author's tenure at the University of Pittsburgh. Thus, we assumed no change in the performance of the electron gun. We can take some comfort, though, by a determination of the impact of the margin of error, ± 0.20. Our fitting program was run on H_2 at the extremes of the ratio (3.55 and 3.15), and the impact on the results was very slight. $\Delta\varepsilon_s$

changed by 1 meV, and the population change was 0.25 %. Thus, slight fluctuations in the electron gun performance are not expected to have caused much error in our results.

The peak fitting and population analysis that we performed above for the 5 diatomic molecules was done in the most consistent manner possible. Further analysis is always possible and has, in fact, been done for Ne* + H_2 in Reference 20, a template for further analysis. The alternative fitting that was performed in Reference 20, although even that fitting did not utilize a more complex transmission correction, was able to resolve the ambiguity about which peak ($v' = $ 1 or 2) in the H_2 spectrum was the most intense. There, it is shown that the $v' = 2$ peak is the most intense peak in the Ne* + H_2 PIES spectrum. This is not to denigrate the fits that we have made here. The visual inspection test that we mentioned above, while not as analytical as the χ^2 test, is nonetheless a surprisingly good test to gauge the quality of a fit. The vast majority of the fits that we have achieved here are good, and we do not expect large changes in the PIES shifts nor the populations should further fitting be attempted. As a whole H_2 has the worst fits of all, and the fits get slightly worse for all of the molecules as E increases since the true line shape begins to emerge, which, evidently, is not best represented by a least squares fit Gaussian function. Other than this, the only other consistent problem is the $v' = 1$ peak for N_2. To predict how much change (perhaps, improvement) we expect in $\Delta\varepsilon_s$ and populations with further fitting, let us compare the H_2 results that we obtained here with those found in Reference 20. The $\Delta\varepsilon_s$ comparison is done in Table 5.1, and the $P(v')/P(2)$ comparison is done in Table 5.2. In Table 5.2 we use the average of the runs for which $v' = 2$ was the largest peak.

Table 5.1. Comparison of $\Delta\varepsilon_s$ for H_2 from two fits

E (kcal/mol)	$\Delta\varepsilon_s$ (meV) this work	$\Delta\varepsilon_s$ (meV) Ref. 20	% Difference
1.83	63.9 ± 0.2	64.2 ± 0.3	0.5
2.50	84.4 ± 0.1	73.3 ± 0.6	14
3.16	93.6 ±0.2	75.0 ± 0.7	22
3.89	107.3 ± 0.1	96.3 ± 0.7	11

Table 5.2. Comparison of $P(v')/P(2)$ for H_2 from two fits

v'	$P(v')/P(2)$ average of runs 1 and 3 in this work	$P(v')/P(2)$ Ref. 20	% Difference
0	0.5071 $\pm$ 0.0452	0.51 $\pm$ 0.05	0.6
1	0.9679 $\pm$ 0.0436	0.96 $\pm$ 0.03	0.8
2	1	1	0
3	0.6885 $\pm$ 0.0007	0.72 $\pm$ 0.06	4.4
4	0.4085 $\pm$ 0.0041	0.43 $\pm$ 0.01	5.1

The elementary percent difference calculation for $\Delta\varepsilon_s$ shows that for the higher energies there are significant, though not extreme, differences between the values obtained from the two fits. The same increasing blue shift trend is observed for both fits, but this simple comparison reveals that fitting is an imperfect science. Note that the values of $\Delta\varepsilon_s$ that we obtained in this dissertation increase in a more systematic way. In Reference 20 the $\Delta\varepsilon_s$ values are very close for $E = 2.50$ and 3.16 kcal/mol. If taken at the extremes of the error, they are nearly identical (73.9 and 74.3 meV). If true, this would be very odd. The Reference 20 fits are successful, however, in that the fits of all four energies show that the $v' = 2$ peak is the most intense. This agrees with Bussert et al. [59], and this dissertation makes no argument against this find. Nonetheless, the v' $= 1$ and $v' = 2$ peaks have very similar heights, and Table 5.2 shows that the population ratios obtained in this dissertation are within the margins of error of those determined in Reference 20. This is very encouraging and allows us to have faith in the integrity of the H_2 results presented here and not to regard them as poor. The three step fitting process described in Reference 20 evidently is required, however, to achieve fits with the $v' = 2$ peak as the highest peak. The fits for the remaining diatomic molecules are better than those for H_2, and we expect that there will be even less difference between any additional fits than we found for H_2. An important find, however, in Reference 20 that needs to be explored in the future is the dependence of $\Delta\varepsilon_s$ on v'. This was attempted in a rudimentary fashion for the other molecules of this dissertation, and no significant improvement in the fit was noted, leading to the conclusion that there is no dependence of $\Delta\varepsilon_s$ on v'.

A major issue with our fitting program is its inability to fit spectra with a large number of peaks. This was most prevalent with NO and O_2. In both cases, peaks that appear early in the

progression had to be held constant, their peak heights fixed at the transmission corrected values. Of course, when the peak heights are held constant, they are not allowed to be adjusted by gelspec2.for to obtain the best Gaussian lineshape for the data. This affects the population output and defeats attempts to treat all data and peaks in the identical manner. While this effect is small, given that we fixed the peak heights at the transmission corrected values, it is troubling that our fitting program requires inconsistent treatment of spectra. The reason for the failure of the program for spectra with a large number of peaks remains a total mystery to all group members, and it is an issue that needs to be addressed in the modification of gelspec2.for. Additionally, we noted above that the $v' = 1$ peaks of the N_2 spectra were not fit as well as we would like. Further, for the seeded runs the $v' = 1$ peaks are not well fit at the peak maxima. Attempts to to alleviate this problem by accounting for asymmetry of the peaks were not successful. When this asymmetry parameter was varied, the PIES shift that was calculated was essentially identical for all three seeded runs (around 58 meV). This result is not correct by simple inspection of the data, but it could be due to other fitting parameters that can be better utilized or could indicate an additional parameter might be needed. Thus, the present N_2 fits were obtained without an asymmetry parameter. A possible source of error in the fit of the $v' = 1$ peak is that the fit of the Ne*(seeded) + N_2 experiments ignores the $^3S_1$ state of He*. Any effect due to this is expected to be small, however, given the peak ratio He*($^3S_1$)/He*($^1S_0$) = 0.11. Further, the excitation energy of He*($^3S_1$) is 0.80 eV less than that of He*($^1S_0$), placing the He*($^3S_1$) peak under the $v' = 0$ peak of the N_2 progression, not the $v' = 1$ peak. Despite the issues with gelspec2.for, we again note the importance of the visual inspection of the fit. Overall, our fits were quite good. These issues need to addressed, but they do not seem to indicate any fundamental flaw in the program.

We end this section with an observation regarding a possible population dependence on E. We found for H_2 that no discernable dependence exists [20]. This is not really possible to detect in this dissertation, given the inability to fit the data to give the $v' = 2$ peak as the tallest peak at each E. The case for CO, however, seems to indicate a definite relationship. Of the 32 possibilities in Table 4.3 only one population bucks the trend of an increase in population relative to the $v' = 0$ peak as E increases for every peak. N_2 might show a possible decrease in populations as E increases. With only two Es for NO and a single E for O_2 insufficient data exists to make any decision regarding this issue for these molecules. If the trend is even real, possible models for this must wait for future work.

5.2 EXPLANATION OF SPECTRA AND FUTURE WORK

The major issue for spectroscopists is to explain observed spectra via peak assignments, population determination, and models. As mentioned throughout this dissertation, this is often done through analysis of orbital energies, the energy of the exciting or ionizing agent, and FC or non-FC behavior. The peak assignments and populations above are, for the most part, not open to debate. This is even more true for this dissertation than for one based on He*, given the much smaller excitation energy of Ne* than that of He*. There is less possible overlap of progressions, simplifying, in some respects, our work. The one issue, however, that is not simplified for Ne*

versus He* is the non-FC behavior that was observed for H_2, CO, N_2, NO, O_2, and CO_2. An understanding of the non-FC behavior that we observed in our reactions can be gained by a comparison of the NeI/Ne* population results compared to those of HeI/He* in previous and current work.

H_2: Bevsek[4], Bevsek, Dunlavy, and Siska[17], Bregel et al.[67] and many others have demonstrated that the He* + H_2 reaction yields populations for $H_2(v = 0) \rightarrow H_2^+(v')$ that closely follow FCfs. In the case of Ne* + H_2, however, there is a greater difference between the relative populations and the FCfs. There appears to be a systematic deviation from FCfs. [20] Both HeI + H_2 and NeI + H_2 PES essentially exhibit FC behavior. HeI has a much longer vibrational progression, due to its higher energy photons than NeI. Thus, any potential non-FC behavior for NeI + H_2 PES is impossible to observe since it NeI can only ionize up to the $v' = 4$ level. (Such a statement ignores any perturbation of energy levels.)

CO: The work of Bevsek[4], Yee et al.[68], and Harada et al.[69] has shown that He*($^1S_0$, $^3S_1$) + CO follows FC behavior closely for the X state with the X state peaks at essentially zero intensity after $v' = 2$. Also of note is that the A state population is much lower than that observed in HeI + CO, an indication of the chemical nature of PIES. The higher X and B state populations relative to the A state population is most likely explained by the better overlap between the $2s$ AO of the metastable He* and the 4σ and 5σ MOs, as opposed to the 1π MO. [69] In Ne* + CO there is a much longer X state progression, as seen in this work and that of others [13]. This longer X state progression is also observed[70,71] for NeI($^1P_1$, $^3P_1$) + CO PES. The $v' = 0$ and 1 peaks were explained in the PES results by direct FC transitions [71]. Above $v' = 1$, the peaks

were explained as the result of an autoionizing Rydberg state that undergoes radiationless transitions to the ground ionic state.

N$_2$: The case of N$_2$ is similar to that of CO. Dunlavy and Siska[18] obtained a He* + N$_2$ spectrum with a bimodal X state peak progression. The X state $v' = 0$, 1, and 2 relative populations were 1, 0.0845, and 0.0108. The X state resumes with significant populations for those peaks from $v' = 6$ to 11. We can't reach the $v' = 6$ to 11 peaks with the less energetic Ne*, but this bimodal distribution is theoretically important. Our Ne* + N$_2$ results show significantly greater relative populations of the $v' = 1 - 3$ levels than in the case of He* + N$_2$. The enhanced population of these levels (versus HeI + N$_2$ PES) is also seen in NeI($^1P_1$, $^3P_1$) + N$_2$ PES. [71]

NO: For He*(2 ^3S) + NO, Brion *et al*.[72] found that Penning ionization from NO to the ground electronic state of NO$^+$ is vertical within experimental error by a comparison of vibrational populations for HeI + NO and He*(2 ^3S) + NO up through $v' = 5$. Beyond $v' = 5$ the populations were too small to report. Hotop[73] reported very similar results to Brion [72] for He*(^3S) + NO and HeI + NO, that is, a very close correlation between the PIES and PES results. In a later work[74] Hotop *et al*. reported similar results again, still only listing results up to $v' = 5$. Hotop reports significant differences, however, between NeI + NO and Ne*($^3P_2$) + NO spectra. The most intense peak that he reported for the NO + Ne*($^3P_2$) PIES spectrum was $v' = 2$, whereas the most intense peak for the PES spectrum is the $v' = 1$ peak. We found $v' = 2$ as the maximum, too, for our Ne* + NO spectra. (Likewise, HBr exhibits a change in the tallest peak on going from PES to PIES[75].) The maximum at $v' = 1$ in the PES spectrum agrees with FCfs, as do the relative (to $v' = 1$) populations shown by Hotop [73]. The relative (to $v' = 2$) populations

for the PIES spectrum, however, are double those for the PES spectrum from, at least, $v' = 3$ to v' = 6. [73]

O$_2$: Morgner et al.[76] show results for He*(^1S) and He*(^3S) + O$_2$. These results show non-FC behavior beyond $v' = 5$ for the X state, which is what we find for Ne*. Our Ne* results, though, show larger peaks for the $v' = 6$ to 10 transitions, relative to the FC region, than do the He* spectra. These larger peaks in our Ne* spectrum are evident before the large continuum signal increases substantially, indicating that their greater intensity than found in He* + O$_2$ is not due to the continuum signal. There is a vast difference between the HeI and the NeI PES X state spectrum of O$_2$. The HeI spectrum of O$_2$ generally follows FCfs with essentially no peaks beyond $v' = 4$ or 5[77], in line with Table 4.8. The NeI X state progression is reasonably close to FC behavior up to $v' \approx 3$ or 4, but there are well resolved peaks in our calibration spectrum to at least $v' = 16$. Branton et al. [77] have shown well resolved peaks up to $v' = 21$. In fact, the peak heights from $v' = 5$ to 9 are greater than the largest peak in the FC direct photoionization region ($v' = 0$ to 3 or 4). We are in agreement with Branton et al. [77] that the $v' = 7$ peak is the tallest in the NeI + O$_2$ X state progression.

Our results have shown that all Ne* spectra for the diatomic molecules in this dissertation exhibit non-FC behavior. Only for H$_2$ are the relative FCfs *larger* than some of the relative populations of the PIES spectrum. See Figure 4.4. For all of the other diatomic molecules studied here, there are significant populations in long progressions well beyond that predicted by FCfs. See Figures 4.7, 4.11, 4.17, and 4.21 and Table 4.8. Only for the first few peaks in the spectra do we find FC behavior. Why is FC behavior rarely followed for the molecules that we

tested? As mentioned above, He*($^1S_0$, $^3S_1$) states are more energetic than Ne*($^3P_2$, $^3P_0$) states by at least 3 eV (see Table 1.1), and they also have a different geometric dependence than Ne* collisions due to the occupied *s* vs. *p* orbitals. Since NeI PES uses NeI *photons*, Ne* reactions use Ne* *atoms*, and non-FC behavior is seen in both cases, the key factor must be the lower energy of Ne* (compared to He*), not the geometric dependence. (As mentioned above for CO, geometric differences can affect populations. It is just not the major reason for the appearance of so many non-FC peaks in Ne* spectra as opposed to He* spectra.) The Miller idea of Section 1.2 is worth noting again: Miller describes PI as the "leakage" (i.e., transition) from the discrete state found on the V_0 curve to a state in the continuum that is degenerate with it. (See Figure 1.3.) Apparently, the lower energy of Ne* allows for greater "leakage". To explain and model the non-FC behavior one must consider increases or decreases in coupling $V_{0\varepsilon}(R)$ (i.e., a larger transition matrix element) between V_0 and V_+, changes in Γ, or the possibility that the process we observe is not Penning ionization. To explain the origins of our spectra, we will review the currently proposed mechanisms for reactions involving metastable noble gases. Mentioned in Chapter 1, the first mechanism is the *exchange mechanism* which is responsible for Penning ionization, where a valence electron from the target molecule fills the "hole" in the metastable and the excited electron from the metastable is ejected. The exchange mechanism proceeds through a collision complex [NeX]* where Penning electrons are emitted only during the fleeting existence of the complex. [20] This very often occurs with a nonzero $\Delta\varepsilon_s$. This direct ionization process is responsible for population of the FC peaks in He* and Ne* PIES, as described above in relation to Figure 1.3. This mechanism is also able to generate many additional non-FC peaks in Ne* PIES spectra, peaks that do not appear in He* PIES spectra, because there is a greater density of Rydberg states for Ne* reactions than for He* reactions due to the "softer" (i.e., less

energetic) collisions of Ne* than He*. This increased number of Rydberg states allows for greater "leakage" from V_0 to a state in the continuum above V_+. Generally, a Rydberg state is one in which an electron is in a high n level, but it is not considered to be ionized. In PIES this highly excited electron, from the metastable atom, is the electron that is ejected. The loss of the electron from the Rydberg state is referred to as *autoionization*, and it is accompanied by relaxation into a lower energy state (almost always the X state for Ne* PIES diatomic reactions). A more specific application of this mechanism has been proposed by Dunlavy and Siska[18] to explain the bimodal X state peaks for He*($2\ ^1S_0$) + N_2 that were mentioned above. In their scheme the nearly resonant vibrational levels are those of an excited state of the ion and those of the ground state of the ion. A bit more revealing than Figure 3.10, Figure 5.1 shows that starting around the $v' = 6$ level of the N_2^+ X state curve, the vibrational levels are nearly resonant with the roughly $v' = 1$ and higher vibrational levels of the A state of N_2^+. Thus, in the formation of N_2^+ peaks in the non-FC region they proposed an excited $A\ ^2\Pi_u$ core (or a state very nearly resonant with it) with a Rydberg electron that relaxes into the $X\ ^2\Sigma_g^+$ state. This can be represented schematically as: He* + N_2 → {He···[N_2**]}•e$^-$ → He + N_2^+ + e$^-$. While the transition state in the middle step could be represented as *only* [HeN$_2$]*, the schematic {He···[N_2**]}•e$^-$ is an attempt to describe their proposed mechanism. To adhere to the exchange mechanism, this notation is meant to convey that He* has accepted an electron from N_2, N_2 becomes excited ([N_2**]), and the Rydberg electron (•e$^-$) is the initially excited electron from He*. We used ** on N_2 to show that the excitation on N_2 is *not* the exact excitation possessed by He* initially; the *sum* of the energy of [N_2**] and the energy of the Rydberg electron is equal to the initial excitation of He*. Again, vibronic relaxation with a simultaneous loss of the Rydberg electron produces the final products. Despite the difference in appearance of the transition state, the PIES

spectra obtained for this reaction give information about the nascent ion, N_2^+. The Dunlavy and Siska mechanism is more specific; a generic state in the continuum is replaced by a specific state, the A state of N_2^+. The loss of a Rydberg electron, initially attached to an excited core that decays to a lower energy state, is an important mechanistic concept in PIES. In the He*($2\,^1S_0$) + N_2 spectrum the lack of peaks for the $v' = 3$ to 5 portion of the X state progression and any peaks above $v' = 11$ is due to the lack of resonance of any other levels with the A state curve. This bimodal mechanism requires that the curves for two states cross within the energy available to the system from the metastable. Further, any state above the X state is barely accessible for our Ne* reactions. See Table 1.3 and Figure 3.10. Thus, this mechanism will not apply to any diatomic reaction in this dissertation. (H_2, of course, has only the X state.) If the enhanced populations (above FC predictions) in Table 4.6 for Ne* + NO (a state) are correct, it can not be due to relaxation from the b state to the a state via this bimodal mechanism because these two curves do not cross until roughly the $v' = 6$ level for the a state. This is beyond the excitation energy of Ne*.

A second mechanism that *can* lead to PI is provided by Morgner *et al*. [76] in a paper on the reaction of He* and O_2. They proposed two main avenues for ionization of O_2 for the He* + O_2 reaction. The first is ionization that follows formation of an *ion pair*: $He^+ + O_2^-$. This mechanism is made possible because O_2 has a positive electron affinity (0.450 eV)[78] and an unfilled HOMO and because three out of four of the covalent potential energy curves (He* + O_2) can cross over to the ionic potential energy curve for dissociation to $He^+ + O_2^-$. A Penning process is then possible, forming all possible O_2^+ states, with a significant $\Delta\varepsilon_s$ and a very broad electron energy distribution. Ion pair formation does *not* have to lead to Penning ionization. The

second avenue to ionization proceeds through He*(2 ^3S) + O$_2$ → He + O$_2$* and involves

excitation transfer from He* to O$_2$. The excitation gained by the O$_2$ is *very nearly* equal to that

initially possessed by Ne*. This is followed by the molecular autoionization O$_2$* → O$_2^+$($X\,^2\Pi_g$,

v') + e$^-$. This is not Penning ionization, although the overall reaction certainly looks like it. One

of the key findings to support this was that there was no shift found for the He*(2 ^3S) + O$_2$ → He

+ O$_2^+$ reaction. Morgner [76] points out that, since O$_2$* will have an energy nearly equal to that

of Ne*, no shift is expected; the energy of the ejected electron is expected to be very close to that

based purely on orbital energies (i.e., the nominal energy). Thus, peaks with no shift that are

found in spectra from metastable noble gas reactions are most likely attributable to the excitation

transfer mechanism, and Morgner *et al*. argues that the O$_2^+$ ($X\,^2\Pi_g$) peaks are not PIES peaks.

The other key point that Morgner uses to justify the excitation transfer mechanism is that a PI

(i.e., exchange) mechanism is symmetry forbidden. To be clear, we argued above that non-FC

peaks can originate from the exchange mechanism as long as autoionization of the Rydberg state

occurs *after electron transfer in a Penning fashion* and yields *a non-zero line shift*. Since there is

a Rydberg state, though, there must be 'excitation', but the excitation is not equal to the entire

excitation of the metastable. In the excitation transfer mechanism *there is no electron transfer*

from the metastable to the target. Thus, it is *not* Penning ionization, and the transfer of

excitation is total or nearly so. Morgner argues that the excitation transfer mechanism occurs

most effectively into a state which has an energy as close as possible to the excitation energy of

the metastable. Like the non-FC exchange mechanism, though, there is autoionization of a

Rydberg state, and competition between these two mechanisms is clearly possible in some cases.

Yee *et al*. [68] note that this competition between the excitation transfer mechanism and Penning

ionization leads to spectra where "the shape of the envelopes will be different since the

[competing] transitions occur between two different sets of potential surfaces with different transition probabilities".

Based on this overview of mechanisms above, we will propose mechanisms for our diatomic reactions. It is important to note the following before we do. We have *not* determined the *final* products for the reactions in this dissertation. We have not considered (see Section 1.1) the possibility of associative, dissociative, or rearrangement ionization. The DI and RI channels comprise the post-ionization dynamics, and, since this happens after the electron leaves the [ABC]* complex, we can not know about it in the instrument used for this dissertation. Thus, if there are no other mechanisms (e.g., excitation transfer or ion pair) occurring, the complex [ABC]* will either undergo Penning ionization or associative ionization. AI occurs when the departing electron leaves with sufficient kinetic energy as to keep ABC^+ intact in one of several rovibrational states. Despite this, the ejected electrons provide information on the **nascent ion** *formed from the* **target molecule**. A simple justification for this is to consider the following: In terms of vibrational spacing and position (within a small line shift), the progressions are nearly what one gets from PES of the targets if we include FC and non-FC peaks together. These detected electrons *must* be providing information on ions of the target molecules. While information on Ne* reactions (e.g., branching ratios, etc) still remains scarce to this day, there has been some done to determine products. At $E = 0.02 - 0.4$ eV Appolloni *et al.*[79] report that the formation of X^+ (X = N_2, O_2, CO, and NO) was the dominant process for Ne* + X. Associative ionization, which forms NeX^+, was a very minor (7 %) product. Bussert *et al.* [59] similarly report that H_2^+ is the dominant channel for Ne* + H_2, with roughly 80 % of the product being H_2^+. With this in mind, we propose mechanisms below.
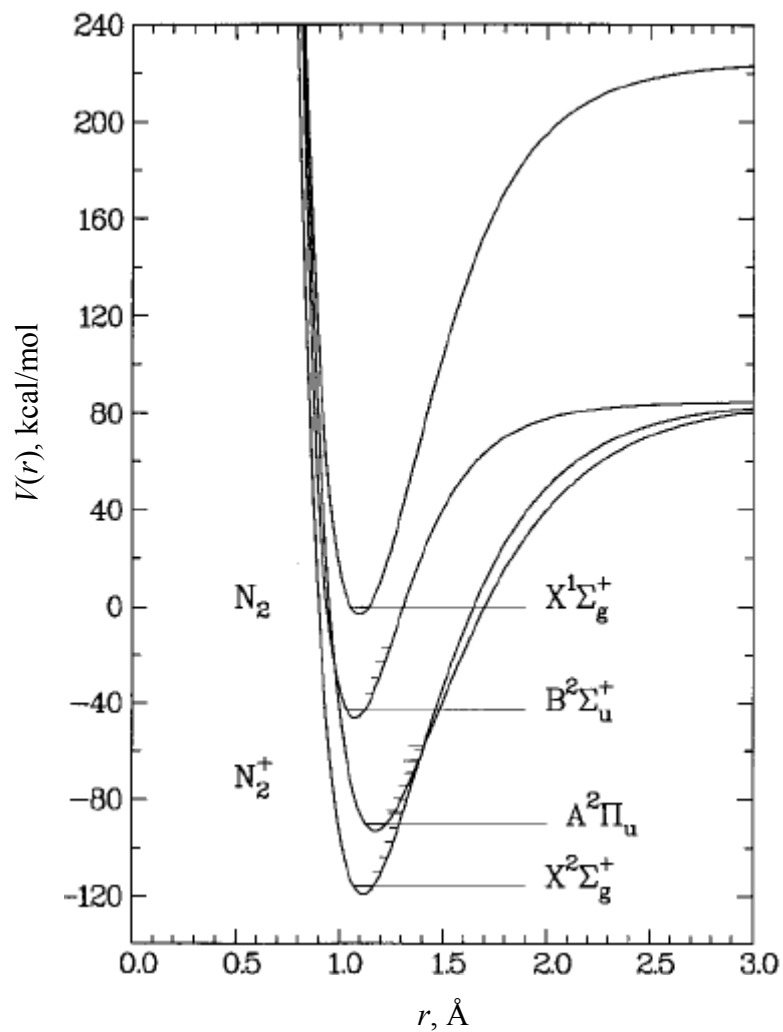
Figure 5.1: Energetics of the He*(2 ^1S) + N_2 Penning ionization reaction illustrated with N_2 and N_2^+ potential curves. The N_2^+ curves have been lowered in energy by the excitation energy of He*(2 ^1S), 20.616 eV (475.42 kcal/mol). The tic marks on the curves denote vibrational levels. Note the nonavoided crossing of the X and A curves on their outer limbs. (Reproduced from Reference 18, Dunlavy and Siska.)

H_2 has no measurable electron affinity.[80,81] The minimum in the potential energy curve of $H + H^-$ is merely a metastable state in the continuum of H_2 plus a scattered electron. CO and N_2 have electron affinities of -1.5, and -1.90 eV, respectively. [26] H_2, CO, and N_2 are all closed shell molecules. These facts essentially rule out the ion pair mechanism for their reactions. The fact that all three exhibited a sizable $\Delta\varepsilon_s$ eliminates the excitation transfer mechanism. This leaves the exchange mechanism as the only choice. Further, as E was increased, the peaks for all three molecules became broader and the line shift for each increased. This is the expected behavior for ionization from a repulsive, excited state potential energy surface. Thus, the FC peaks in the H_2, CO, and N_2 peaks are due to direct Penning ionization, and the non-FC peaks are the result of autoionizing Rydberg states. Bussert *et al*. [59] proposed that Ne* + H_2 proceeds via a (Penning) exchange mechanism. We explore H_2 further below, given its lower than FC populations. As noted in Section 4.2, Lescop *et al*. [13] reported no PIES shift for Ne* + CO. Our results are *very* different. They proposed that a "quasi-resonant excitation transfer process" leads to an intermediate autoionizing Rydberg state for excited CO. From their work, it appears that they do not think this reaction follows a Penning mechanism. We propose that the FC and non-FC peaks are the result of the exchange mechanism. The sizeable shift that we observed rules out the excitation transfer mechanism, as we have defined it here. Lescop *et al*. proposed [12] for Ne* + N_2 that a "resonant excitation transfer between the colliding particles" leads to an intermediate autoionizing Rydberg state for excited N_2.

Proposing a mechanism for NO is difficult without further information. The ion pair mechanism is possible given that it is open shell, but NO has a small electron affinity (0.026 eV)[82]. Appolloni *et al*. [79] propose that a Coulombic attraction, perhaps an ion pair, is possible

for Ne* + NO. This ion pair attraction for Ne* + NO, along with an autoionization process, is also proposed by Aguilar et al.. [14] The line shift is quite small for the $NO^+(X)$ state, however, and an ion pair mechanism is expected to give a sizeable line shift. Likewise, this small shift makes it difficult to choose between the exchange or excitation transfer mechanism. To explain the extensive $NO^+(X)$ progression, however, it seems logical to propose the involvement of an autoionizing Rydberg state that converges to the b state of NO^+. The a state line shift is significant, and its nearly 40 or more meV difference from the X state shift argues for an ion pair or exchange mechanism. Note that it is possible to have different mechanisms at work in different parts of the same spectrum for a reaction. Morgner et al. [76] propose just that for He* + O_2.

Given the very small line shift for O_2, we propose that excitation transfer is the mechanism by which Ne* + O_2 proceeds to form $O_2^+(X\,^2\Pi_g)$. This is the mechanism that Morgner [76] invokes for He*(^3S) + O_2. Appolloni et al. [79] propose that an ion pair is possible for Ne* + O_2 and Ne* + NO, but they acknowledge that there is a large number of possible adiabatic states for Ne* + O_2, making an exact description difficult. Note that the Appolloni paper [79] is on collision cross sections, and the ion-pair mechanism suggestion is not specific to a particular set of peaks in a Ne* + O_2 or Ne* + NO electron kinetic energy spectrum. Our suggestion for the excitation transfer mechanism is specific to the $O_2^+(X\,^2\Pi_g)$ peaks. Despite the excitation transfer mechanism that Morgner [76] invokes to explain the $O_2^+(X\,^2\Pi_g)$ formed from the He*(^3S) + O_2 reaction, he points out that it is surprising that the vibrational populations look very similar to those predicted by FCfs, which is what one expects from a Penning process. This effect appears to be at work for Ne*, too, for the peaks from $v' = 0$ to 3 or 4. See Table 4.8 and

Figure 4.21. The similarity at low v' is attributed to a very short lifetime for O_2*, allowing for nearly equal momentum distribution for the nuclear motion in the ground state of O_2 and the excited state, O_2*. In forming $O_2^+(X\,^2\Pi_g)$ from the reaction He* + O_2 Morgner proposes that all of the peaks are originate *not* from the O_2 ground state but from an excited state O_2*, which converges to the B state. Note (Tables 1.1 and 1.3) He*(^3S) = 19.8196 eV and *IE* for the O_2 B $^2\Sigma_g^-$ state is 20.350 eV[83]. Since Ne*($^3P_2$) = 16.6193 eV and Ne*($^3P_0$) = 16.7156 eV, we propose a similar route for Ne* + O_2, but one that runs through the O_2^+ $A\,^2\Pi_u$ state, the *IE* of which is 17.045 eV.

We acknowledge that the above has been somewhat qualitative, but much of this field is just that. When we or Lescop argue that the non-FC portion of the PIES spectrum for N_2 is due to "autoionizing Rydberg states", it does beg the question: *Which* Rydberg state? Rydberg states are still being investigated (e.g., N_2 and NO)[84,85], and they lead to complex spectra. In the case of N_2, for example, there are three Rydberg series that converge to the $A\,^2\Pi_u$ state of N_2^+. Deciding which series, however, is no simple matter since all three series appear in the same energy region of the spectrum (~122 000 to 132 000 cm^{-1}), as Lefebvre-Brion and Yoshino show.[86] In the case of CO, investigation of the W Rydberg state, which converges to the $A\,^2\Pi$ core, is hampered by predissociation[87,88,89]. Thus, proper descriptions of the coupling to such states are difficult. Further exploration of this is obviously desired.

The line shift for the lowest three Es of CO_2 remained constant, and $\Delta\varepsilon_s$ is small. This supports the excitation transfer mechanism since the energies of the orbitals do not change, of course, if E does (if no perturbation occurs). The sudden change to a blue shift at the highest E

suggests that a competing exchange mechanism becomes dominant since the collision occurs higher up on the repulsive part of the potential energy well. The broader peak with a relative blue shift further supports this proposal, as well. As mentioned above, Figure 4.22 indicates that the first four peaks in the Ne* + CO_2 progression can be assigned solely to the nv_1 progression. Before we discuss the CO_2 populations, though, a few comments on the FCfs in Tables 4.9 and 4.10 are in order. The calculation of FCfs for polyatomic molecules can mostly be traced back to the paper by Sharp and Rosenstock. [63] Work continues in this area in the papers cited in Section 3.2, and corrections and revisions have been performed by Weber and Hohlneicher[90]. For the X state we find that the relative calculated FCfs for CO_2 are 1, 0.122, and 0.019. [63] These have been measured from a figure that they provide. Citing Sharp and Rosenstock [63], Brundle and Turner[91] report nearly identical FCfs, verifying our use of the figure. We can obtain experimental FCfs for C_2H_2 by using HeI PES, assuming that FC behavior is observed for the X state. The results of Parr *et al*. [66] give 1, 0.42, 0.12, and 0.02. Our HeI PES results agree well with these ratios. Lescop *et al*. [10] reported relative FCfs of 1, 0.30, 0.13, and 0.01, citing Parr *et al*. [66]. In email correspondence with B. Lescop, he attributed the 0.30 to an error.

The comparison of the CO_2^+ population data that was made in Table 4.9 shows that FC behavior is not observed. There is enhanced population well above the FCf prediction as early in the progression as $n = 1$. For the region above $\varepsilon = 1.5$ eV, Lescop *et al*. [7] propose that CO_2 ionization is the result of excitation transfer that leads to an autoionizing Rydberg state that converges to the CO_2^+ A state. Our results argue for this even more strongly since our fit suggests that only the nv_1 progression is responsible for the peaks. This enhanced intensity for the single progression must be due to autoionization, not excitation of other vibrational modes or

combination modes. Part of their argument for this region of the spectrum, though, relies on the assignment of which vibrational progressions are present. As yet, we are unwilling to accept their progressions, and those of Cermak, until we perform the fit more completely ourselves. For the region between 0.5 and 1.5 eV, Lescop et al. [7] propose that is the result of an ion pair mechanism that opens during the collision. This, likewise, is a proposal that can't be confirmed nor denied until CO_2 is studied more fully by our group.

In Table 4.10 the X state populations of C_2H_2 show remarkable agreement with the FCfs. Similar results for a single E for Hotop and Niehaus[92] led them to propose that for C_2H_2 the exchange mechanism with direct transitions (i.e., no autoionizing states) is observed. Note that the sizable shifts argue against the excitation transfer mechanism, and the -1.7 eV[93] EA of the closed shell C_2H_2 argues strongly against the ion pair mechanism. In the intervening years between Hotop's proposed mechanism and today, Lescop et al. [10] proposed that the exchange mechanism competes with an excitation transfer mechanism, including autoionization. Citing Aguilar et al. [14], Lescop et al. [10] note the relatively flat ionization cross section behavior for Ne* + C_2H_2. If ionization depends on orbital overlap, as the exchange mechanism does, one expects the ionization cross section to increase as E increases. Likewise, as mentioned at the end of Section 4.8, as E increases, "normal" PI predicts that blue shifts become more blue. We did not find that, but our C_2H_2 results did show two runs with identical (within error) line shifts. This would argue against the exchange mechanism in the same way mentioned above for the first three Es of CO_2. Yet, the substantial decrease in line shift between the first two Es can't be ignored. An explanation for the results found here, then, is that the exchange mechanism is dominant at low E, but that an excitation transfer mechanism opens up as E increases. The only

problem with this is that, if we try to meld the results of both groups, the result for Lescop *et al.* [10] was for a run at $E \approx 1.3$ kcal/mol. Our proposal puts forth the exchange mechanism at this E. This competing mechanism idea, however, is possibly the key to explaining the results of NO, CO_2, and C_2H_2, which are so vastly different than the traditional results seen for PI. Theoretically, it is more complex, but it is full of (funded, perhaps) research potential. A final note of caution about the constant line shifts that were found for CO_2 and C_2H_2 and their relation to the proposed mechanisms must be noted. From Bevsek [4] and Siska [5], a more slowly varying region in V_0 is able to explain a leveling off of the shift values, as found with He* + CO [4]. The values for Ne* + CO_2 and Ne* + C_2H_2, however, were the same within error – not slowly changing. They didn't "level off". Thus, the mechanism proposals for CO_2 and C_2H_2 assume a "typical" V_0 with no kinks. [5]

Above we have argued that the populations of the non-FC region for CO, N_2, NO, and O_2 can be explained by relaxation of autoionizing Rydberg states into the ground states of the molecular ion, made possible by the larger number of states, compared to He*, that are in resonance with the continuum of states above V_+. (The process of electronic relaxation of Rydberg states with an excited ionic core is not possible for H_2, of course, since there is only one state of the ion.) For H_2, however, there is a problem. Figure 4.4 shows that the populations for the $v' = 3$ and 4 peaks are *lower* than the FCf prediction. This is a troublesome result because the concepts and explanations of Miller [34], applied to molecules, rely on the idea that the Penning transition is analogous to an optical transition, where it is expected that the overlap between the incoming neutral vibrational wave function $|v\rangle$ and the range of possible cation wave functions $|v'\rangle$, that is, the FCfs $q_{vv'} = |\langle v|v'\rangle|^2$, will be a significant factor in determining the form of the

distribution. Because the Penning transition is induced by a collision, however, a more comprehensive theory would incorporate the extent to which the oscillators in the reagent and product states are distorted by the collision.[94] Any distortion would be reflected in alterations in the FCfs and in the *observed* populations. In 1995 Bevsek and Siska [94] developed a theory to predict PIES spectra. This model and its extension to Ne* + H_2 in Reference 20 are outlined below. Note, however, a very important idea: Since all of the other diatomic data exhibited non-FC behavior that *added* to the observed intensity and/or progressions, there is no way to tell whether these other diatomics actually exhibit the same lowered intensity from FC transitions. Perhaps, they do, but this fact is obscured by the competing autoionization process. Thus, the goal of the Bevsek and Siska model is to describe kinetic energy distributions for PIES for the cases where an autoionization process is not competing. In Reference 20 this model is used to calculate line shape and line shifts and explore the possibility of the dependence of $\Delta\varepsilon_s$ on v' due to bond stretching at higher vibrational levels.

To develop a theoretical framework for treating vibrational population distributions $P(v')$ of the molecular Penning ion in the transition region ("nascent" populations) [93], Bevsek and Siska proposed a vibrationally adiabatic model for molecular Penning ionization, in which the distribution of vibronic populations in various product states is decoupled from the dynamically determined line shape characterizing an individual vibronic line [20]. By vibrationally adiabatic they meant that the vibrations of the reagent molecule and its cationic product are relatively undisturbed by the ionizing collision [18]. In this model, the vibronic intensity distribution is a reflection of Franck-Condon behavior, modulated by the bond length (r) dependence of the

discrete-continuum coupling $V_{0\varepsilon}(r,R)$, an off-diagonal matrix element of the electrostatic

Hamiltonian. If $V_{0\varepsilon}$ is expanded as

$$V_{0\varepsilon}(r,R) = V_{0\varepsilon}[1 + a_1(r - r_e) + a_2(r - r_e)^2 + \cdots] \tag{4}$$

they obtained

$$\frac{P(\upsilon')}{q_{\upsilon'0}} = |1 + f_{\upsilon'0}|^2 , \tag{5}$$

where $q_{\upsilon'0}$ is a FCf for the diatomic molecule, and $f_{\upsilon'0}$ is the adiabatic correction term of the

form

$$f_{\upsilon'0} = a_1 \frac{\langle \upsilon'|r - r_e|0 \rangle}{\langle \upsilon'|0 \rangle} + a_2 \frac{\langle \upsilon'|(r - r_e)^2|0 \rangle}{\langle \upsilon'|0 \rangle} + \cdots \tag{6}$$

In Equation 6 r_e refers to the neutral molecule. Further, the theory relies on the work of

Miller [34], particularly the S matrix, to incorporate $V_{0\varepsilon}$. In the quantum mechanical formulation,

Miller expressed S as [94]:

$$S^l_{\varepsilon 0} = -2i(2\mu_c/\hbar^2)\exp(i\eta_{l0} + i\eta_{l\varepsilon}) \times \langle u_{l0}(R)|V_{0\varepsilon}(R)|u_{l\varepsilon}(R)\rangle , \tag{7}$$

where the subscript 0 refers to the initial state, heavy-particle motion on the complex (optical) potential $V_0(R) - i\Gamma(R)/2$ with kinetic energy E; subscript ε refers to the electron kinetic energy in the final state, heavy-particle motion on the potential $V_+(R)$ with kinetic energy $E' = E + \varepsilon_0 - \varepsilon$; l is the collisional angular momentum quantum number; μ_c is the collisional reduced mass; $\eta_{l0}(\eta_{l\varepsilon})$ is a heavy-particle radial phase shift for the initial (final) state; and $u_{l0}(u_{le})$ is the corresponding 1D radial wave function. $V_{0\varepsilon}$ is the discrete-continuum coupling electronic matrix element, described in Chapters 1 and 2 and given in Equation 4 in an expanded format,

$$V_{0\varepsilon} = \int dr_{\mathrm{el}} \Phi_0(r_{\mathrm{el}}; R)[H_{\mathrm{el}} - E_{\mathrm{el}}]\Phi_\varepsilon(r_{\mathrm{el}}; R) = \langle \Phi_0 | H_{\mathrm{el}} - E_{\mathrm{el}} | \Phi_\varepsilon \rangle, \tag{8}$$

where r_{el} represents all electron coordinates, Φ_0 is the quasidiscrete (resonance) electronic wave function for the initial state, Φ_ε is the continuum electronic wave function describing an ionic bound state plus a free electron, and H_{el} and E_{el} are the electronic Hamiltonian and energy. The phase is included in Equation 7 because transitions on the incoming and outgoing part of the trajectory (of the collision) have a different phases associated with them. The equations for the phase are found in the Miller paper [37]. As done in Reference 20, to include vibration of the molecular target, we modify the matrix element of Equation 7 as follows:

$$S_{\varepsilon 0}^l(\varepsilon) = -2i(2\mu_c / \hbar^2)\exp(i\eta_{l0} + i\eta_{l\varepsilon}) \times \langle u_{l0}(R) | \langle \chi_\upsilon(r; R) | V_{0\varepsilon}(R) | \chi_{\upsilon'}(r; R) \rangle u_{l\varepsilon}(R) \rangle, \tag{9}$$

where the χs are vibrational wave functions [18]. Ultimately, the best line shapes and line shifts for Ne* + H$_2$ were determined from the spherical potential, which yields the Penning line (i.e., peak) shape given by [18]:

$$P(\varepsilon) = \frac{\pi}{k^2} \sum_{l}^{\infty} (2l+1) \left| S_{\varepsilon 0}^{l}(\varepsilon) \right|^2 . \tag{10}$$

Note that $k^2 = 2\mu E/\hbar^2$. Evaluation of $S_{\varepsilon 0}^{l}(\varepsilon)$ is no easy matter. The process begins by determining V_0 and V_+, the potential energy curves for the entrance and exit channels. Both curves were approximated by Na + H_2, where Na is a stand-in for Ne*, given its $3s$ electron. These calculations[95] yield *ab initio* points along both potential surfaces, which are fit to functional forms convenient for numerical solution of the radial Schrödinger equations governing the motion on V_0 and V_+. [20]   (From Equation 9 the 1D radial wave functions that we need are u_{l0} and u_{le}.) The "functional forms" are the potential energy surfaces proposed[96] by Tang and Toennies(TT) or those TT potential energy functions that have been modified by the group[97,98,99]. The exact forms of V_0 and V_+ are given in Reference 20. The form of Γ was chosen to be a simple exponential: $\Gamma(R) = \Gamma_0 \exp(-\alpha R)$. Recall that Γ is buried in S by its relation to $V_{0\varepsilon}$, shown above. More elaborate functions for $\Gamma(R)$ have been used in the past for He* + N_2. [18] To establish values for the parameters Γ_0 and α, we varied them in a nonlinear least squares procedure to fit simultaneously the quenching rate constant[100] k_q for Ne*($^3P_2$) + H_2 and the state-averaged E dependence of the total ionization cross section Q_I.[101] Fortunately, References 100 and 101 contain k_q and Q_I data for N_2 and CO, allowing us to repeat this process for N_2 and CO in future work. The results of the potential energy function calculations are shown in Figure 5.2.

The potential energy surfaces shown in Figure 5.2 are used to obtain radial functions numerically to solve the S matrix equation, which allows us to solve Equation 10. The $P(\varepsilon)$ functions give the line shape and line shift of the spectral peaks, not the populations. The theory

handles the populations by weighting the peaks by FCfs. Figure 5.3 shows the line shapes and

shifts for the four energies that were studied for Ne* + H_2. Note that the peaks shift to higher

energy and get broader as E increases. Figure 5.4 compares the theoretical results to the

observed spectra, where the line shapes of Figure 5.3 are used repeatedly, weighted by FCfs, to

build up the overlapped spectra. It is apparent in Figure 5.4 that the theory predicts narrower,

more blueshifted lines than found experimentally. [20]
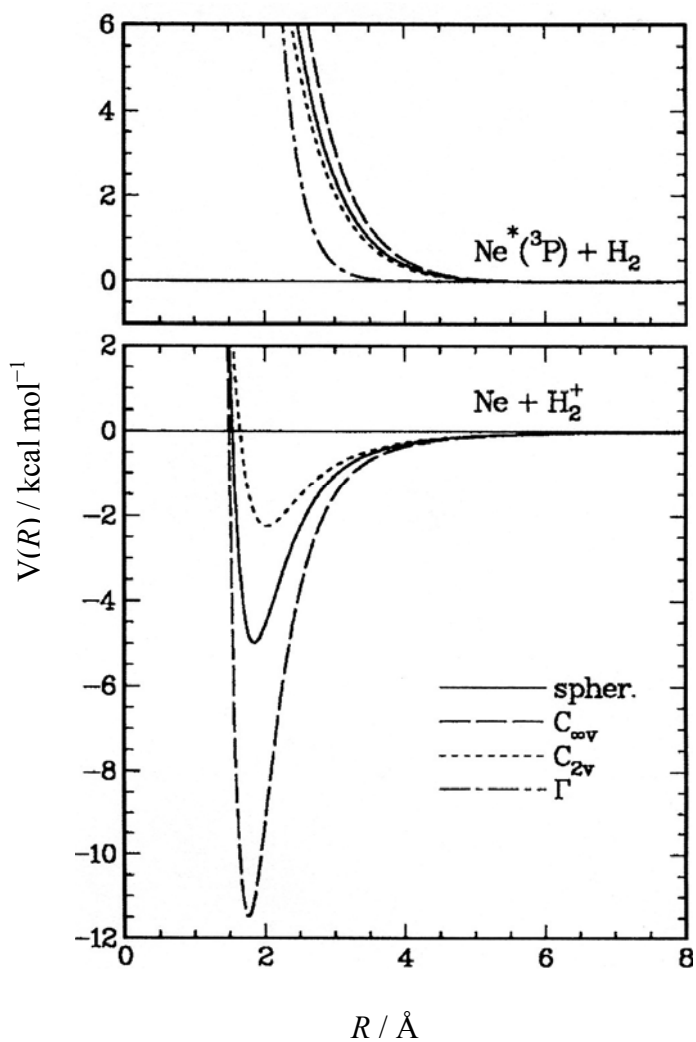
Figure 5.2: Potential-energy functions from Tang-Toennies potential energy functions, adjusted to fit ab initio calculations, or experimental data (in the case of Γ). The energy difference between the asymptotes of the upper and lower panels is 29.741 kcal/mol for Ne*($^3P_0$) and 27.520 for $^3P_2$. [Reproduced from Reference 20.]
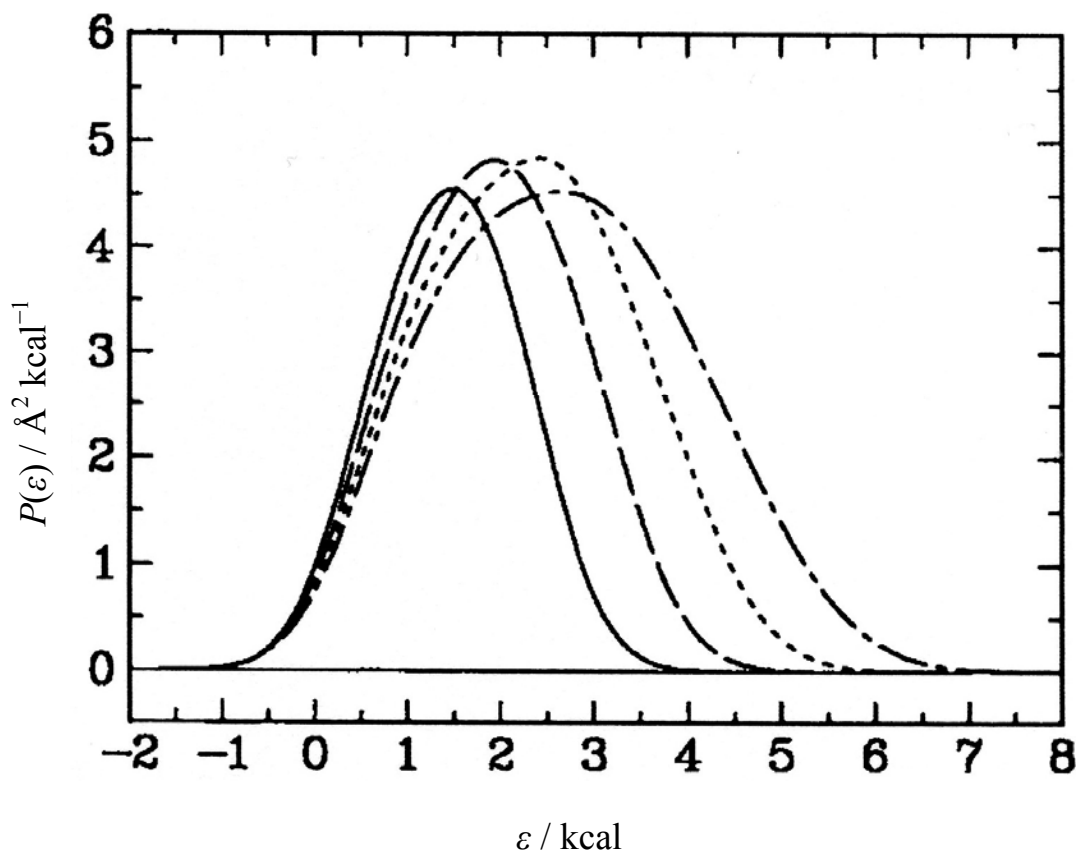
Figure 5.3: $P(\varepsilon)$ curves at the four collision energies for Ne* + H_2. These are based on a spherical potential. The curves broaden and shift to higher electron energy as E increases. [Reproduced from Reference 20.]

Thus, Figure 5.4 is the culmination of kinetic energy studies of PIES. The experimental line shifts and shapes that we obtain in our spectra are "correct". It is our job to find a theory that correctly models the potential surfaces that give rise to the spectra. We know how well we did by how well our theoretical results match the observed spectra. In addition to the theoretical peak shapes being too narrow and more blueshifted than observed, the populations are not well represented by the FCfs. This same population problem was seen for the A state of N_2^+ in the reaction of He* + N_2. [18] This is not unexpected because the theory makes no attempt to determine populations, but this raises a significant issue. In this dissertation the observed Ne* PIES spectra obeyed FC behavior only for the X state of $C_2H_2^+$. The extensive difference between the relative FCfs and the relative populations for the Ne* spectra of all of the other target molecules might prohibit extending this theory to Ne* reactions in general. At a minimum, it will only be able to model a small potion of the observed spectrum. Consider, for example, that the large majority of peaks observed in the Ne* + CO spectrum are non-FC. The greatest concern, though, for the application of this theory to Ne* PIES reactions in general is the primary assumption: the vibrations of the reagent molecule and its cationic product are relatively undisturbed by the ionizing collision. If the lower energies involved in Ne* reactions and the greater number of resonant states create larger than expected perturbations, then the theory will need adjusting. Note, though, that the theory was made *tractable* in the first place *because* of the assumption just stated. Perhaps, greater than expected perturbation of the vibrational wave functions is the cause of the *lower* (within an unperturbed FC framework) than expected populations for the $v' = 3$ and 4 in the Ne* + H_2 spectrum. Still, Bevsek [4] points out that, if collisional perturbation does occur, one would expect $P(v')$ distributions to become increasingly non-FC with increasing E. For the FC portions of the observed Ne* spectra, this was not

145

observed. The populations and peak shapes did not undergo drastic changes as E increased. Due to the vast differences between He* and Ne* PIES spectra, further work must be done to determine how applicable this theory will be to Ne* PIES reactions.
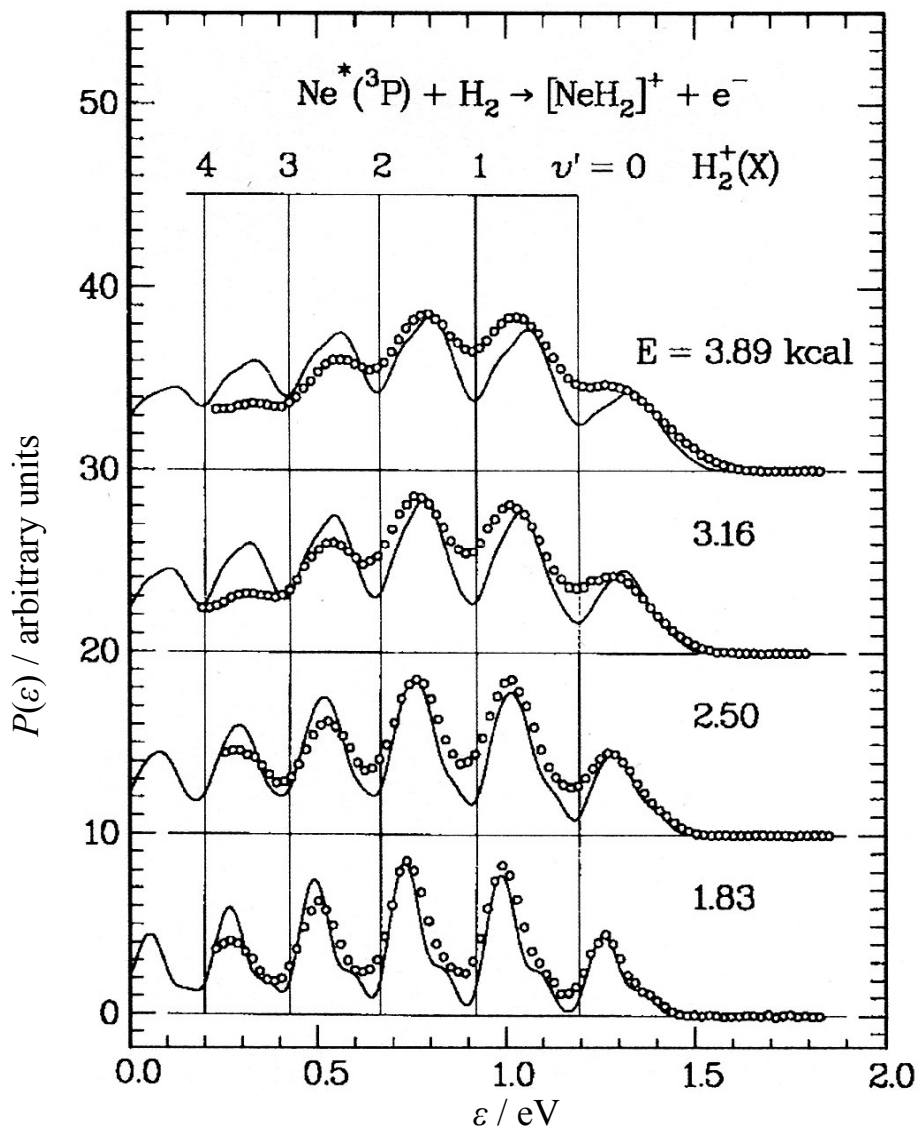
Figure 5.4: Simulated spectra (lines) based on the line shapes of Figure 5.3, weighted with Franck-Condon factors, compared to experiment (circles) at four collision energies *E*. [Reproduced from Reference 20.]

6.0 WRITING TEXTBOOK SUPPLEMENTS

A "student solutions manual" must be provided with nearly all new textbooks; publishers require it. It is a legitimate concern that providing complete solutions does not help a student to learn, but, as instructors of chemistry, we can only suggest to those students who obtain a solutions manual that they not look at the solution until a serious effort has been made to attempt to solve the problem. Despite this possible drawback, a textbook supplement can be a way to present subject matter in an alternative format. As coauthor of a student solutions manual for *University Chemistry*, an advanced freshman chemistry book by Peter E. Siska, I was given the opportunity to write solutions to problems, of course, but, additionally, I presented introductions to each chapter's solutions to assist student learning. This chapter is comprised of examples of these efforts.

A common strategy in education is to appeal to a student's prior knowledge. This provides the student with confidence, by allowing them to refine and extend the material that they have seen previously, not replace it. Freshman chemistry students who previously have taken chemistry courses are certain to have learned about valence electrons and electron configurations. Appealing to this knowledge was done to provide the student with a basis for understanding what chemists mean by an "orbital" and a "wave function", as shown below:

In the introduction to Chapter 3 in this manual, we said that quantum mechanics explained the order of the Periodic Table. We say this because confined waves, which are described by quantum mechanics, are what we call orbitals. By assuming that all electrons in atoms occupy similar orbitals ($1s$, $2s$, $2p$,…) with the same general shapes and nodal structure and that each electron has an intrinsic spin, all of the atoms that react readily with water line up (Group IA), all of the nonmetal atoms that typically form -1 ions line up (Group VIIA), all of the atoms that essentially do not react line up (Group VIIIA), etc. You already knew these groups lined up. Further, it is likely that you would attribute this to the identical valence electron configuration in each group. (A more than valid answer, by the way.) *Now you should have a much deeper understanding that these electron configurations consist of products of orbitals that are the result of the wave properties of electrons (or are the waves themselves) and that a mathematical device called a many electron wave function is used to obtain as much information as we can from these orbitals*. While you might not yet understand all of the math or the philosophical implications (few, if any, do), your list of "descriptors" for atomic behavior has grown in a fundamental way.

Further appealing to prior knowledge was done in regards to hybridization of atomic orbitals. Just as with orbitals, beginning students do not consider the "truth" of hybridized orbitals. A good high school student will explain that carbon must be sp^3 hybridized to account for the four bonds that it makes. College chemistry teachers, however, must reveal more of the truth about the subject. To this end, the following was included about hybridized orbitals:

Atomic hybridization is not a verifiable fact. It is a scheme that chemists have devised in response to the knowledge that has been gained about the actual shape of molecules and can be used, for example, to predict the outcome of an untried reaction or to guide the design of drugs…We invoke hybridization only when it is needed, a sure sign that it is not a general explanation. …at times it seems that some chemists rely too heavily on the picture that hybridization gives us *with misleading results*. The rabbit ears representation of the lone pairs on water or the articulated lone pair lobe on NH_3 are picturesque; they

are not, however, true. Their inclusion is to remind you that sp^3 hybridization is being used to rationalize the bonding in these two molecules. Also, they provide conceptually convenient places to start a mechanism, if, for example, water should decide to act as a Lewis base and donate an electron pair.

Another example of building on the students' prior knowledge was made possible through the discussion of Lewis structures. Having taught in high school and having observed freshman chemistry students in college, it is apparent that some high school chemistry teachers require students to differentiate where electrons originate in Lewis structures. For example, in the case of water the electrons from hydrogen can be drawn as ×'s, whereas the electrons from oxygen can be drawn as •'s. This matter was dealt with as follows:

> Some students might be troubled by differences between the [Lewis] structures that we present in *University Chemistry* and those that have been seen in other introductory courses. First, we treat all valence electrons as equals in the compound and do *not* use different symbols (for example, ×'s or •'s) to keep track of which electrons come from which atom. The electrons certainly lose track of where they originate, and the Lewis structure should reflect that.

Due, perhaps, to the physical chemistry leanings of Peter Siska and myself, we find such a practice to be particularly damaging to chemical education and, worse, simply wrong. Electrons can not be tagged; their willingness to spend time on different nuclei is of *fundamental significance* to the formation of covalent bonds. The larger "box", a la the particle in a box, for the electrons in a molecule, as opposed to their more confined atomic orbitals, lowers the total energy of the system, providing motivation for bond formation. In more advanced treatments, of course, the exchange integral is a quantitative measure of "sharing" and a result of indistinguishable electrons. The three examples above illustrate attempts to aid the students in

developing awareness to the fact that the basic concepts that they learned previously are actually

derived from much more rigorous definitions and concepts. This is a process that students must

undergo to learn and excel in chemistry.

A second strategy employed to assist student learning was to present brief summations of

material in the text that is new for nearly all freshman chemistry students, honors or otherwise.

Additionally, the summations were designed to relate seemingly disparate material from different

chapters. The first such example is the topic of distribution functions. In the quotations below,

brief descriptors in brackets follow the relevant portions:

> In introductory courses you often find a plot such as Figure 9.12 [a Maxwell-Boltzmann
> velocity distribution plot] and the "take home" message that molecular speeds increase as
> the temperature increases. Chapter 9 gives you a bit more of the truth by providing
> mathematical details and equations for the three velocities of note, which also indicate
> that at the same T more massive gases move more slowly. Equation 9.46 [the Maxwell-
> Boltzmann velocity distribution equation] provides us the opportunity to revisit the
> concept of a distribution function, which we saw in Chapter 3 with distribution functions
> for the electron. It takes some thought, but the "cloud" [whose density is proportional to
> orbital amplitude] of Figure 3.3(d) is *identical* in appearance for both the location of an
> electron in hydrogen and the particular velocities of a gas sample. The only difference is
> that the axes in Figure 3.3(d) are spatial coordinates (x, y, z), whereas the axes for the
> velocity distribution are the components of the velocities. This is the essence of Figure
> 9.6 [a figure detailing coordinate space to velocity space transformation], which is a
> difficult figure for many to grasp. It may prove to be helpful if you compare the volumes
> of the spherical shells that are shown in Figure 9.6(b) and Figure 3.8 [spherical shell used
> to form radial distribution functions]: $4\pi v^2 dv$ and $4\pi r^2 dr$, respectively. These differ only
> in the variable. The mathematical construct is the same. Further, note how Equation
> 9.47 [the most probable velocity] is derived; we find the maximum of $f(v)$ by setting df/dv
> equal to zero. This is mathematically *exactly* what we did in Exercise 17 of Chapter 3 to

find the most likely points in space for a $2p_z$ electron. The only difference there is that the derivative was taken with respect to r, not v. Thus, the important science/math point is that distribution functions appear in many places in science, but the math and meaning behind them are the same in all cases. This topic is explored in Exercise 37, where we convert from a velocity distribution to an energy distribution.

A second example of a brief summation of material from several chapters pertains to degrees of freedom, a subject of great importance to spectroscopists and physical chemists, especially those engaged in statistical mechanics. This topic is certainly new to freshman, and I tried to clarify the matter with the following:

Exercises 43 through 51 [of Chapter 10] return us to the degree of freedom concerns that were mentioned in the introduction of the Chapter 8 solutions, and here they are used to determine the heat capacities of gases. Now, classical physics did have it partially correct. Molecules do store energy in their various degrees of freedom, and those in which they can store energy are the translational, rotational, and vibrational degrees of freedom. For the record, we note that there are also electronic and nuclear degrees of freedom, but as in Chapter 8 we will not deal with them at this time, except to say that their contribution to the heat capacity is very small. Classical physics, however, did not recognize that the various degrees of freedom are subject to quantization restraints. What complicates the matter further is that the spacing between energy levels is different for translational, rotational, and vibrational degrees of freedom. As discussed in Chapter 8 in the text and in the introduction in this manual, the spacing is smallest for translational energy levels and largest for vibrational levels. It turns out that at room temperature the spacing is small enough in translation that these quantum levels form a continuum. In line with the Bohr Correspondence Principle, the quantum numbers for the translational energy levels that are occupied at room temperature are on the order of 10^{10}. For this reason the kinetic molecular theory yields a *correct* "quantum number free" formula for the translational, that is, kinetic, energy of a monatomic gas, Equation 9.33 or 9.35 [$E = \frac{3}{2}nRT$]. The rotational levels are farther apart, requiring a formula with quantum

numbers, as in Equation 8.11 $[\varepsilon_j = [h^2 j(j + 1)/8\pi^2 I]$. Likewise for vibration in Equation 8.25 $[\varepsilon_v = hv(v + 1)]$. Still, the rotational levels are close enough that thermal energy is sufficient to populate enough excited energy levels to allow for the classical predictions regarding heat capacity to be correct. This is not true for the vibrational levels. The N_2 example in Section 10.7 shows that thermal energy is *not* sufficient to excite even the first excited vibrational state, $v = 1$. (Compare this to the $n \approx 10^{10}$ state for translation.) Therefore, no energy can be stored in the vibrational degrees of freedom. The only energy that is present in vibration is the zero point energy. (From the above, do not think that an H_2 molecule does not vibrate at room temperature. It most certainly does – in its ground vibrational state.)

A third example of a brief summation designed to incorporate previous topics covered in the text is encountered in the chapter on nuclear chemistry. The strategy was to remind the student that the idea of a confined particle applies to more than just an electron. This was done, with a pensive conclusion, as follows:

Nuclear chemistry or processes have not been observed, wittingly or not, for the vast majority of human history because the energies are so difficult to release, yet so monstrous. It is a new force, the strong force, that harnesses this stored energy by "turning on" at short distances, thereby keeping nuclei together despite the *very* close proximity of protons. As indicated by Equation 16.1, the nucleus is extremely small. Since the nucleus is still, of course, subject to quantum effects, we can apply the Particle in a Box model to nuclear distances (*a* in Equation B.8) to show that the energy level spacing is very large (see Exercise 2) – *much* larger than the energy spacing between electronic energy levels and larger still than the spacing between rotational and vibrational levels. Equation 16.2 $[\Delta E = (931.5 \text{ MeV/amu})\Delta m]$ indicates this with the presence of the MeV unit. Thus, thermal agitation or chemical energies, typically hundreds of kcal/mol at the most, are utterly incapable of exciting nuclei to higher energy levels. For these reasons, man has seen green grass, grown food, and started fires – all electronic processes – and generally not seen nuclear processes. That sunrises may

153

endure, we hope that future nuclear processes are confined to isotopic labeling, medicinal purposes, spectroscopy, and power plants. See Section 16.5.

I will close this chapter of my thesis, as well as our brief foray into chemical education, with a quotation from the chapter on the *d*-block elements that is a hybrid of the two methods used above. It was designed to give the student a grain of salt to mix with the "more rigorous definitions and concepts" to which we alluded above. The skeptical chemist, with all honors due to Boyle, must recognize chemical models are flawed and that it is their utility that makes them relevant:

> The "correctness" of the Crystal Field Model and the Ligand Field Model is secondary to the success of these theories. From our modern view crystal field theory seems unrealistic and not rooted deeply in orbital theory, aside from its inclusion of the *d* orbitals. At least ligand field theory incorporates the MO theory of Chapter 7, yielding Figure 17.13 [an MO diagram] for octahedral complexes. Before, however, we banish crystal field theory to the chemistry underworld, note that many chemists still routinely use Lewis structures in research ideas or proposals or in lectures to other advanced scientists who are "in the know", yet Lewis structures are hardly "correct". Research *must* move forward; chemistry must advance. It takes all sizes and shapes of chemists to make the chemistry world go 'round, and many chemists can't worry about the details of a monstrous Hamiltonian. In many ways it is completely irrelevant to them. Lewis structures work in many cases. Likewise, crystal field theory and ligand field theory, for that matter, work in many cases, giving rational explanations for the color, shape, magnetic properties, bonding, and other aspects of transition metal complexes. Useful tools, schematic or not, can never and should never be eliminated from science. The key result of either theory is the *splitting* Δ_o that exists between the *d* orbitals. When the splitting is large, strong M–L bonds are predicted along with large electron energy level spacing. The opposite is true for small Δ_o's. This parameter also helps to predict and explain magnetic properties via unpaired electrons by comparing its value to the pairing energy between two electrons in the same *d* orbital.

154

The two methods shown above were intended to assist the students' understanding of concepts by building on their prior knowledge or by presenting brief summations of complex material that included examples from several chapters and topics. Further, it is hoped that reminding the student that our explanations and models can be extended to many areas will lessen anxiety since only a small number of new concepts must be learned to succeed.

APPENDIX

Below we outline how to calculate the initial energy of the system E, as defined previously, at a particular nozzle temperature. Analysis of supersonic jets[102,103] leads to the main conclusion that the beam of gas that emerges from a very small orifice is "cold" in the sense that it has a very narrow velocity distribution. The gas particles' flow velocity v_f, the velocity relative to the reference frame of the laboratory, is nonetheless typical in magnitude of any gas as described by the Maxwell-Boltzmann velocity distribution. (The velocity distribution is, however, certainly *not* Maxwellian.) For supersonic jets v_f is given by a modified version of the Maxwell-Boltzmann most probable velocity formula:

$$v_f = \sqrt{\frac{\gamma}{\gamma-1}}\sqrt{\frac{2k_B(T_0-T)}{m}}\ . \tag{4}$$

γ is the heat capacity ratio C_P/C_V, T_0 is the temperature of the nozzle, T is the cooled translational temperature, and m is the mass of a single gas atom or molecule. γ has the approximate value of 5/3 for ideal monatomic gases (e.g., He and Ne) or 7/5 for diatomic rigid rotors (e.g., N_2 and H_2) and other linear polyatomic molecules (e.g., CO_2 and C_2H_2) with no low frequency vibrations. For nonlinear polyatomic molecules $\gamma = 4/3$. These approximate values come from the equipartition theorem. The value of 5/3 is nearly exact for the noble gases, and we use it for neon. The more exact value for CO_2 that has been obtained for our spectrometer[104]

is 1.395 and will be used here. Since energy can be stored in the internal (rotational and vibrational) degrees of freedom, thereby affecting the heat capacities, it is important to point out that the large number of collisions that occur in the nozzle relax the rotations and vibrations of the molecule, converting rotational and vibrational energy into translational energy. Usually, most vibrational levels are not occupied, and little energy is stored in them. The energy in rotation, however, is significant, sometimes resulting in *heavier* particles having a *greater* v_f, than lighter particles, once the rotational energy has been converted to translational motion. Such is that case here, where C_2H_2 has a greater v_f than Ne. We make the assumption, then, that C_2H_2 has no occupied vibrational levels and no low frequency vibrations that can become excited. Thus, we use $\gamma = 7/5$ for C_2H_2. (Note, also, that any residual vibrational energy does not contribute to the translational velocity of the gas.)

In Equation 4 T is a measure of the velocity spread in the beam; the lower T is, the smaller the spread in velocity. To determine T, we first need S, the speed ratio, given by

$$S = M\sqrt{\frac{\gamma}{2}}, \tag{5}$$

where M is the mach number, the ratio of v_f to the local speed of sound. It is no simple task to determine M, which can be obtained by time of flight analysis. [49, 64] Here, we use $M(CO_2) = 8.4$, as determined in the referenced time of flight measurements. Further, we estimate that $M(Ne) = 15$ and $M(C_2H_2) = 8$. T is then given by

$$T = \frac{T_0}{1 + \left(\frac{\gamma - 1}{\gamma}\right) S^2}. \tag{6}$$

Note that for infinite M, T = 0, reducing the second factor of Equation 4 to the exact formula for the most probable velocity of a gas in a Maxwellian distribution. Thus, any nonzero T works to *decrease* v_f relative to the most probable velocity of a gas in a Maxwellian beam. M increases lead to smaller T values, via Equations 5 and 6, and M can vary significantly between seemingly similar molecules. The first factor of Equation 4, however, is always greater than 1, which works to *increase* v_f relative to the most probable velocity of a gas in a Maxwellian beam. Thus, the correlation between v_f, m, and M can't be simply stated, nor can the values of v_f for two different molecules be easily predicted. As noted above, C_2H_2 has a *larger* v_f than Ne. CO_2, however, has a smaller v_f than Ne. The T correction, generally, is small, and the first factor in Equation 4 ensures that v_f for a supersonic beam of gas always exceeds the most probable velocity for a Maxwellian beam.

Now v_f can be calculated. To be slightly more accurate, however, it is better to use the most probable velocity v_{mp} to determine E via Equation 1. v_{mp} is given by

$$v_{mp} = v_f \left(1 + \frac{1}{S^2}\right). \tag{7}$$

As shown in Figure 1, we calculate v_{rel} by the Pythagorean Theorem, giving

$$v_{rel}^2 = \left(v_{mp}^{Ne*}\right)^2 + \left(v_{mp}^{CO_2}\right)^2. \tag{8}$$

Finally, then, the collision energy is given by substituting into Equation 1:

$$E = \frac{1}{2}\mu v_{rel}^2 = \frac{1}{2}\mu\left[\left(v_{mp}^{Ne*}\right)^2 + \left(v_{mp}^{CO_2}\right)^2\right]. \tag{9}$$

Next, we complete the actual calculation for Ne* + CO$_2$, leaving T_0 so that we can calculate E at the four different nozzle temperatures used. Combining Equations 5 and 6 for Ne gives

$$T = \frac{T_0}{1 + \frac{1}{2}(\gamma-1)M^2} = \frac{T_0}{1 + \frac{1}{2}\left[\left(\frac{5}{3}\right)-1\right](15)^2} = \frac{T_0}{76}. \tag{10}$$

Next, the flow velocity is given by

$$v_f^{Ne*} = \sqrt{\frac{\gamma}{\gamma-1}}\sqrt{\frac{2k_B(T_0-T)}{m}}$$

$$= \sqrt{\frac{5/3}{\frac{5}{3}-1}} \times \sqrt{\frac{2(1.38065 \times 10^{-23}\text{ J/K})\left(T_0 - \frac{T_0}{76}\right)}{20.1797\text{ amu}\left(\frac{1.66054 \times 10^{-27}\text{ kg}}{1\text{ amu}}\right)}} \tag{11}$$

$$= 45.38839\text{ m s}^{-1}\text{ K}^{-1/2}\sqrt{T_0 - \frac{T_0}{76}} = 45.08879\text{ m s}^{-1}\text{ K}^{-1/2}\sqrt{T_0}$$

The most probable velocity follows from

$$v_{mp}^{Ne^*} = v_f^{Ne^*}\left(1 + \frac{1}{S^2}\right) = 45.08879 \text{ m s}^{-1} \text{ K}^{-1/2}\sqrt{T_0} \times \left(1 + \frac{1}{M^2\left(\frac{\gamma}{2}\right)}\right)$$

$$= 45.08879 \text{ m s}^{-1} \text{ K}^{-1/2}\sqrt{T_0} \times \left(1 + \frac{1}{(15)^2\left(\frac{5/3}{2}\right)}\right) \qquad (12)$$

$$= 45.32926 \text{ m s}^{-1} \text{ K}^{-1/2}\sqrt{T_0}$$

For CO_2 $T_0 = 313$ K for all of the reactions that were run. Thus, combining Equations 5 and 6 gives

$$T = \frac{T_0}{1 + \frac{1}{2}(\gamma - 1)M^2} = \frac{313 \text{ K}}{1 + \frac{1}{2}(1.395 - 1)(8.4)^2} = 20.95664 \text{ K}. \qquad (13)$$

The flow velocity is given by

$$v_f^{CO_2} = \sqrt{\frac{\gamma}{\gamma - 1}}\sqrt{\frac{2k_B(T_0 - T)}{m}}$$

$$= \sqrt{\frac{1.395}{1.395 - 1}} \times \sqrt{\frac{2(1.38065 \times 10^{-23} \text{ J/K})(313 \text{ K} - 20.95664 \text{ K})}{44.010 \text{ amu}\left(\frac{1.66054 \times 10^{-27} \text{ kg}}{1 \text{ amu}}\right)}} \qquad (14)$$

$$= 624.23967 \text{ m s}^{-1}$$

The most probable velocity is given by

$$v_{mp}^{CO_2} = v_f^{CO_2}\left(1+\frac{1}{S^2}\right) = 624.23967 \text{ m s}^{-1} \times \left(1+\frac{1}{M^2\left(\frac{\gamma}{2}\right)}\right)$$

$$= 624.23967 \text{ m s}^{-1} \times \left(1+\frac{1}{(8.4)^2\left(\frac{1.395}{2}\right)}\right) \qquad (15)$$

$$= 636.92345 \text{ m s}^{-1}$$

Now that we have v_{mp} for both reactants, E is given by Equation 1:

$$E = \frac{1}{2}\mu v_{rel} = \frac{1}{2}\mu\left[\left(v_{mp}^{Ne^*}\right)^2 + \left(v_{mp}^{CO_2}\right)^2\right]$$

$$= \frac{1}{2}\left(\frac{44.010 \text{ amu}(20.1797 \text{ amu})}{64.190 \text{ amu}}\right)\left(\frac{1.66054 \times 10^{-27} \text{ kg}}{1 \text{ amu}}\right) \qquad (16)$$

$$\times \left[\left(45.32926 \text{ m s}^{-1} \text{ K}^{-1/2}\sqrt{T_0}\right)^2 + \left(636.92345 \text{ m s}^{-1}\right)^2\right]$$

$$= 1.14873 \times 10^{-26} \text{ kg}\left[2054.742 \text{ m}^2 \text{ s}^{-2} \text{ K}^{-1/2}(T_0) + 405671 \text{ m}^2 \text{ s}^{-2}\right]$$

Finally, we have a general equation that simply requires input of T_0 in K for Ne*. The above formula is in SI units and gives E in units of J/collision. This is easily converted to the kcal/mol values that are given in the Results section of this dissertation. Repeating this process for C_2H_2 generates the following general formula:

$$E = \frac{1}{2}\mu v_{\text{rel}}^2 = \frac{1}{2}\mu\left[\left(v_{\text{mp}}^{\text{Ne*}}\right)^2 + \left(v_{\text{mp}}^{\text{C}_2\text{H}_2}\right)^2\right]$$

$$= \frac{1}{2}\left(\frac{26.038\ \text{amu}(20.1797\ \text{amu})}{46.218\ \text{amu}}\right)\left(\frac{1.66054 \times 10^{-27}\ \text{kg}}{1\ \text{amu}}\right) \tag{17}$$

$$\times\ \left[\left(45.32926\ \text{m s}^{-1}\ \text{K}^{-1/2}\sqrt{T_0}\right)^2 + \left(823.56354\ \text{m s}^{-1}\right)^2\right]$$

$$= 9.43910 \times 10^{-27}\ \text{kg}\left[2054.742\ \text{m}^2\ \text{s}^{-2}\ \text{K}^{-1/2}(T_0) + 678253\ \text{m}^2\ \text{s}^{-2}\right]$$

BIBLIOGRAPHY

[1] V. Cermak, Z. Herman, Coll. Czech. Chem. Comm., **30**, 169 (1965).

[2] Y. T. Lee, Angewandte Chemie, **26**, 939 (1987).

[3] T. Madison and P. E. Siska, unpublished work.

[4] H. M. Bevseck, Ph.D. Thesis, University of Pittsburgh (1996).

[5] P. E. Siska, Rev. Mod. Phys., **65**, 341-343 (1993).

[6] (a) W. C. Martin, J. Phys. Chem. Ref. Data, **2**, 257 (1973). (b) V. Kaufman and L. Minnhagen, J. Opt. Soc. Amer., **63**, 1185 (1972).

[7] B. Lescop, M. Ben Arfa, M. Cherid, G. Le Coz, G. Sinou, G. Fanjoux, A. Le Nadan, and F. Tuffin, J. Chem. Phys., **108**, 550 (1998).

[8] R. Maruyama, H. Tanaka, Y. Yamakita, F. Misaizu, K. Ohno, Chem. Phys. Lett., **327**, 104 (2000).

[9] M. Ben Arfa, B. Lescop, M. Cherid, B. Brunetti, P. Candori, D. Malfatti, S. Falcinelli, F. Vecchiocattivi, Chem. Phys. Lett., **308**, 71 (1999).

[10] B. Lescop, M. Ben Arfa, M. Cherid, G. Le Coz, G. Sinou, G. Fanjoux, A. Le Nadan, and F. Tuffin, J. Elec. Spec. Rel. Phen., **87**, 51 (1997).

[11] A. Le Nadan, G. Sinou, and F. Tuffin, J. de Physique II, **3**, 775 (1993).

[12] B. Lescop, M. Ben Arfa, M. Cherid, G. Fanjoux, E. Kassab, J. de Chimie Physique et de Physico-Chimie Biologique, **95**, 2113 (1998).

[13] B. Lescop, M. Ben Arfa, G. Le Coz, M. Cherid, G. Sinou, A. Le Nadan, and F. Tuffin, Chem. Phys. Lett., **252**, 327 (1996).

[14] A. Aguilar, B. Brunetti, M. Gonzalez, and F. Vecchiocattivi, Chemical Physics, **145**, 211 (1990).

[15] F. Biondini, B. Brunetti, P. Candori, F. De Angelis, S. Falcinelli, F. Tarantelli, M. Teixidor, F. Pirani, F. Vecchiocattivi, J Chem. Phys., **122**, 164307 (2005).

[16] F. Biondini, B. Brunetti, P. Candori, F. De Angelis, S. Falcinelli, F. Tarantelli, M. Teixidor, F. Pirani, and F. Vecchiocattivi, J Chem. Phys., **122**, 164308 (2005).

[17] H. M. Bevsek, D. C. Dunlavy, and P. E. Siska, J. Chem. Phys., **102**, 133 (1995).

[18] D. C. Dunlavy and P.E. Siska, J. Phys. Chem., **100**, 21 (1996).

[19] B. A. Jacobs, W. A. Rice, and P. E. Siska, J. Chem. Phys., **118**, 3124 (2003).

[20] J. H. Noroski and P. E. Siska, J. Chem. Phys., **125**, 133118/9 (2006).

[21] J. Noroski, L. Park, and P. E. Siska (unpublished).

[22] H. Hotop, A. Niehaus, and A. L. Schmeltekopf, Zeitschrift für Physik (Z. Phys.), **229**, 1 (1969).

[23] P.J. Keliher, F. B. Dunning, M. R. O'Neill, R. D. Rundel, and G. K. Walters, Phys. Rev. A, **11**, 1271 (1975).

[24] P. E. Siska, Rev. Mod. Phys., **65**, 338 (1993).

[25] *CRC Handbook of Chemistry and Physics*, 86th Ed., CRC Press, Boca Raton, 10-208 (2005).

[26] Huber, K. B.; Herzberg, G., *Molecular Spectra and Molecular Structure. IV. Constants of Diatomic Molecules*; van Nostrand Reinhold: New York, 1979.

[27] O. Edqvist, E. Lindholm, L. E. Selin, L. Åsbrink, Phys. Scr., **1**, 25 (1970).

[28] D. L. Albritton, A. L. Schmeltekopf, R. N. Zare, J. Chem. Phys., **71**, 3271 (1979).

[29] P. Baltzer, F. Chau, J. Eland, L. Karlsson, M. Lundqvist, J. Rostas, K. Tam, H. Veenhuizen, B. Wannberg, J. Chem. Phys., **104**, 8922 (1996).

[30] L. Wang, J. Ruett, Y. Lee, and D. Shirley, J. Elec. Spec. Rel. Phen., **47**, 167 (1988).

[31] R. T. Wiedmann, E. R. Grant, R. G. Tonkyn, M. G. White, J. Chem. Phys., **95**, 752 (1991).

[32] W. Kong, D. Rodgers, J. W. Hepburn, Chem. Phys. Lett., **221**, 301 (1994).

[33] E. Kinmond, J. Eland, L. Karlsson, Inter. J. Mass. Spec., **185/186/187**, 437 (1999).

[34] D. Holland, M. MacDonald, M. Hayes, L. Karlsson, B. Wannberg, J. Elec. Spec. Rel. Phen., **97**, 253 (1998).

[35] N. Kishimoto, E. Matsumura, K. Ohno, J. Chem. Phys., **121**, 3074-3086 (2004).

[36] M. Yamazaki, S. Maeda, K. Ohno K., Chem. Phys. Lett., **391**, 366 (2004).

[37] W. H. Miller, J. Chem. Phys., **52**, 3563 (1970).

[38] A. P. Hickman and H. Morgner, J. Phys. B., **9**, 1765 (1976).

[39] I. N. Levine, *Molecular Spectroscopy*, John Wiley & Sons: New York, 1975.

[40] L. Avaldi, G. Dawber, R. Hall, G. King, A. McConkey, M. MacDonald, G. Stefani, J. Elec. Spec. Rel. Phen. **71**, 93 (1995).

[41] A. P. Hickman and H. Morgner, J. Chem. Phys. **67**, 5484 (1977).

[42] C. Weiser and P. E. Siska, Rev. Sci. Instrum. **58**, 2124 (1987); Z. Phys. D **10**, 165 (1988).

[43] E. Harting and F. H. Read, *Electrostatic Lenses*, Elsevier: New York, 1976.

[44] (a) J. H. Moore, C. C. Davis, and M. A. Coplan, *Building Scientific Apparatus,* Addison-Wesley: London, 1983.
(b) P. R. Bevington and D. K. Robinson, *Data Reduction and Data Analysis for the Physical Sciences*, McGraw-Hill: New York ,1992.

[45] C. Weiser and P. E. Siska, Rev. Sci. Instrum. **58**, 2124 (1987); Z. Phys.D: At., Mol. Clusters **10**, 165 (1988).

[46] J. Ingle, S. Crouch, *Spectrochemical Analysis*, Prentice Hall: New Jersey, 212 (1988).

[47] Dixon, T. and Woods, R., Phys. Rev. Lett. **34**, 61 (1975).

[48] Y. T. Lee, Angew. Chem. Int. Ed. Engl. **26**, 939 (1987).

[49] Dunlavy, D. C., Ph.D. Dissertation, University of Pittsburgh, (1996).

[50] Cyphersmith, A., *A Study of Penning Ionization of Metastable Ne* and N_2O: Potential Energy Surfaces*, Bachelor of Philosophy Thesis, University of Pittsburgh, (2008).

[51] J. Ruett, L. Wang, J. Pollard, D. Trevor, Y. Lee, D. Shirley, J. Chem. Phys. **84**, 3022 (1986).

[52] R.W. Nicholls, M. Amani, and M. Mandelman, Canadian J. of Phys. **79**, 611 (2001).

[53] (a) Rydberg, R., Z. Phys., **73**, 376 (1931). (b) Klein, 0., Z. Phys., **76**, 226 (1932). (c) Rees, A. L. G., Prog. Phys. Soc., **59**, 998 (1947). (d) F. Castaño, J. de Juan, and E. Martinez, J. Chem. Ed., **60**, 91 (1983).

[54] J. M. Luis, D. M. Bishop, B. Kirtman, J. of Chem. Phys., **120**, 813 (2004).

[55] R. S. Drago, *Physical Methods for Chemists*, Saunders: Fort Worth, 112 (1992).

[56] N. J. D. Lucas, J. Phys. B: Atom. Molec. Phys., **6,** 155 (1973).

[57] J. M. Luis, D. M. Bishop, B. Kirtman, J. of Chem. Phys., **120**, 813 (2004).

[58] M. W. N. Ibrahim, eprint arXiv:physics/0005036, (2000).

[59] W. Bussert, J. Ganz, H. Hotop, M. W. Ruf, A. Siegel, H. Waibel, P., Botschwina, and J. Lorenzen, Chem. Phys. Lett. **95**, 277 (1983).

[60] J. M. Frye and T. J. Sears, Mol. Phys. **62**, 919 (1987).

[61] V. Cermak, J. Elec. Spec. Rel. Phen. **9**, 419 (1976).

[62] J. H. D. Eland and C. J. Danby, Intl. J. of Mass Spec. and Ion Phys., **1**, 111 (1968).

[63] T. E. Sharp and H. M. Rosenstock, J. Chem. Phys., **41**, 3453 (1964).

[64] C. Baker, D. W. Turner, Proc. Roy. Soc. **A308**, 19 (1968).

[65] J. Yang and Y. Mo, J. Phys. Chem. A, **110**, 11001 (2006).

[66] A. C. Parr, D. L. Ederer, J. B. West, D. M. P. Holland, J. L. Dehmer, J. Chem. Phys., **76**, 4349, (1982).

[67] T. Bregel, A. J. Yencha, M. W. Ruf, H. Waibel, and H. Hotop, Z. Phys. D, **13**, 51 (1989).

[68] D. S. C. Yee, W. D. Stewart, C. A. McDowell, and C. E. Brion, J. Elec. Spec. Rel. Phen., **7**, 93 (1975).

[69] Y. Harada, K. Ohno, and H. Mutoh, J. Chem. Phys., **79**, 3251 (1983).

[70] J. E. Collin and P. Natalis, J. Mass Spectrom. Ion Phys, **2**, 23l (1969).

[71] P. Natalis, J. Delwiche, and J. E. Collin, Chem. Phys. Letters, **13**, 491 (1972).

[72] C. E. Brion, C. A. McDowell, and W. D. Stewart, Chem. Phys. Lett., **13**, 79 (1971).

[73] H. Hotop, Radiation Research, **59**, 379 (1974).

[74] H. Hotop, E. Kolb, and J. Lorenzen, J. Elec. Spec. Rel. Phen., **16**, 213 (1979).

[75] A. J. Yencha, M. W. Ruf, and H. Hotop, Z. Phys. D, **14**, 57 (1991).

[76] O. Leisin, H. Morgner, and W. Müller, Z. Phys. A., **304**, 23 (1982).

[77] G. R. Branton, D. C. Frost, T. Makita, C. A. McDowell, and I. A. Stenhouse, Phil. Trans. Roy. Soc. Lond. A, **268**, 77 (1970).

[78] J. Schiedt and R. Weinkauf, Z. Naturforsch A, **50**, 1041 (1995).

[79] L. Appolloni, B. Brunetti, F. Vecchiocattivi, and G. G. Volpi, J. Phys. Chem., **92**, 918 (1988).

[80] R. McWeeny, J. Molec. Struc. (Theochem), **261**, 403 (1992).

[81] T. E. Sharp, Atom. Data, **2**, 119 (1371).

[82] Travers M. J., Cowles D. C., and Ellison G. B., Chem. Phys. Lett., 164, 449 (1989).

[83] F. Merkt and P. M. Guyon, Chemical Physics, **173**, 479 (1993).

[84] C. Lavin, A. M. Velasco, I. Martin, E. Bustos, Chem. Phys. Lett., **394**, 114 (2004).

[85] N. Jones, R. Minns, R. Patel, H. Fielding, J. Phys. B: At. Mol. Opt. Phys., **41**, 185102 (2008).

[86] H. Lefebvre-Brion and K. Yoshino, J. Molec. Spec., **158**, 140 (1993).

[87] T. Ebata, T. Sutani, N. Mikami, Chem. Phys. Lett., **240**, 357 (1995).

[88] M. Drabbels, J. Heinze, J. J. ter Meulen, and W. L. Meerts, J. Chem. Phys., **99**, 5701 (1993).

[89] P. F. Levelt, W. Ubachs, and W. Hogervorst, J. Chem. Phys., **97**, 7160 (1992).

[90] J. Weber and G. Hohlneicher, Mol. Phys., **101**, 2125, (2003).

[91] C. R. Brundle and C. W. Turner, Int. J. Mass. Spec. Ion. Phys., **2**, 195, (1969).

[92] H. Hotop and N. Niehaus, Z. Phys., **228**, 68 (1969).

[93] K. M. Ervin, J. Ho, and W. C. Lineberger, J. Chem. Phys., **91**, 5974, (1989).

[94] H. M. Bevsek and P. E. Siska, J. Chem. Phys., **102**, 1934 (1995).

[95] M. F. Falcetta, J. L. Pazun, M. J. Dorko, D. Kitchen, and P. E. Siska, J. Phys. Chem., **97**, 1011 (1993).

[96] K. T. Tang and J. P. Toennies, J. Chem. Phys., **80**, 3726 (1984).

[97] P. E. Siska, J. Chem. Phys., **85**, 7497 (1986).

[98] M. F. Falcetta and P. E. Siska, Mol. Phys., **88**, 647 (1996).

[99] M. F. Falcetta and P. E. Siska, Mol. Phys., **97**, 117 (1999).

[100] J. M. Brom, Jr., J. H. Kolts, and D. W. Setser, Chem. Phys. Lett., **55**, 44 (1978).

[101] F. T. M. van den Berg, J. H. M. Shonenberg, and H. C. W. Beijerinck, Chem. Phys., **115**, 359 (1987).

[102] J. B. Anderson, R. P. Andres, and J. B. Fenn, Adv. Chem. Phys., **10**, 275 (1966).

[103] H. C. W. Beijerinck and N. F. Vester, Physica, **111C**, 327 (1981).

[104] J. Pazun, Ph.D. Thesis, University of Pittsburgh (1991).